



Title	Elucidation of Structure-Activity Relationship in Heterogeneous Catalysis by in situ/operando Surface Science Techniques
Author(s)	LU, Bang
Citation	北海道大学. 博士(工学) 甲第15620号
Issue Date	2023-09-25
DOI	10.14943/doctoral.k15620
Doc URL	http://hdl.handle.net/2115/90838
Type	theses (doctoral)
File Information	LU_Bang.pdf



[Instructions for use](#)

Elucidation of Structure-Activity Relationship in Heterogeneous
Catalysis by *in situ/operando* Surface Science Techniques

in situ/operando 表面科学手法による不均一触媒構造活性相関の解明

Bang Lu

魯邦

Division of Quantum Science and Engineering

Graduate School of Engineering, Hokkaido University

September 2023

ABSTRACT

Catalysts play a critical role in industrial chemistry since they can increase the rate of chemical reactions. Most of the industrial catalysts consist of active metal species that are highly dispersed on powdery oxide supports and the catalytic performance largely depends on the morphological and electronic states of the active metal species. Therefore, it is important to characterize them at the atomic level to elucidate the “structure-activity relationship” for the development of further active catalysts. However, since the powdery catalysts are “ill-defined” with polycrystalline and microporous structures, it is hard to obtain an accurate structure. Using single-crystal surfaces can solve this problem by providing “well-defined” surfaces and applying the ultra-high vacuum (UHV) surface science techniques, which are mainly electron probe techniques, give an atomic-level understanding of the surface processes in heterogeneous catalysis. The catalytic reaction does not occur without reactants (i.e., UHV condition). Thus, the development of *in situ/operando* surface science techniques, where surface characterization is carried out under working conditions, is highly demanded to unravel the surface chemical processes on the model catalysts under realistic reaction conditions.

In this work, firstly I used single-crystal surfaces to investigate the surface processes of plasma-assisted catalysis. Then I analyzed the 3-dimensional structure of Cu species on an α -Al₂O₃(0001) single crystal by polarization-dependent total reflection fluorescence (PTRF)-XAFS. Finally, I developed an *in situ/operando* surface science technique, which is named “*operando* PTRF-XAFS technique”, to obtain the structure-activity relationship in heterogeneous catalysis.

The first chapter of the dissertation is the introduction. The second chapter describes experimental methods. It mainly includes the details of the development of the *operando* PTRF-XAFS technique and the construction of an integrated UHV system for the preparation and multiple characterizations of model catalyst surfaces.

The third chapter describes the investigation of surface processes of plasma-assisted catalysis by surface science techniques. An XPS study on Co(0001) surface

found that the adsorption of nitrogen species occurred when the surface was exposed to the electron cyclotron resonance (ECR) N₂ plasma at room temperature (RT) while no nitrogen adsorption without the plasma. They can be further hydrogenated to ammonia at RT by exposure to the H₂ plasma. The corresponding kinetics and mechanism study was carried out on the Co(0001) surface.

In the fourth chapter, the 3D structure of Cu atoms on an α -Al₂O₃(0001) single-crystal surface at low coverage ($9.7 \times 10^{13} / \text{cm}^2$) was studied in the UHV conditions using the newly developed *operando* PTRF-XAFS cell to test its performance on XAFS measurements. The PTRF-XANES spectra in both s-and p-polarizations showed the formation of monovalent Cu species. Furthermore, an iterative method using FEFF code to simulate PTRF-EXAFS spectra based on a real-space model structure suggested that the Cu species was atomically dispersed and stabilized by the surface oxygens of the α -Al₂O₃(0001) surface.

The fifth chapter focuses on an *operando* study of a Pt/ α -Al₂O₃(0001) model catalyst during the CO oxidation reaction using the batch-type *operando* PTRF-XAFS cell. The cuboctahedral Pt clusters consisting of 147 Pt atoms were found to be the main species under the CO oxidation reaction condition at 493K. Its corresponding turnover frequency (TOF) of CO₂ formation was determined to be 0.06 s⁻¹ based on the structure determined by the *operando* PTRF-XAFS and the simultaneous activity measurements using the quadrupole mass spectrometry (QMS).

In the sixth chapter, I found there were two temperature regimes in the activation energies towards CO oxidation on the Pt/ α -Al₂O₃(0001) by using the flow-type cell. The *in situ* PTRF-XAFS measurements were applied to reveal the origin of two different activation energies.

The seventh chapter is the general conclusions of the work. I have successfully developed a novel *operando* PTRF-XAFS technique to reveal the well-defined catalyst surface structure to unravel the surface processes. Consequently, my Ph.D. work has opened a new horizon of *operando* surface science in the heterogeneous catalysis field.

TABLE OF CONTENTS

ABSTRACT	2
CHAPTER 1 GENERAL INTRODUCTION	6
1.1 Overview	6
1.2 Model catalyst	7
1.3 Conventional Surface Science Techniques.....	11
1.4 <i>in situ</i> / <i>operando</i> characterizations.....	17
CHAPTER 2 EXPERIMENTAL METHODS	27
2.1 Construction of an Integrated UHV System for the Preparation and Multiple Characterizations of Model Catalyst Surfaces.....	27
2.2 Polarization-Dependent Total Reflection Fluorescence X-ray Absorption Fine Structure Technique	32
2.3 Development of <i>operando</i> PTRF-XAFS system.....	37
2.4 Modification from the batch-type to flow-type cell	40
2.5 Data analysis method for PTRF-XAFS.....	41
CHAPTER 3 PLASMA-ASSISTED NITROGEN ADSORPTION AND HYDROGENATION ON Co(0001) SURFACE	58
3.1 Kinetic Analysis of Plasma-Assisted Nitrogen Adsorption on Co(0001) Surface	59
3.2 Hydrogenation of nitrogen species on Co(0001) surface.....	67
3.3 Conclusions	68
CHAPTER 4 3D STRUCTURE OF LOW COVERAGE Cu SPECIES ON α - Al ₂ O ₃ (0001) SURFACE EXAMINED BY UHV PTRF-XAFS.....	75

4.1	Performance Test of the New Cell – Attaining PTRF-XAFS Spectra of a Low Coverage Model System.....	76
4.2	3D Structure Determination of Cu Atoms on α -Al ₂ O ₃ (0001)	80
4.3	Conclusions	84
CHAPTER 5 STUDY OF A Pt/ α -Al ₂ O ₃ (0001) MODEL CATALYST DURING CO OXIDATION REACTION USING <i>in situ/operando</i> PTRF-XAFS TECHNIQUE		98
5.1	3D structure of as-deposited Pt species on α -Al ₂ O ₃ (0001) surface at room temperature	99
5.2	Simultaneous measurements of catalytic activity and XANES	103
5.3	3D structure of the Pt species on α -Al ₂ O ₃ (0001) surface during CO oxidation... ..	105
5.4	Conclusions	107
CHAPTER 6 ELUCIDATING ACTIVATION ENERGY CHANGE TOWARDS CO OXIDATION ON Pt/ α -Al ₂ O ₃ (0001) VIA <i>in situ/operando</i> PTRF-XAFS		121
6.1	Temperature dependence of activation energy towards CO oxidation on the Pt/ α -Al ₂ O ₃ (0001)	122
6.2	Investigation of adsorbates on Pt/ α -Al ₂ O ₃ (0001) during CO oxidation.....	125
6.3	Conclusions	128
CHAPTER 7 GENERAL CONCLUSIONS		138
ACKNOWLEDGEMENTS.....		143
COPYRIGHTS & PERMISSIONS		144

CHAPTER 1

GENERAL INTRODUCTION

1.1 Overview

Catalysts are key materials for the development of a sustainable society and play a critical role in the industrial production of various chemicals. More than 80% of the catalytic processes use the heterogeneous catalysis system to achieve high conversion and / or selectivity by lowering of the activation barriers to lead to the desired products [1, 2]. These materials mainly consist of transition metals supported and stabilized by oxide substrates. Plenty of research has shown that the catalytic reaction rate per unit of catalyst area largely depends on the structure of the catalyst [3]. The term “structure” here represents not only the geometric structure of the metal species, but also the electronic states that are affected by the interaction with the support surface and the adsorbed species. Especially, the geometric and electronic effects cannot be separated as independent parameters in many cases. For example, when the size of metallic particles increases, it leads to an electron bandwidth increase, this in turn changes the nature of the exposed facets of the metal surface. Therefore, it is important to have a better understanding of the physical and chemical properties of the catalysts underlying the catalytic reactions. However, the realistic industrial catalysis involves complex reaction processes on the “ill-defined” catalyst surfaces, it is difficult to obtain the accurate “structure-activity relationship”. Using single crystal surfaces can solve this problem by providing “well defined” surfaces and applying the ultra-high vacuum (UHV) surface science techniques, which are mainly electron probe techniques, give an atomic level understanding of the

surface processes in heterogeneous catalysis. Moreover, the structure of the catalyst cannot be treated as a static item because the surface structure can be largely modified under high temperature conditions or the presence of reactive gases [4, 5]. Therefore, a fundamental understanding of the geometric and electronic structure of a supported metal species under the catalytic reaction conditions is required and represents an important step towards elucidation of the precise structure-activity relationship in heterogeneous catalysis, which will lead to the design and development of high-performance catalysts.

1.2 Model catalyst

During the long period of the utilization of the catalyst, the synthesis and treatment receipts were based on empirical studies, which is an unwelcome situation for scientific researchers. They therefore want to obtain the fundamental understanding of the catalytic processes by connecting the macroscopic effects with the microscopic processes taking place on the surface. However, there is a big obstacle in the way, i.e., the complexity of the practical industrial catalysis. The practical catalytic reactions usually comprise multiple steps, such as adsorption, diffusion, dissociation of reactants, and desorption of products. Each step, which can occur on a different site on the surface, is governed by their own rate laws. This extremely complex situation often hampers the understanding of the whole reaction in detail. Fortunately, we have a powerful tool which is widely used in many scientific research fields, i.e., the idealized model. It involves a simplification of something complicated with the objective of making it more tractable or understandable. Specifically, model catalyst in this work.

In the late 1960s, the concept of model catalyst was introduced with the development of UHV technology. The so-called model catalysts are basically well-define

materials, which can partially / completely simulate the complexities of realistic catalysts, helping us to establish the fundamental understanding of the surface structure, metal particle size and support effects on catalyst reactivity and selectivity.

[Metal single crystal]

Metal single crystals are the most common model system for heterogeneous catalysis. They only consist of pure transition metal and have well-defined bulk structures and highly uniformed surface structures. They can be therefore easily characterized and studied in detail, both under UHV conditions and under simulated catalytic conditions [6-8]. Another benefit of using the metal single crystals as the model catalysts is that the surface structure properties such as the number and type of steps and kinks can be easily controlled by cutting the metal crystal in specific directions.

Plenty of catalytic reactions were therefore studied on transition metals for various reactions. A pioneering work about the ammonia synthesis processes has been done by Ertl et al. [9] and Somorjai et al. [10]. Figure 1-1 is the results of a representative experiment by Somorjai [11]. It shows the rate of dissociative adsorption of nitrogen on iron single-crystal surfaces of different orientation. Both the dissociative adsorption of the nitrogen molecules and the overall catalytic reaction rate are largely dependent on the crystal face of the iron surface involved in the experiment. Based on these fundamental studies Stoltze and Nørskov [12, 13] successfully constructed a micro kinetic model that can describe the ammonia synthesis process under industrial conditions. Many other catalytic reactions have also been studied by using the metal single crystals such as the oxidation and hydrogenation of CO [14, 15], the synthesis of methanol [16], and the ring opening of cyclopropane [17].

Here arises the question that does the information we studied on metal single-crystal model catalysts extend to practical industrial catalysis? The answer is uncertain. Indeed, as shown in Figure 1-2, the nanoparticles that are commonly used in industrial catalysts can be considered as a small crystallite composed of many well-defined crystal faces. Many reports also claimed good agreements reached between studies of the same reaction on the metal single-crystal model surface and realistic dispersed catalysts [8]. However, the metal particle size and shape effect [3, 18] and the interaction between the metal nanoparticles and the supports [19-21] are two deep gaps that can never be filled by studying only the pure metal surfaces. Another type of model catalyst that is more closely related to the realistic industrial catalyst is required.

[Oxide-supported metals]

Generally, catalysis can be sorted into heterogeneous and homogeneous catalysis. In heterogeneous catalysis, the catalysts are usually solids, and the reactants and products are in a gas or liquid phase, and the reactant molecules can only react on the surface of the solid catalyst via several mechanisms: Langmuir-Hinshelwood, Eley-Rideal and Mars-van Krevelen [22-24]. The total surface of the catalyst, therefore, has a significant effect on the rate of the reaction. For a certain amount of catalyst, we need to make the catalyst surface as large as possible by shrinking the catalyst particle size into ultra small cluster. Because if the cluster is small enough, most / all the atoms in the cluster can be regarded as surface atoms. The concentration of surface atoms in a cluster with a given size can be described by its dispersion D . where D is the ratio of the number of surface atoms to the total number of atoms of the cluster:

$$D = \frac{\text{number of surface atoms}}{\text{total number of atoms}}$$

1 - 1

Thus, most of the industrial catalysts are made of high-surface-area materials (typically $50 \sim 400 \text{ m}^2\text{g}^{-1}$). However, the size of catalyst particles has a limitation because small particles, especially under nano or sub-nano scales, have higher surface energy and tend to aggregate into larger particles when they are close to each other. Then, catalyst particles are put on the surface of other high surface area materials, which are mostly made of metal oxides, to stabilize and disperse them well. However, it has been reported that the shape and size of the deposited metal species and metal-support interaction largely affect their catalytic performance. As shown in Figure 1-3, the surface structures of such supports are quite involved because a variety of crystal faces are exposed and lots of surface defects exist. When the metal nanoparticles are deposited on these surfaces, plenty of metal nanoparticles with diverse shapes, sizes and metal/oxide interfaces may form, which makes it difficult to have a clear understanding of the connection between the microscopic and macroscopic phenomena.

Oxide-supported metal model catalyst composed of metal nanoparticles deposited on a flat single-crystal oxide support surface (Figure 1-4). This model system can mimic the nanoparticle properties in industrial catalysts by involving the effects of the shape and size of the deposited metal species and metal-support interaction to their catalytic performance.

Benefiting from the development of colloid chemistry and vacuum technology, the oxide-supported model catalysts can be synthesized by nucleation and growth of the metal clusters on a clean oxide surface under UHV or by decomposition of metal-organic precursors [25-27] or wet impregnation [28], so that the metal nanoparticles with well-controlled shape and / or size can be routinely prepared in the solution and vacuum. Based on them, many studies focusing on the metal particle size / shape effects as well as the metal support interactions in the catalytic reactions were conducted [29].

In short, model catalyst is a reductionist tool to deconvolute the observations made with the practical catalyst. By making and studying a model catalyst, we could reveal the origin of a catalytic phenomenon and design further active catalysts.

1.3 Conventional Surface Science Techniques

[UHV system]

The development of surface science promoted the study of the catalyst, especially model catalyst. The surface science approaches enable us to probe the interfaces at atomic level and establish detailed descriptions of catalytic reactions and properties. Most of the techniques involve electrons as the probing method. Considering the mean free path and the impingement rate of the electron probe, an ultra-high vacuum (UHV), i.e., pressure at and below 10^{-5} Pa is required. The mean free path is the distance that a particle, take nitrogen molecules as an example in this case, travels on average between collisions. Its mean free path is shown as

$$\lambda = \frac{\bar{v}}{Z} = \frac{k_B T}{\sqrt{2} \sigma p}$$

2 - 1

where \bar{v} is the mean velocity of the nitrogen molecules in an ideal gas in $\text{m}\cdot\text{s}^{-1}$, Z is the collision frequency in s^{-1} , k_B is the Boltzmann constant with the dimension of $\text{m}^2\cdot\text{kg}\cdot\text{s}^{-2}\cdot\text{K}^{-1}$, and T is the temperature in K, σ is the collision cross section of the nitrogen molecules in m^2 , and p is the gas pressure in Pa. The collision cross section of the nitrogen molecule is 0.42 nm^2 . According to the equation 2 - 1, the mean free path of the nitrogen molecules in the atmospheric pressure (101.3 kPa) is just 70 nm, whereas at around 1×10^{-8} Pa environment the mean free path could be longer than 500 km. Therefore, the electron-based surface science approaches are usually conducted under UHV conditions where the pressure is lower than 10^{-5} Pa, such that the mean free path longer than hundred meters.

From the viewpoint of model catalyst surface, we can calculate the flux (I) incident on the surface using the Hertz-Knudsen equation:

$$I = \frac{p}{\sqrt{2\pi mk_B T}}$$

2 - 2

where m is the mass of a particle in kg. If we place the sample in the chamber that filled by carbon monoxide gas at room temperature, and the surface atom density of the sample to be $1 \times 10^{15} \text{ cm}^{-2}$. A monolayer (ML) would be reduced to:

$$I = (2.9 \times 10^3 \text{ ML s}^{-1})p$$

2 - 3

with the pressure p given in Pa. When the pressure of the carbon monoxide gas is 3×10^{-4} Pa, in every second, the number of the gas molecules that hit the sample surface equal to the equivalent of the number of the entire surface atoms in the sample. If each of these molecules (CO is a well-known active adsorbate of many noble transition metals) stuck to the surface and became absorbed, i.e., sticky coefficient equal to unit, the sample surface would be completely covered in only 1 second. An effective way to avoid this situation is to decrease the environmental pressure of the sample, i.e., UHV conditions. So that the sample surface can be kept as “clean” for a relatively long period of time comparable to the experiment time.

In section 2 of this chapter, the design and construction of an integrated vacuum system and several small vacuum cells will be introduced. Several different types of vacuum pumps were employed to achieve UHV conditions. For instance, dry pump (DP) was used for evacuating the chamber to vacuum condition (typically $1 \sim 10^{-1}$ Pa) and establishing the working environment to high vacuum pumps. It is a mechanical pump that can achieve a clean vacuum without back-flow or diffusion of water and oil to avoid contamination from the sample surface. Turbo molecular pump (TMP) is another type of frequently used vacuum pump to further evacuate the chamber to UHV condition (typically $10^{-5} \sim 10^{-8}$ Pa). It consists of a stationary stator blade and high-speed rotating rotor blade, whose linear velocity is close to the thermal velocity of free molecules so that the gas molecules can be scattered to the desired direction by the molecular drag effect. Titanium sublimation pump (TSP) can form a thin film of metallic titanium on the surrounding chamber wall. The active titanium thin film then adsorbs residual gas from the chamber to achieve better vacuum. Non-evaporable getter (NEG) pump, which has a

similar principle with TSP, was employed and played an important role in my portable chambers / cells.

[XPS]

X-ray Photoelectron Spectroscopy (XPS) is a surface-sensitive technique that can conduct qualitative / quantitative analysis of the surface composition, chemical state of a sample based on photoelectric effect in UHV environment.

In the XPS measurements, the sample is irradiated by a beam of X-ray with a certain known photon energy ($h\nu$), for instance, a commonly used lab-base soft X-ray source aluminum $K\alpha$, $h\nu=1486.7$ eV. The atomic electron can be knocked out with a certain kinetic energy as a photoelectron by absorbing a photon (Figure 1-5). The kinetic energy of the photoelectrons is then detected by an electron energy analyzer. Thus, the binding energy of the emitted electrons can be determined using the following equation:

$$E_b = h\nu - (T + \phi)$$

2 - 4

where E_b and T represent the binding and the kinetic energy of the electron, respectively. ϕ is called work function and it related with the specific situation of the sample surface and condition of the instrument. The binding energy of the atomic electron depends not only on the specific element and orbital, but also on its chemical state and coordination environment. On another hand, the photoelectron emitted from the bulk of the sample has much higher possibility to undergo inelastic collisions, recombination, and excitation of other atoms, they are barely captured by the analyzer. Therefore, by detecting the kinetic

energy of the photoelectrons, the overall electronic structure of the surface species of the sample can be obtained.

The XPS measurements were used to determine the amount of surface adsorbed / deposited species on the single-crystal surfaces. All the XPS spectra in this thesis were conducted background removal using the Shirley background [1].

[LEED]

The surface sensitive technique that has been used most extensively to determine surface geometry is Low Energy Electron Diffraction (LEED). LEED is a macroscopic probe that relies on the long-range order of the surface atoms to produce the constructive and destructive interference of the incident electron wave that generates a diffraction pattern. Thus, for LEED to give an accurate picture of the arrangement of surface atoms, the surface must be highly ordered over large areas (of the order of a few hundred Å). For an ordered surface, measurement of the current of electrons scattered into each LEED beam (I) as a function of incident-electron energy (V), which are referred to as “I-V” measurement, are theoretically capable of determining atomic positions both in the plane of, and normal to, the surface.

In this work, LEED was used to confirm the surface symmetry of the metal single-crystal surface (Co(0001) in Chapter 3) and oxide single-crystal surface (α -Al₂O₃(0001) in Chapter 4, 5, 6).

[AFM&STM]

Atomic Force Microscopy (AFM) is a type of scanning probe microscopy (SPM) that can trace out the geometry of the sample surface by detecting the force between the sample surface atoms and the probe. The schematic of AFM is shown in Figure 1-6.

The cantilever with a tip (~nm in diameter) approaches the sample surface, when the distance between tip and sample surface is close enough, the motion of the cantilever is modified by the sample surface atoms based on the fact that the force between two atoms (tip-sample) depends on the distance between them, and the modification on motion of the cantilever can be amplified by a laser beam and then captured by the detector. Thus, the vertical arrangement of the sample surface atoms can be obtained. One merit of AFM is that despite the substance, the repulsive and attractive force between atoms always exist (Figure 1-7). It means even if the sample is insulator, which is difficult to perform other SPM like STM, the measurement can still be done without extra treatment.

[Others, TPD, QMS]

TPD is a method of detecting desorbed molecules from surface during constant temperature rising, and the information of the binding energy between adsorbed species and surface can be acquired. Before temperature increases, the sample surface is exposed to a probe gas. The gas adsorbs on surface in physisorption (interacting with van der Waals force) or chemisorption (covalent bonding) manners. The binding energy varies with the combination of adsorbed species and adsorption sites on surface. During surface temperature rising process, thermal energy is transferred toward adsorbed species and finally exceeds the binding energy, and then the adsorbed species desorb from the surface. The desorbed gas is detected by a mass spectrometer. The mass signal is proportional to

the amount of desorbed species; thus, the amount of the adsorbed species can be determined as a function of temperature. Moreover, when a specific amount of gas is exposed, one can count the amount of desorbed species, and then the sticking coefficient can be determined.

Quadrupole Mass spectrometer (QMS) is one type of mass spectrometry that consists of four parallel metal rods arranged in the form of a square. A pair of rods at opposite position are connected to each other, and an electrical voltage consisting of a DC portion U and an AC portion with amplitude V and frequency $f=\omega/2\pi$ are applied as:

$$U_{quad} = U + V \cdot \cos(\omega t)$$

2 - 5

The sample molecules are bombarded by electrons into ions before the metal rods. The various of ions with different mass-to-charge ratio (m/z) are then separated in the rod system, only the ions that have certain m/z can go through the rods section and reach the detector for a given ratio of voltages; other ions will collide with the rods due to the unstable trajectories. By applying this system to a gas-phase chemical reaction, the components of the reactant and products can be monitored throughout the whole reaction.

1.4 *in situ / operando* characterizations

To know the structure of metal catalyst, we need to characterize the catalyst surface by applying some surface analysis techniques. Conventionally, *ex situ* study is mainly conducted, i.e., the characterization of catalyst surface is carried out before and after the catalytic reaction and outside of reaction conditions. However, after the concept of

flexible surface that mainly revealed by Somorjai [30], people found that the structure of catalyst may change according to the environment conditions, especially the catalyst prepared in ultra-high vacuum (UHV) and that during catalysis. The reconstruction is caused by two main factors: pressure and temperature [31]. When the pressure of a reactant increases and its coverage on the catalyst surface is high, the repulsion force between adjacent adsorbate becomes strong and leads to a reconstruction of the catalyst to release the repulsion. On another hand, a temperature higher than room temperature is usually necessary for most catalytic reactions because it helps to provide enough thermal energy to overcome the activation barriers. It may also result in an aggregation of small metal clusters into larger ones or a reconstruction of metal catalyst surface.

Therefore, to reveal the real active structure of catalyst and its corresponding catalytic performance, characterization of the catalyst under reaction conditions, i.e., *operando* characterization is highly demanded.

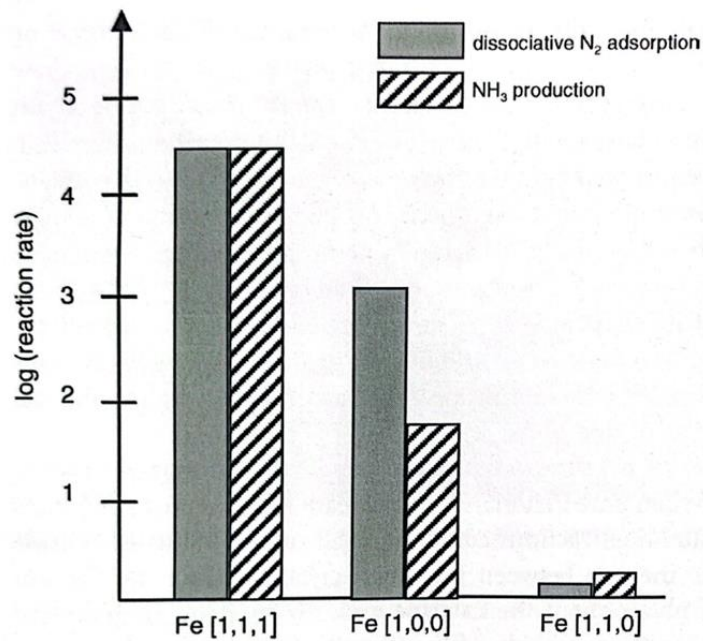


Figure 1-1. Relative rates of dissociative N₂ adsorption (gray bars) and ammonia synthesis (hatched bars) on different planes of Fe single crystals [11].

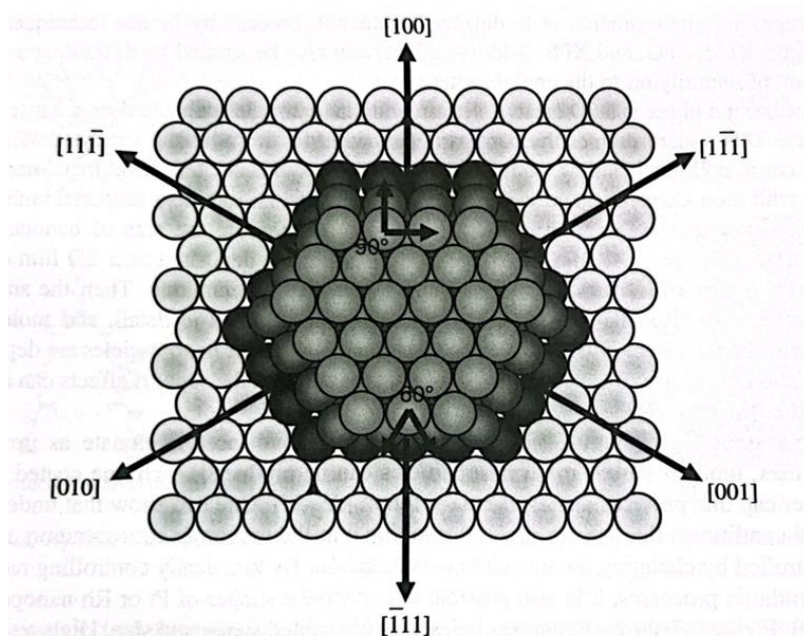


Figure 1-2. Catalyst particle viewed as a crystallite, composed of well-defined atomic planes, steps, and kink sites [10]

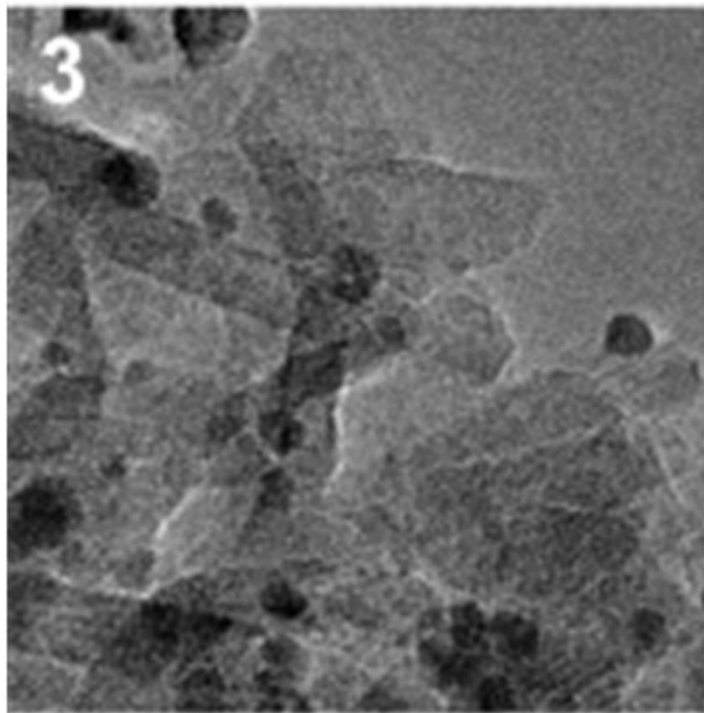


Figure 1-3. TEM images of Pt/γ-Al₂O₃(0001) powdery sample [32].

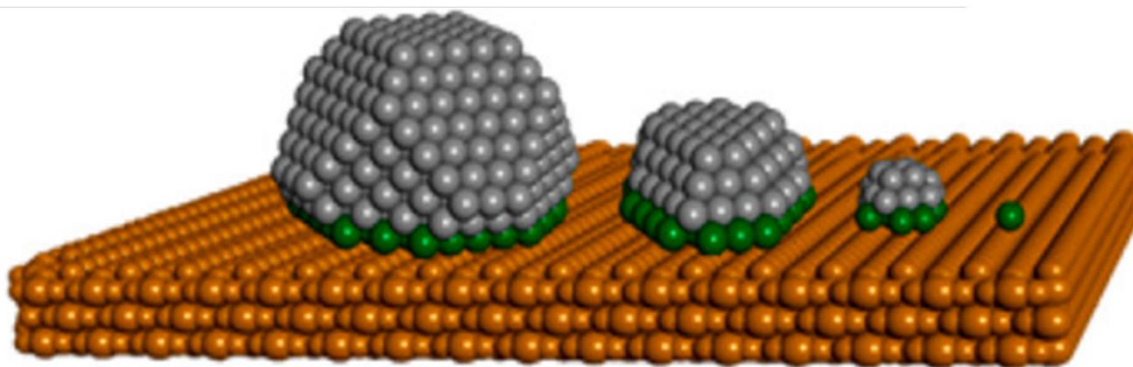


Figure 1-4. Model structures for metal clusters on a flat single-crystal surface [33]

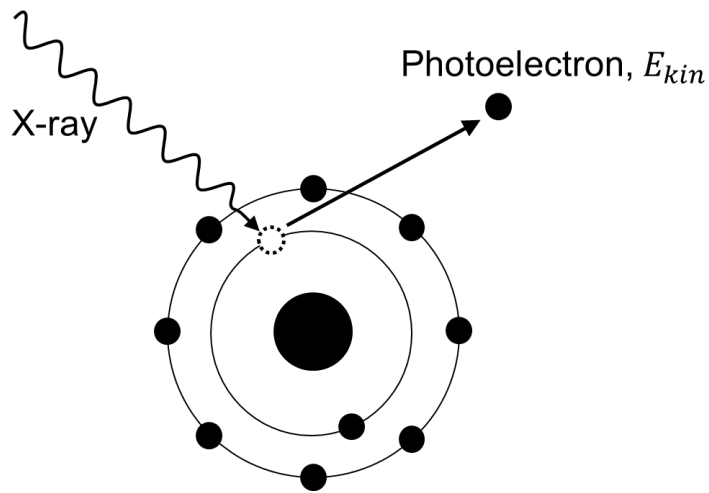


Figure 1-5. The photoelectron generation process.

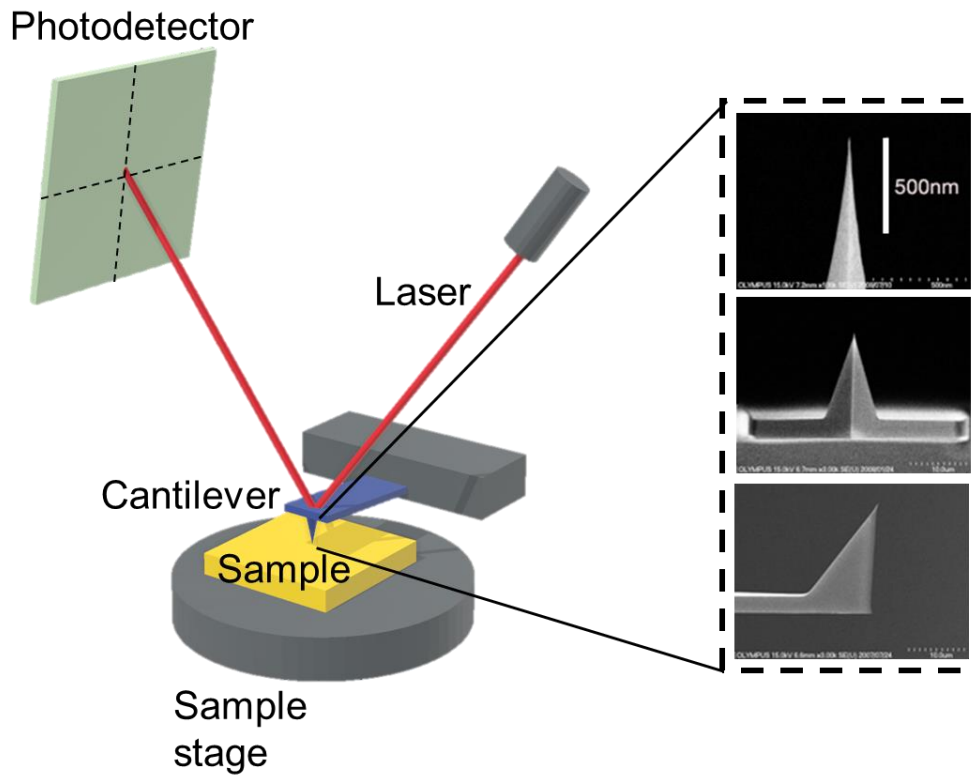


Figure 1-5. The schematic and tip photos of AFM.

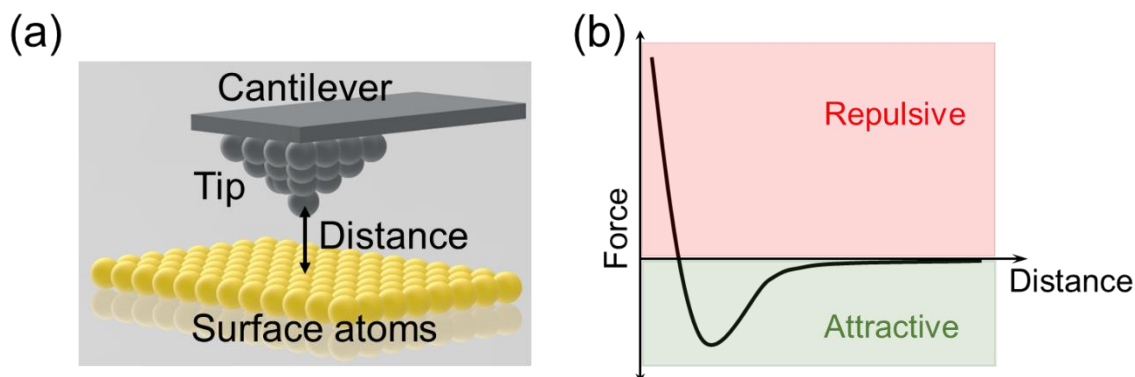


Figure 1-7. (a) The schematics of AFM tip and sample surface and (b) the force between the tip and the surface as a function of the distance.

References

- [1] Handbook of Heterogeneous Catalysis, G. Ertl, H. Knözinger, F. Schüth, and J. Weitkamp, Eds., Weinheim, Germany: Wiley-VCH Verlag GmbH & Co. KGaA, 2008.
- [2] G. A. Somorjai and Y. Li, Introduction to Surface Chemistry and Catalysis. John Wiley & Sons, 2010.
- [3] B. Coq and F. Figueras, "Structure–activity relationships in catalysis by metals: some aspects of particle size, bimetallic and supports effects," *Coordination Chemistry Reviews*, vol. 178–180, pp. 1753–1783, Dec. 1998.
- [4] G. A. Somorjai, "Surface reconstruction and catalysis," *Annual Review of Physical Chemistry*, vol. 45, no. 1, pp. 721-751, 1994.

- [5] J. Rogal, K. Reuter, and M. Scheffler, "First-Principles Statistical Mechanics Study of the Stability of a Subnanometer Thin Surface Oxide in Reactive Environments: CO Oxidation at Pd(100)," *Phys. Rev. Lett.*, vol. 98, no. 4, p. 046101, Jan. 2007.
- [6] D. W. Goodman, "Model catalytic studies over metal single crystals," *Acc. Chem. Res.*, vol. 17, no. 5, pp. 194–200, May 1984.
- [7] G. A. Somorjai and Y. Li, *Introduction to Surface Chemistry and Catalysis*. John Wiley & Sons, 2010.
- [8] J. H. Larsen and I. Chorkendorff, "From fundamental studies of reactivity on single crystals to the design of catalysts," *Surface Science Reports*, vol. 35, no. 5, pp. 163–222, Dec. 1999.
- [9] G. Ertl, D. Prigge, R. Schloegl, and M. Weiss, "Surface characterization of ammonia synthesis catalysts," *Journal of Catalysis*, vol. 79, no. 2, pp. 359–377, Feb. 1983.
- [10] G. A. Somorjai and N. Materer, "Surface structures in ammonia synthesis," *Top Catal*, vol. 1, no. 3, pp. 215–231, Sep. 1994.
- [11] D. Strongin, "The importance of C7 sites and surface roughness in the ammonia synthesis reaction over iron," *Journal of Catalysis*, vol. 103, no. 1, pp. 213–215, Jan. 1987.

- [12] P. Stoltze, "An interpretation of the high-pressure kinetics of ammonia synthesis based on a microscopic model," *Journal of Catalysis*, vol. 110, no. 1, pp. 1–10, Mar. 1988.
- [13] P. Stoltze and J. K. Nørskov, "Bridging the 'Pressure Gap' between Ultrahigh-Vacuum Surface Physics and High-Pressure Catalysis," *Phys. Rev. Lett.*, vol. 55, no. 22, pp. 2502–2505, Nov. 1985.
- [14] R. M. Eiswirth, K. Krischer, and G. Ertl, "Nonlinear dynamics in the CO-oxidation on Pt single crystal surfaces," *Appl. Phys. A*, vol. 51, no. 2, pp. 79–90, Aug. 1990.
- [15] D. W. Goodman, R. D. Kelley, T. E. Madey, and J. T. Yates, "Kinetics of the hydrogenation of CO over a single crystal nickel catalyst," *Journal of Catalysis*, vol. 63, no. 1, pp. 226–234, May 1980.
- [16] P. B. Rasmussen et al., "Methanol synthesis on Cu(100) from a binary gas mixture of CO₂ and H₂," *Catal Lett*, vol. 26, no. 3, pp. 373–381, Sep. 1994.
- [17] T. B. Scoggins, H. Ihm, Y. M. Sun, and J. M. White, "Chemistry of Cyclopropane on Pt(111): Thermal, Electron, and Photon Activation," *J. Phys. Chem. B*, vol. 103, no. 32, pp. 6791–6802, Aug. 1999.
- [18] M. Haruta, T. Kobayashi, H. Sano, and N. Yamada, "Novel Gold Catalysts for the Oxidation of Carbon Monoxide at a Temperature far Below 0 °C," *Chem. Lett.*, vol. 16, no. 2, pp. 405–408, Feb. 1987.

- [19] T. W. van Deelen, C. Hernández Mejía, and K. P. de Jong, “Control of metal-support interactions in heterogeneous catalysts to enhance activity and selectivity,” *Nat Catal*, vol. 2, no. 11, Art. no. 11, Nov. 2019.
- [20] Z. Luo, G. Zhao, H. Pan, and W. Sun, “Strong Metal–Support Interaction in Heterogeneous Catalysts,” *Advanced Energy Materials*, vol. 12, no. 37, p. 2201395, 2022.
- [21] J. (Jimmy) Liu, “Advanced Electron Microscopy of Metal–Support Interactions in Supported Metal Catalysts,” *ChemCatChem*, vol. 3, no. 6, pp. 934–948, 2011.
- [22] G. Ertl, “Reactions at Surfaces: From Atoms to Complexity (Nobel Lecture),” *Angewandte Chemie International Edition*, vol. 47, no. 19, pp. 3524–3535, 2008.
- [23] N. Biophysicahlemistry and O. F. Bristol, “MEXHANISIVLS OF HYDROGEN CATALYSIS By D. D. ELEY,PH.D.,” *QUARTERLY REVIEWS*.
- [24] J. R. H. Ross, “Chapter 7 - The Kinetics and Mechanisms of Catalytic Reactions,” in *Contemporary Catalysis*, J. R. H. Ross, Ed., Amsterdam: Elsevier, 2019, pp. 161–186.
- [25] B. K. Min, W. T. Wallace, and D. W. Goodman, “Support effects on the nucleation, growth, and morphology of gold nano-clusters,” *Surface Science*, vol. 600, no. 2, pp. L7–L11, Jan. 2006.
- [26] M. T. Kief and W. F. Egelhoff, “Growth and structure of Fe and Co thin films on Cu(111), Cu(100), and Cu(110): A comprehensive study of metastable film growth,” *Phys. Rev. B*, vol. 47, no. 16, pp. 10785–10814, Apr. 1993.

- [27] S. K. Purnell, X. Xu, D. W. Goodman, and B. C. Gates, "Adsorption and Reaction of $[\text{Re}_2(\text{CO})_{10}]$ on Ultrathin MgO Films Grown on a Mo(110) Surface: Characterization by Infrared Reflection-Absorption Spectroscopy and Temperature-Programmed Desorption," *J. Phys. Chem.*, vol. 98, no. 15, pp. 4076–4082, Apr. 1994.
- [28] M. Valden, J. Aaltonen, E. Kuusisto, M. Pessa, and C. J. Barnes, "Molecular beam studies of CO oxidation and CO-NO reactions on a supported Pd catalyst," *Surface Science*, vol. 307–309, pp. 193–198, Apr. 1994.
- [29] A. K. Santra and D. W. Goodman, "Oxide-supported metal clusters: models for heterogeneous catalysts," *J. Phys.: Condens. Matter*, vol. 15, no. 2, p. R31, Dec. 2002.
- [30] G. A. Somorjai, "The flexible surface. Correlation between reactivity and restructuring ability," *Langmuir*, vol. 7, no. 12, pp. 3176–3182, Dec. 1991.
- [31] J. Dou, et al. "*Operando* chemistry of catalyst surfaces during catalysis," *Chemical Society Reviews* vol. 46, no. 7, pp. 2001-2027, 2017.
- [32] A. Boubnov et al., "Structure–activity relationships of Pt/Al₂O₃ catalysts for CO and NO oxidation at diesel exhaust conditions," *Applied Catalysis B: Environmental*, vol. 126, pp. 315–325, Sep. 2012.
- [33] I. Ro, J. Resasco, and P. Christopher, "Approaches for Understanding and Controlling Interfacial Effects in Oxide-Supported Metal Catalysts," *ACS Catal.*, vol. 8, no. 8, pp. 7368–7387, Aug. 2018.

CHAPTER 2

EXPERIMENTAL METHODS

2.1 Construction of an Integrated UHV System for the Preparation and Multiple Characterizations of Model Catalyst Surfaces

To investigate the surface processes on the model catalyst surface by surface science approaches, ultra-high vacuum (UHV) condition is a good environment because it can essentially keep the surface unchanged over the duration of an experiment. Therefore, an integrated UHV apparatus that can realize multiple functions including sample preparation, reaction, and surface characterization is demanded.

[UHV chamber]

The construction, modification, and maintenance of the UHV system span my entire doctoral course. The details of the current UHV system are shown in Figure 2-1. The right-side chamber is the main chamber for sample preparation and characterizations. It is evacuated using a turbo molecular pump (TMP) followed by a dry pump (DP). A titanium sublimation pump (TSP) is also employed to reduce the partial pressure of H₂, which is difficult to be evacuated by TMP. Usually, the base pressure of the main chamber can be kept lower than 5×10^{-8} Pa by these efforts. The 4-axis manipulator (x, y, z, θ) that is mounted on the top of the chamber can capture the sample holder vertically around the center of the chamber and enable fine adjustment of the sample position for various treatments and measurements. The left upper part of the system is a high-pressure cell for heterogeneous catalytic reactions. Depending on the cell modules, different types of catalytic reactions can be realized. The operatable pressure range for reactant gases inside

the cell is 1×10^{-5} Pa to 1×10^5 Pa. The left bottom chamber was named “load-lock chamber”. It basically consists of a rotatable plate with 3 slide rails for parking the sample holders. The top cap of the chamber can be opened for sample introduction. The two magnetic rods enable us to transfer the sample between the main chamber and the cell under UHV environment without exposing the sample to air. The base pressure of the load-lock chamber achieves less than 5×10^{-6} Pa. The cell and load-lock chamber are evacuated by another two sets of TMP and DP, respectively.

[heating system and sample holder]

An essential factor that affects the catalytic reactions is the temperature. It is therefore important to control the temperature of the catalyst surface. The home-made sample holder realized this function. Figure 2-2 shows the details of the sample holder design. The main body of the holder is made of molybdenum and glass-ceramic (Macor). The molybdenum part works as the framework of the sample holder. Two chamfered edges on the sides make it possible to slide the holder into the rails at the desired places in the chamber. The Macor part is insulator. A one side polished square-shaped Si single crystal wafer with side length of 15 mm and thickness of 0.5 mm is used as the heater for resistive heating. It is placed in a 16×16 mm² indentation with depth of 2 mm in the Macor. The opposite edges on the back side of the Si wafer contact two molybdenum electrodes, respectively. When current flows over the extended electrodes, the Si wafer can be heated up so that the temperature of the sample that is closely attached to the Si wafer will also increase. In the case of metal sample, a thin insulator layer, typically a both sides polished $15 \times 15 \times 0.2$ mm³ Al₂O₃ single crystal, is used to isolate the sample. There are 4 delicate slides with screws on the corners of the indentation to fix the sample and press it tightly

to the Si wafer. The thermocouple wires (typically K-type, but possible for other types) are contacted to the edge of the sample surface through two tiny holes on one of the slides. In the practical experiments, a PID controller and a DC power supply can be connected to the extended feedthroughs for sample heating and thermocouple. Therefore, the temperature of the sample surface can be monitored and controlled precisely from room temperature to 1000K under UHV or reaction conditions.

[ion gun]

Catalyst surfaces, especially transition metal surfaces always subject to contaminants, which is a severe issue for the characterizations by surface science approaches. These surface contaminants can be sputtered off together with the substrate top layer by bombardment of the surface by noble gas ions, Ar^+ for instance. As shown in Figure 2-1, an ion gun is attached to the main chamber for surface cleaning. Argon gas is introduced through a variable leak valve directly into the ion gun. Figure 2-3 shows the basic concept of the ion gun. The gas atoms are ionized via electron impact in the ionizer of the ion gun. The produced ions are accelerated to the desired energy (typically, 0.5 ~ 5.0 keV) and directed towards the sample. Although ion sputtering is an effective technique to remove the contaminants from the surface, the surface structure of the sample has also been degraded. It would be a problem especially in the case of single-crystal surfaces. Therefore, subsequent annealing process is required to recover the surface crystallography and to remove implanted and adsorbed argon atoms. In practice, several ion sputtering and annealing cycles are required to prepare a well-ordered atomically clean surface.

[metal deposition system]

Oxide-supported metals play a very important role in heterogeneous catalysis. They generally consist of active transition-metal species that are highly dispersed on oxide supports. The UHV metal deposition system is therefore required to prepare the model catalysts for such materials. In the main chamber, several types of UHV deposition modules can be attached depending on the desired deposition materials. For instance, copper has relatively low melting point (1358 K), a home-made resistive heating evaporator can be used to make copper vapor for vacuum metal deposition. As shown in Figure 2-4, a curly spring shaped tungsten wire with thickness of 0.35 mm is used as the resistive heater. An ultra-thin copper wire (thickness: 0.02 mm) is rolled on the curly tungsten wire. The two edges of the tungsten wire are fixed to thick electrodes, which are typically made of copper. The deposition rate can be optimized by adjusting the current that flows through the tungsten wire. The customized tube and mask, which can specify the deposition area to the sample surface effectively, are attached to the vacuum side of the evaporator. On the other hand, some noble but frequently used metals, such as platinum and palladium have relatively high melting point, A commercial electron beam evaporator becomes a prefer candidate. Take platinum as an example, the high purity Pt rod is fixed in a hearth and heated by a high-current electron beam. The electrons are generated by thermionic emission from a hot filament placed close to the hearth. They are then accelerated by applied high voltages to hit the material surface. As a result of local melting and the materials evaporates. The deposition rate can be easily controlled by adjusting the emission current and the deposition duration can be determined by the open/close status of the shutter.

[XPS]

To qualitatively and/or quantitatively understand the surface components and chemical states of the catalysts, an XPS/AES is attached to the main chamber. It consists of a light source that emit aluminum $K\alpha$ and manganese $K\alpha$ X-rays and a hemispherical electron energy analyzer.

[LEED]

The main chamber is also equipped with a LEED, because when we use the single-crystal surface as the model catalyst, LEED pattern provides useful information on the crystalline structure and adsorbates of the well-ordered catalyst surface.

[Gas doser and TPD]

Heterogeneous catalysis on surface involves adsorption, diffusion, reaction, and desorption processes of the gases. The combination of a gas doser and a temperature programmed desorption (TPD) can satisfy our curiosity to the understanding of the desorption properties and surface kinetics of the adsorbed species on the catalyst surface. Therefore, a home-made gas cylinder and doser is attached to the main chamber (Figure 2-1). It can backfill the main chamber with the desired gas to some predetermined pressure for a measured length of time controlled by the variable leak valve. The TPD data can be acquired by a quadrupole mass spectrometer (MKS) that is placed behind an aperture in a differentially pumped (by a nonevaporable getter pump) chamber. This can improve the data quality by reducing the background pressure in the detector and ensuring that the detected species desorb directly from the sample rather than from the sample holder, chamber walls or any other surfaces.

2.2 Polarization-Dependent Total Reflection Fluorescence X-ray Absorption Fine Structure Technique

[XAFS]

X-ray Absorption Fine Structure (XAFS) is a powerful element specific X-ray Absorption Spectroscopy (XAS) to reveal atomic scale information with high sensitivity. In an X-ray absorption process, a beam of X-ray with a certain energy E irradiates the sample, some X-ray photons are absorbed by atoms in the sample and result in the excitation or ejection of core electrons of the atoms [1]. The absorption at this energy point can be simply quantified by measuring the intensity of incident and transmitted X-ray as follows,

$$A = \frac{I_t}{I_0} = \exp(-\mu t)$$

1 - 2

where A , I_t , I_0 , μ , and t represent absorption, intensity of transmitted X-ray, intensity of incident X-ray, absorption coefficient and thickness of the sample, respectively. X-ray absorption spectrum, $\mu(E)$ in typical case, is supposed to be obtained by scanning the photon energy in the range where core electrons can be excited. Generally, as the photon energy increases, a decreasing trend curve with several sudden increases, which were called absorption edges, at specific energies can be obtained. The locations of absorption edges are characteristic of the atoms irradiated by the X-ray. If we magnify the area around an absorption edge, the specific fine structure features are supposed to be observed. It is due to the ejected electron is scattered from the neighbor atoms around absorbing atom and the interferences occur between the outgoing and scattered electron wavefunctions. It contains very local structure information on neighboring atoms such as

bond distance, coordination number and thermal motions. In this sense, XAFS can be applied not only to crystals, but also to materials with short-range order like amorphous. Moreover, the high penetration of hard X-ray in air and most liquids makes *in situ* and *operando* XAFS techniques possible.

XAFS can be divided into two regimes: X-ray Absorption Near Edge Structure (XANES) and Extended X-ray Absorption Fine Structure (EXAFS) as shown in Figure 2-5. XANES generally covers the energy range starting from pre-edge up to 20 or 30eV above the edge and it is sensitive to the electronic structure of the unoccupied levels and coordination symmetry of the absorbing atom [2]. It involves an electron transition process, whose probability is usually dominated by selection rules, from an atomic core level to an unoccupied electronic state. Especially, for some L_{2,3}-edges of transition metals, the dipole allowed transitions between 2p to nd lead to a sharp intense peak referred as “white line” (WL) in the XANES region.

EXAFS usually starts from the end of XANES and extends several hundred eV further. The origin of this phenomenon is the interference of an electron with itself. In this energy range, the electron has been ejected out of the absorbing atom after absorbing a photon and propagates as a wave in all directions. Consequently, the electron wave can be scattered back by nearest atoms through the path from which it comes [3]. As the wavenumber of photoelectron increases, constructive and destructive interferences alternately arise, which leads to a change in electron density around the absorbing atom. As a result, the quantity of absorption coefficient starts to oscillate up and down in the EXAFS region. Therefore, it contains the structural information of the surrounding environment (generally up to $\sim 6\text{\AA}$) of the absorbing atom, including the elements,

coordination number, bond distance of neighboring atoms. The oscillation of EXAFS was quantitative parametrized by Sayers et al. in 1971[4] as:

$$\chi(k) = \frac{\mu(E) - \mu_s(E)}{\mu_0(E)} = S_0^2 \sum_i N_i \frac{F_i(k)}{kr_i^2} \sin[2kr_i + \phi_i(k)] e^{-2k^2\sigma_i^2} e^{-\frac{2r_i}{\lambda_i(k)}}$$

1 - 3

$\mu(E)$ – Absorption coefficient	m – Electron rest mass
$\mu_s(E)$ – Smooth ingredients of $\mu(E)$	\hbar – Reduced Planck constant
$\mu_0(E)$ – Absorption edge height	$F_i(k)$ – Back scattering amplitude
S_0^2 – Intrinsic loss factor	$\phi_i(k)$ – Back scattering phase shift
N_i – Coordination number	$\lambda_i(k)$ – Mean free path
k – Wave number	r_i – Bond distance
E_0 – Absorption Edge energy	σ_i^2 – Debye Waller factor
E – Incident X-ray energy	

It included most of the structural information we can extract from the EXAFS spectrum. Therefore, common methods for analyzing EXAFS spectrum are based on this EXAFS equation.

[polarization dependence of XAFS]

Conventional XAFS gives the average structural information over all spatial directions, therefore it is difficult to obtain accurate 3D and interface structures of the dispersed

metal species on the oxide surface. However, if we apply XAFS to such metal species on a model catalyst surface, for instance, an oxide single-crystal surface, more information regarding the 3D structure of supported metal species can be obtained. Because EXAFS oscillation $\chi(k)$ at K and L edges have the polarization dependence as shown in Figure 2-6.

For K and L₁ absorption edges,

$$\chi_{obs}(k) = \sum_i 3 \cos^2 \theta_i \cdot \chi_i(k)$$

1 - 4

For L₂ and L₃ absorption edges,

$$\chi_{obs}(k) = \sum_i (0.7 + 0.9 \cos^2 \theta_i) \cdot \chi_i(k)$$

1 - 5

where θ_i is an angle between the polarization vector \vec{E} of the incident X-ray and the bond vector as shown in Figure 2-6. Since the conventional supported metal catalysts are used in a powder form, the EXAFS oscillations are averaged over all directions. On the other hand, when the flat oxide substrates like single crystals are used, the structural information parallel and perpendicular to the surface can be separately obtained by the polarization-dependent EXAFS measurements (Figure 2-7). When the polarization vector is parallel to the surface (s-polarization), EXAFS will provide information on the bonds parallel to the surface. When the polarization vector is perpendicular to the surface (p-polarization), the information about the structure perpendicular to the surface, i.e., the

metal-support bond is mainly obtained [5]. Using a polarized x-ray and flat sample, one can obtain the three-dimensional information by EXAFS.

[total reflection fluorescence XAFS]

When we measure the XAFS, especially EXAFS, of the metal species dispersed on oxide single-crystal surface, the low concentration of the metal species would be a severe problem. The concentrations of sub-monolayer metal films are in the range of $10^{13} \sim 10^{15}$ atoms per centimeter square, which is 4 ~ 6 orders of magnitude lower than the concentrations of metal species in the case of commonly used catalysts in a powder form. If the transmission detection mode was applied to the single-crystal oxide-supported metals, the signal to background (S / B) ratio in the transmitted x-ray would be very low, because of the X-ray absorption by the oxide support is much higher than that of the target metal species. The S / B ratio might be 10^{-5} or less of the powdery sample, which has high surface area. It means that it is impossible to obtain meaningful EXAFS signal by a transmission mode. Therefore, EXAFS and surface sensitive techniques must be combined to apply it to a single-crystal oxide model system.

The Auger electron yield XAFS is a surface sensitive technique that detects EXAFS by monitoring the Auger electron intensity [6]. However, the Auger yield is largely affected by the inelastic photoelectron background, which is generated by the oxide support, and leads to the low S / B ratio. At the same time, high vacuum is required for the Auger electron detection, which makes *in situ / operando* measurements difficult [7]. Therefore, to realize the measurements that can be conducted under reaction environments on single-crystal surfaces, other surface sensitive X-ray techniques are demanded, such as total reflection and fluorescence detection mode.

The X-ray fluorescence detection mode is a proper method to increase the sensitivity of XAFS measurements. Figure 2-8 shows the principle of the fluorescence detection mode of EXAFS measurements. The core hole is generated by X-ray absorption following the photoelectron emission. The core hole has a high energy state so that an electron transition occurs from the outer shell to fill and relax it. This relaxation process is accompanied by fluorescence X-ray radiation.

Since the deposited metals are only present at surface, the signal from the substrate is just the background signal. To reduce this background signal as shown in Fig. 2-9, total-reflection mode was adopted. When the X-ray incident angle is less than the critical angle, the X-ray total reflection occurs, and the X-ray cannot penetrate into the bulk. The total reflection condition decreases the emission of scattered X-rays from the bulk and improves surface sensitivity.

As a result, Polarization dependent Total-Reflection Fluorescence XAFS (PTRF-XAFS) is a technique to give three-dimensional information (by using polarization dependence) on a high dispersed metal species on surface (by using total-reflection fluorescence).

2.3 Development of *operando* PTRF-XAFS system

The developed *operando* PTRF-XAFS cell realizes the following concepts:

(i) PTRF-XAFS measurements are possible under reaction conditions, i.e., at high temperatures (<800 K) and pressures (<0.1 MPa).

(ii) The internal volume of the cell is as small as a few hundred cubic centimeters to detect the products with the QMS.

(iii) The cell weight is less than 15 kg to set it on the goniometer used for adjustment of the total-reflection conditions of incident X-rays.

(iv) The cell can be connected to and detached from another UHV chamber for sample preparation and characterization with Ar⁺ sputtering, high-temperature annealing (<1200 K), evaporation of metal atoms, and surface science techniques such as LEED/AES and XPS.

As it was introduced in Chapter 1, the PTRF-XAFS measurements required high flux and energy X-rays that can only be generated by synchrotron radiation facilities. It means we must prepare the samples in the facility. Another UHV system was therefore settled in the Photon Factory at the Institute of Materials Structure Science (KEK-IMSS-PF, Tsukuba, Japan). It has basically the same functions as the lab one. Figure 2-10 shows schematic diagrams of the sample transfer from the UHV sample preparation chamber to the *operando* PTRF-XAFS cell, respectively. A single-crystal sample (15 × 15 × 0.5 mm³) is first fixed to the above-mentioned sample holder where a Si wafer of the same size is placed on the backside of the sample as a heater, and the K-type thermocouple wires (made of Chromel and Alumel) are contacted with the edge of the sample surface (see the details in Figure 2-2). The sample is then introduced into the UHV sample preparation chamber (Figure 2-10). Standard procedures for sample surface cleaning such as Ar⁺ sputtering and high-temperature annealing (<1200 K), metal deposition using a UHV evaporator, and surface characterization by LEED/AES and XPS can be performed in this chamber. After preparation, the sample is transferred to the *operando* PTRF-XAFS cell using magnetic transfer rods through the sample parking chamber, where up to three samples can be stored in a specially designed sample holder storage stacker. The cell is

then detached from the UHV system, as shown in Figure 2-10, with its gate valve closed after activation of a nonevaporable getter (NEG) pump (Capaci- Torr-D100, SAES) attached to the cell.

Figure 2-11 shows details of the *operando* PTRF-XAFS cell. After detachment of the cell from the UHV system, the ICF70 flange with a Be window (effective area, 30 mm diameter; thickness, 200 μm ; purity, >99.8%) and the L-shaped evacuation line with an ICF34 gate valve is attached to the ICF70 gate valve of the cell, as shown in Figure 2-11a. The Be window on the ICF 70 flange is used to detect the fluorescence signal for the s-polarization XAFS measurements together with the other Be window on top of the cell for the p-polarization measurements. The L-shaped vacuum line is used to evacuate the cell with a TMP and a DP. The cell also has two more Be windows (effective area, 10 mm diameter; thickness, 200 μm ; purity, >99.8%) attached to the ICF34 flanges (see Figure 2-11b), through which incident and reflected X-rays pass. The sample in the cell can be heated at <800 K by the substrate Si heater, and the surface temperature can be monitored using the K-type thermocouple. A gas inlet line and pressure gauge (capacitance manometer, MKS) are also attached to the cell to introduce reactant gases at a desired pressure (typically of $10 \sim 10^2$ Pa order, but possibly up to 0.1 MPa). The internal volume in the cell is 216 cm^3 when the two ICF34 gate valves and the bellows-sealed valve illustrated in Figure 2-11b are closed. Product analysis is conducted by gas-sampling and QMS measurement through the variable leak valve. The total weight of the cell is approximately 12 kg.

Operando PTRF-XAFS measurements can be conducted after the cell is fixed to the 6-axis goniometer ($x, y, z, \theta, \phi, \psi$) placed in the hutch of the beamline, which enables

optimization of the total-reflection conditions for the incident X-rays, as shown in Figure 2-12. For s-polarization measurements, z motion and ϕ rotation are mainly used to achieve the total-reflection conditions, while x motion and ϕ rotation are adjusted in p-polarization measurements after rotation of the cell by 90° using ψ rotation. The fluorescence signal from the sample surface is extracted through the Be windows (ICF70) attached to the cell and detected using the 19-element solid-state detector (GL0110S; Canberra, USA) during scanning of the incident X-ray energy to measure a fluorescence XAFS spectrum. The positions of the Be windows are in line with those of the SSD windows to obtain maximum efficiency for collection of the fluorescence signal.

2.4 Modification from the batch-type to flow-type cell

The batch-type cell is a closed system, which makes the products accumulate in the cell and can be easily detected. However, for a certain catalytic reaction, reactant gases are consumed, and products are generated continuously, so that the partial pressures of the gases change as reaction time goes by. For high active catalysis, partial pressure of the reactant/product gases inside the reactor drastically change in short time and this may induce a structural change of the catalysts during accumulation of the XAFS data. Therefore, a flow-type reactor, which enabled us to monitor the 3D structure of the supported metal species under steady state span over the long XAFS measurement periods especially of highly active catalysts, is demanded.

Figure 2-13 shows the concepts of the modified cell. The gas inlet lines were attached to the cell via a 1/4-inch VCR stainless steel (SUS) tube. It consisted of up to two high pressure steel cylinders that can supply ultra-pure reactant gases, two mass flow controllers (MKS, full range: 10 sccm) that can control the flow rate of reactant gases to

the low-pressure side at desired values, a evacuation line that was connected to TMP and DP for pre-evacuation of the gas inlet lines. A TMP and DP set was also connected to the cell outlet via the ICF70 flange to establish the gas-in and -out flow system. A SUS tube with the diameter of ½ inch was attached to the top of the cell via a linear motion manipulator (AVC, ALMB-133/30) as the sampling tube. It realized the Z-motion so that the sampling tube can approach to the sample surface at a desired distance to collect the products near the surface without inhibition of the mass transfer between the atmosphere and the sample surface. The other side of the sampling tube was attached to a variable leak valve that can control the flow rate of the sampling gases precisely to the QMS for component analysis. A compact electron cyclotron resonance (ECR) plasma source can be attached to the cell via an ICF70 port so that the plasma-assisted catalytic reactions are applicable by using the upgraded flow-type cell.

2.5 Data analysis method for PTRF-XAFS

The flowchart for the analysis procedure of PTRF-EXAFS is summarized in Figure 2-14. In order to estimate the coordination number and bond distance in each polarization, we need to analyze the s- and p-polarization EXAFS oscillation by carrying out with background removal, normalization, Fourier transform and curve fitting procedures, respectively. Some real space candidate model structures can be then assumed according to these coordination number and bond distance information. By comparing the observed EXAFS spectrum with the oscillation calculated based on the candidate models in different polarizations, the preferable structures can be selected.

For EXAFS analysis, REX2000 (Rigaku Co., Japan) was used as follows [8].

Firstly, the raw EXAFS data obtained from beamline listed the absorption coefficient μ as the function of photon energy E . While the EXAFS oscillation χ is expressed by the sine function of the wavevector of a photoelectron k . Thus, we need to convert the horizontal axis from photon energy to the wavevector of a photoelectron by the following equation:

$$k[\text{\AA}^{-1}] = \sqrt{\frac{2m}{\hbar^2}(E - E_0)} = \sqrt{0.2625(E - E_0)[\text{eV}]}$$

2 - 6

where E_0 is the energy that necessary to emit the core level electron as a free photoelectron. However, there are several ways to determine the E_0 from the experimental data because it is affected by the chemical and valence state of the sample. From the point view of operability, therefore, we temporarily took the inflection point of the edge as the E_0 and optimized the edge shift ΔE in the curve fitting procedure. Then, the EXAFS oscillation needed to be extracted by background removal and rescaling using the following equation:

$$\chi(k) = \frac{\mu - \mu_s}{\mu_0} = \frac{(\mu - \mu_{pre}) - \mu_{post}}{\mu_0}$$

2 - 7

where μ , μ_s and μ_0 are the observed absorption coefficient, its smooth part and edge jump, respectively. The μ_{pre} represents the pre-edge absorption, which is fitted and extrapolated

to the EXAFS region using the Victoreen equation. However, when the I_0 and I_1 are measured by different detectors, a constant should be added as follows:

$$\mu(\lambda) = C\lambda^3 + D\lambda^4 + A$$

2 - 8

The μ_{post} is the gradual decreasing region after edge jump and can be estimated by smoothing out the oscillatory part of the data using Spline smoothing method. The criteria for automatic background removal were proposed by Cook and Sayers. It involves three parameters, H_R , H_N and H_M . They are the height of residual background which is determined by the average value of Fourier transform magnitude between 0.00~0.25 Å, the height of noise which is expressed by the average value of Fourier transform magnitude between 9.0~10.0 Å, and the height of main peak which is represented by the maximum value of the Fourier transform between 1.0~5.0 Å, respectively. Generally, the following relation should be satisfied.

$$H_R - H_N \geq 0.05 H_M$$

2 - 9

while

$$H_R > 0.1 H_M$$

2 - 10

should be used if the spectrum has bad signal to noise ratio (S/N), such as $H_N > 0.1 H_M$.

Then the EXAFS oscillation $\chi(k)$ was weighted by k^n to diminish the quick damping of oscillation at high- k region due to the affect from Debye Waller factor. The sinusoidal-like EXAFS oscillations were further Fourier transformed to r -space and gave a pseudo-radial distribution function.

$$\rho(r) = \int_{k_{min}}^{k_{max}} k^n \cdot \chi(k) w(k) e^{2ikr} dk$$

2 – 11

The resolution of the Fourier transform improves while the transformed range increase. However, the k -region lower than 2~3 Å⁻¹ EXAFS is much affected by multiple scattering. Therefore, k_{max} should be extended as large as the S/N=1.

By applying Fourier transform to the EXAFS oscillations, different shells can be separated using the window functions $w(k)$. The Hanning window was used in this analysis, for instance.

$$w(k) = \begin{cases} \left[1 - \frac{\cos(\pi(k-k_{min}))}{2d}\right] & k_{min} < k < k_{min} + d \\ 1 & k_{min} + d < k < k_{max} - d \\ \left[1 - \frac{\cos(\pi(k_{max}-k))}{2d}\right] & k_{max} - d < k < k_{max} \end{cases}$$

2 - 12

where d should be 5 ~ 10% of the whole transformed range because if d is large, the peak height becomes smaller and broader although the side lobe is smaller.

Then, the curve fitting is usually performed to fit bond distance, coordination number, Debye Waller factor and other parameters by the non-linear least square method. In addition to that, the edge shift ΔE also needs to be optimized because the original point of kinetic energy of photoelectron E_0 in unknown compounds is not exact the same value used for the calculation of phase shift and amplitude functions. Another thing we need to keep in mind is that in the curve fitting procedure of PTRF-XAFS, the information that derived from each polarization direction is in principle one-dimensional. However, the bond distance, Debye Waller factor and E_0 should be consistent for all polarization directions. Finally, the goodness of fitting can be indicated using R_f value which is expressed by the following formula:

$$R_f = \frac{\sum\{k^n \chi_{obs}(k) - k^n \chi_{cal}(k)\}^2}{\sum\{k^n \chi_{obs}(k)\}^2}$$

2 - 13

Generally, smaller R_f value represents a better fitting, but not completely. We still need to consider the physical interpretation of each parameter and bound them within reasonable ranges.

There're many limitations on obtaining structural information using curve fitting. One is the degree of freedom, M , for fitting parameters is determined by Nyquist theory [9]

$$M = \frac{2\Delta k \Delta r}{\pi} + \alpha \quad (\alpha = 0, 1, 2)$$

2 - 14

Here, Δk and Δr are the regions selected for fitting in k-space and r-space (by Fourier transformation), respectively. It requires the number of fitting parameters used in curve fitting to be less than M . However, curve fitting is a path specific method that each scattering path has its own fitting parameters. Although not all parameters are independent among different paths, it can be certain that the more paths are included in curve fitting, the less parameter can be used giving the constant M .

In order to estimate the white line intensity of Pt species, REX2000 was also applied to the analysis of XANES. Similar procedures were conducted such as background removal and rescaling. However, a constant value of background was used due to the short pre-edge. The white line of Pt L_3 -edge was considered as the sum of the arctangent term, which was caused by the transitions to the continuous state, and the Lorentz distribution (or Gaussian distribution) of absorption peak. Consequently, the white line intensity can be then derived by fitting the white pattern and integrating the absorption peak.

By considering the coordination number and bond distance that derived from EXAFS in each polarization direction, a series of 3D model structures in real space can be constructed as candidates.

FEFF is a program [10] that calculates X-ray absorption spectra and electronic structure from a certain known structure of cluster. The output includes EXAFS, XANES, X-ray natural and magnetic circular dichroism (XNCD and XMCD), non-resonant X-ray emission spectra (XES). In this work, I used FEFF to calculate the polarization-dependent EXAFS oscillation of the corresponding model structure candidates in s- and p-polarizations, respectively.

To judge how well the calculated spectra fit the experimental one, the following criteria were applied. The R^2 value, which is expressed as equation 2 - 15, of each polarization of each model structure was calculated and compared with unity. If the R_f value of a certain model structure is less than 1, the model will be considered as a plausible one.

$$R_f = \frac{1}{N} \sum \left(\frac{\chi_{obs}(k_i) - \chi_{cal}(k_i)}{error(k_i)} \right)^2$$

2 - 15

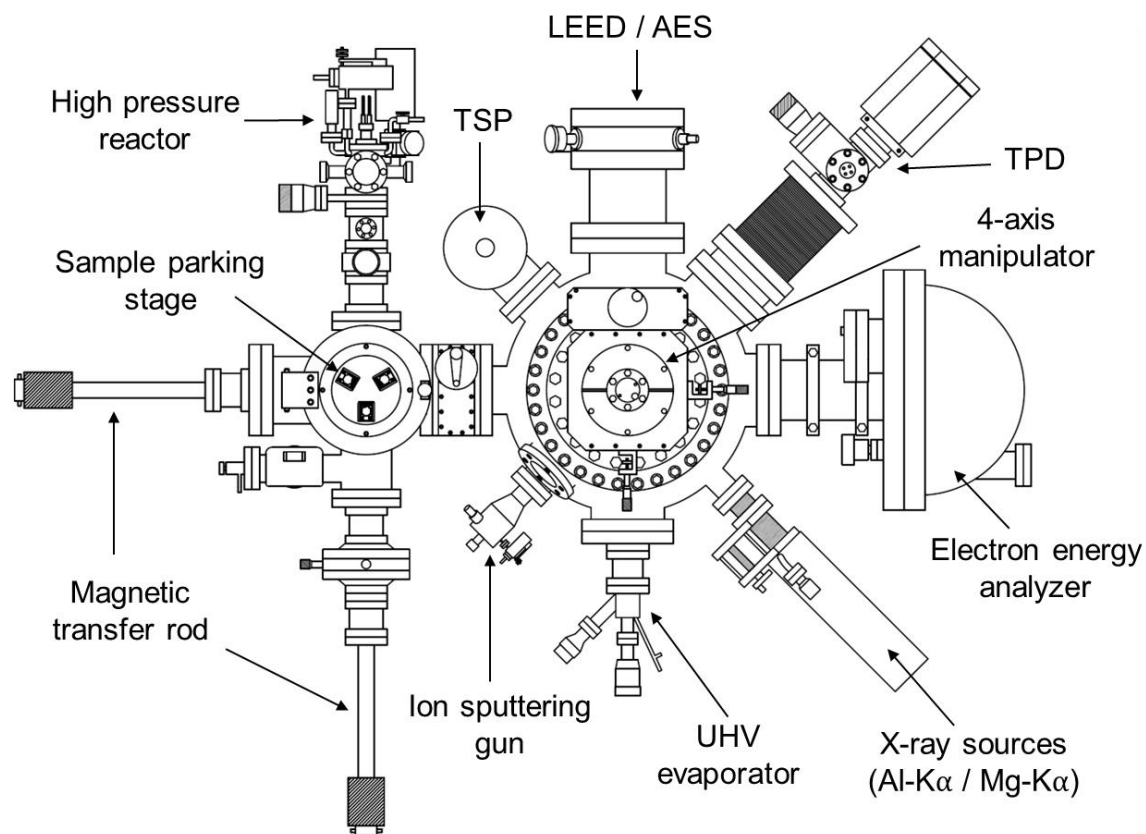


Figure 2-1. The schematic of the integrated UHV system for the sample preparation and multiple characterizations.

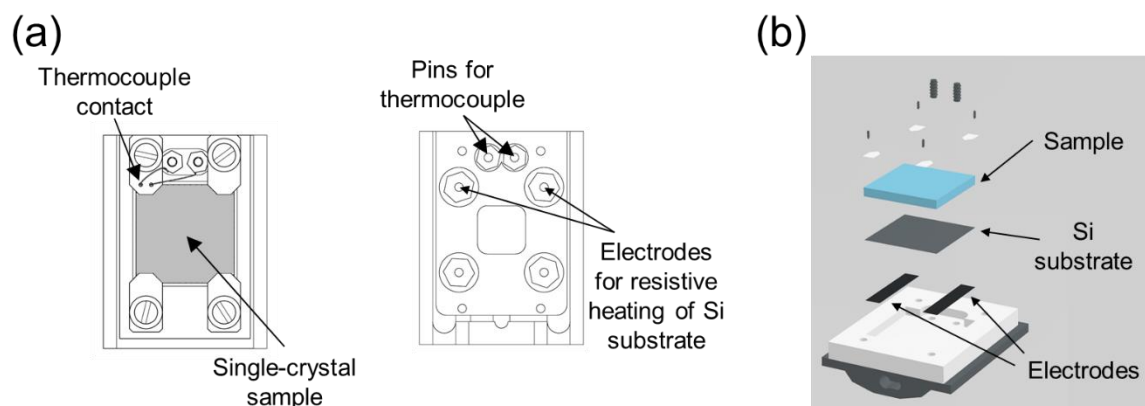


Figure 2-2. (a) Schematic of both the front and back sides of the sample holder. The main body is made of molybdenum, and other insulating parts are made of alumina and Macor. (b) Sample and Si substrate setup to the sample holder.

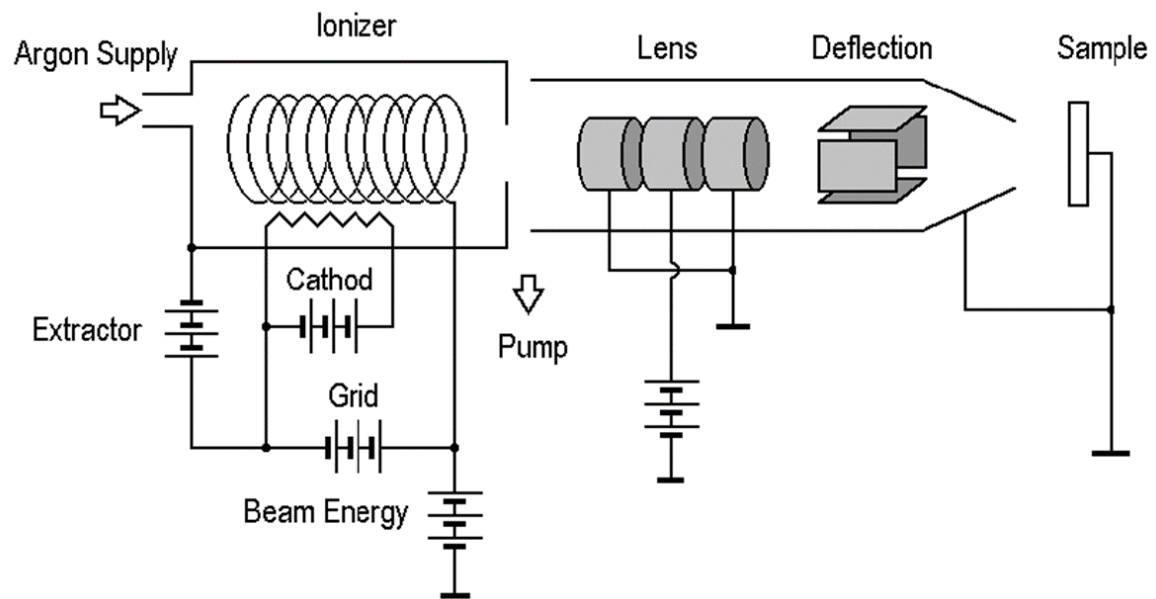


Figure 2-3. Schematic diagram showing a typical ion sputter gun used for sample cleaning.

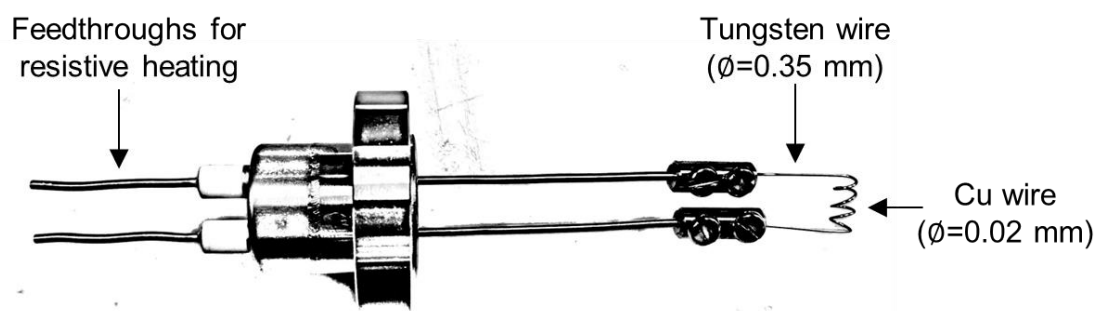


Figure 2-4. Photo of the home-made vacuum evaporator for Cu deposition.

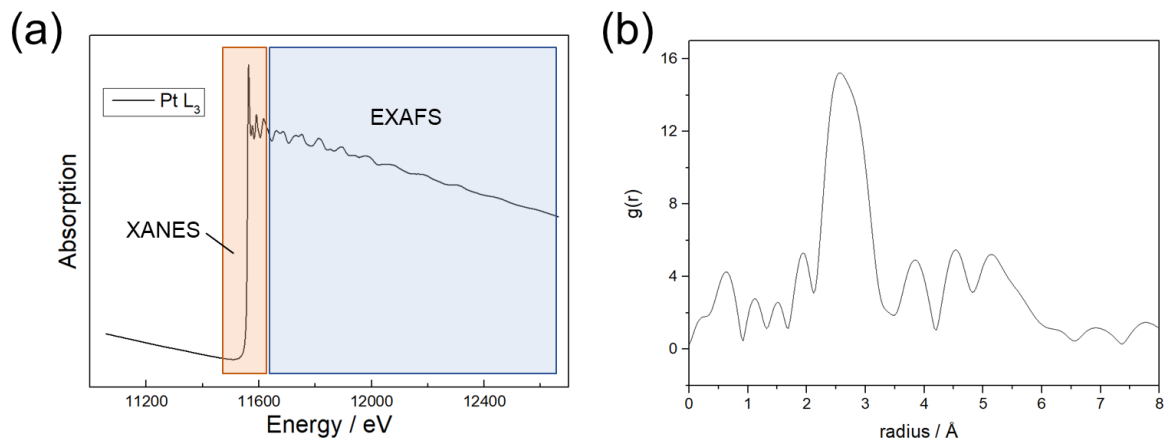


Figure 2-5. (a) XAFS of Pt at L₃ edge and (b) its Fourier transformed distribution in r-space.

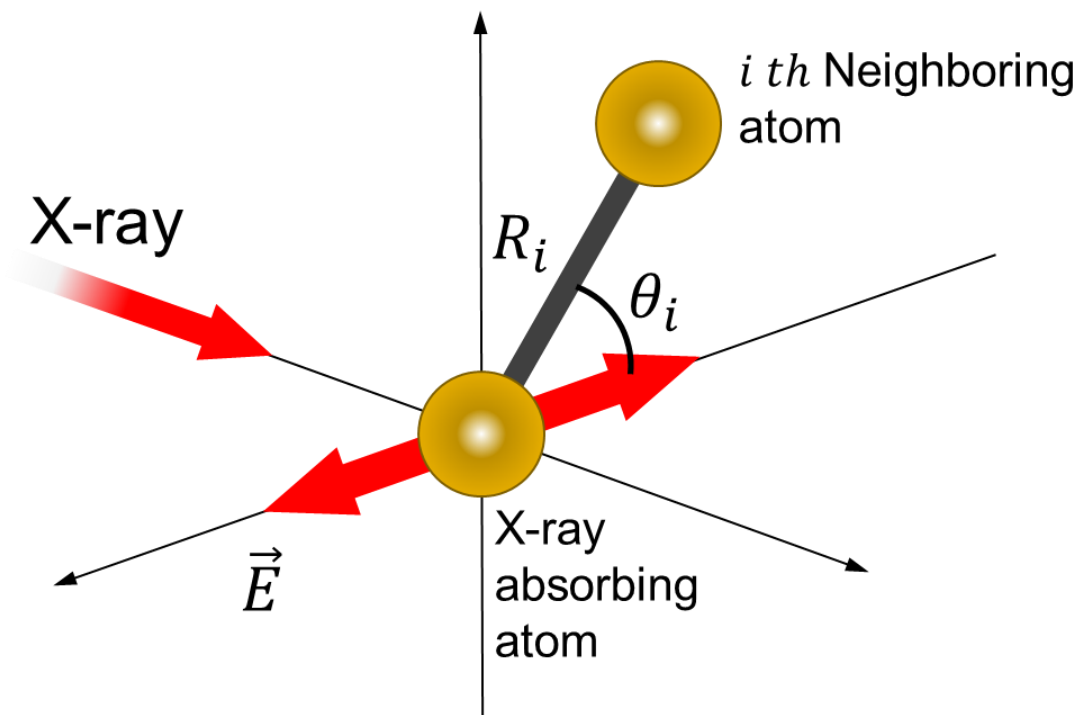


Figure 2-6. Polarization dependence of XAFS oscillation $\chi(k)$.

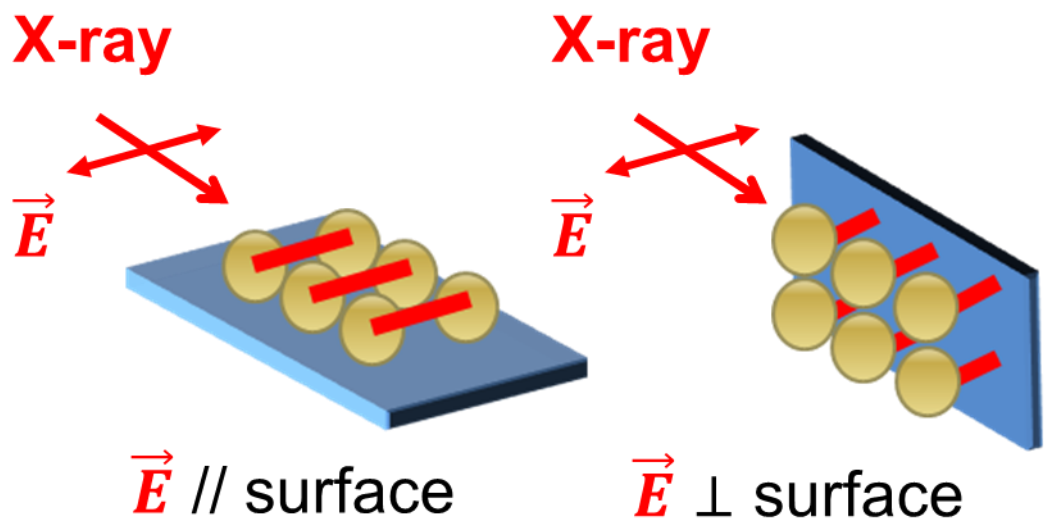


Figure 2-7. PTRF-XAFS measurements by sample rotation.

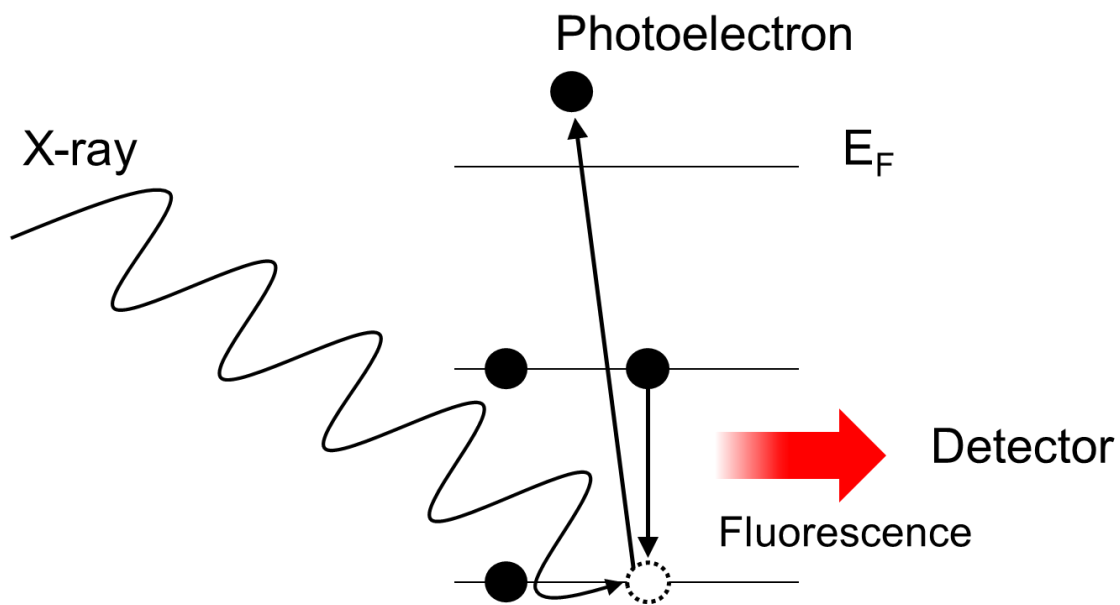


Figure 2-8. The fluorescence detection mode of XAFS measurements.

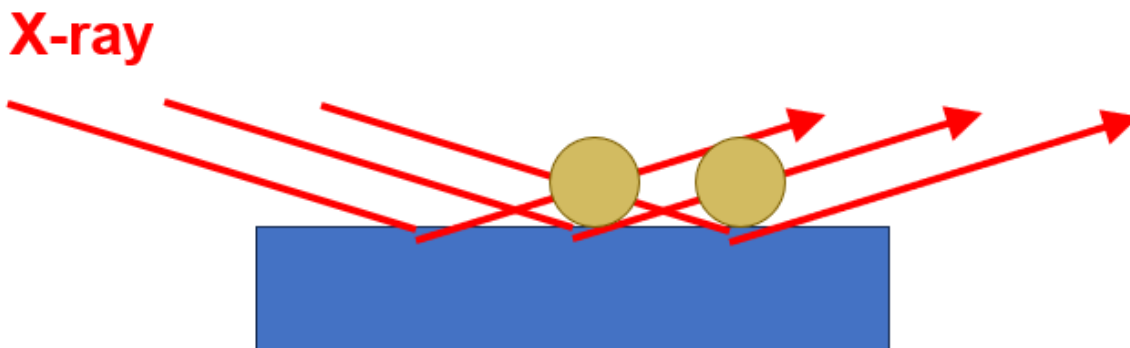


Figure 2-9. The fluorescence detection mode of XAFS measurements.

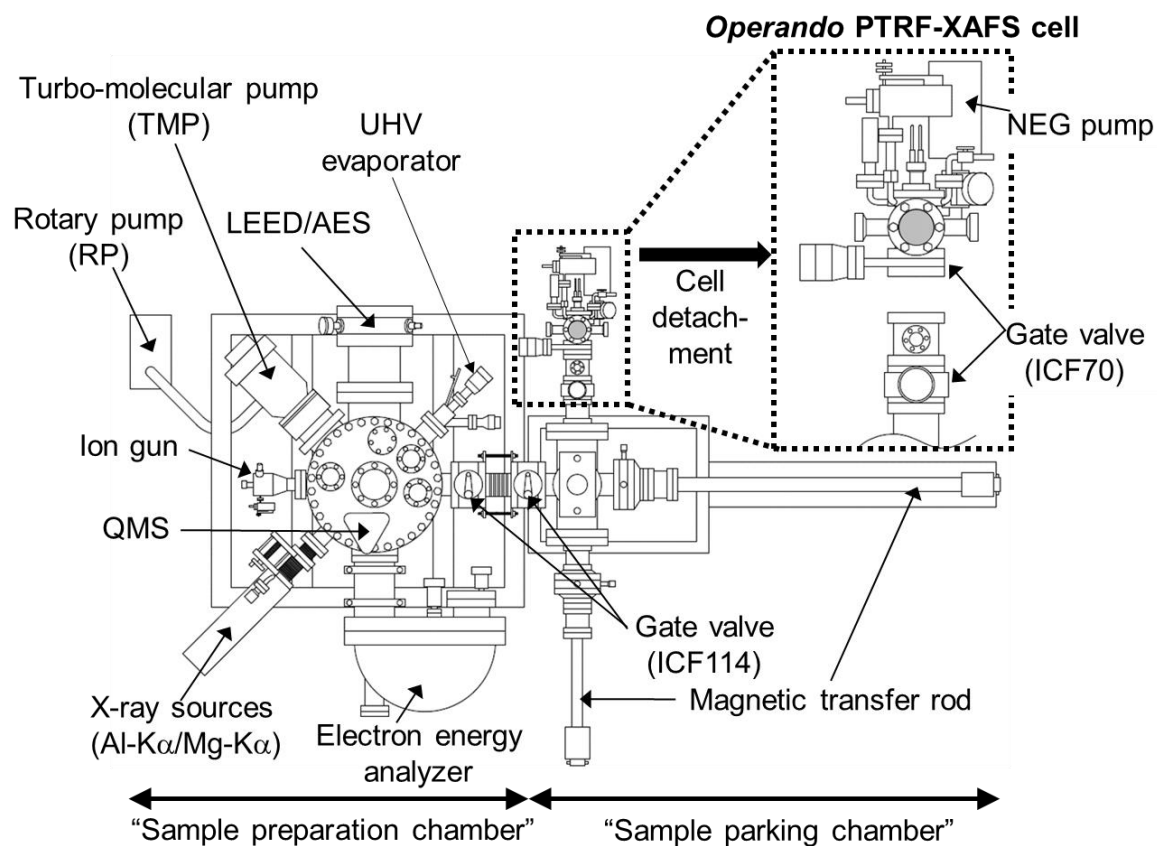


Figure 2-10. Sample transfer from the UHV sample preparation chamber to the *operando* PTRF-XAFS cell through the UHV sample parking chamber using magnetic transfer rods, followed by detachment of the cell.

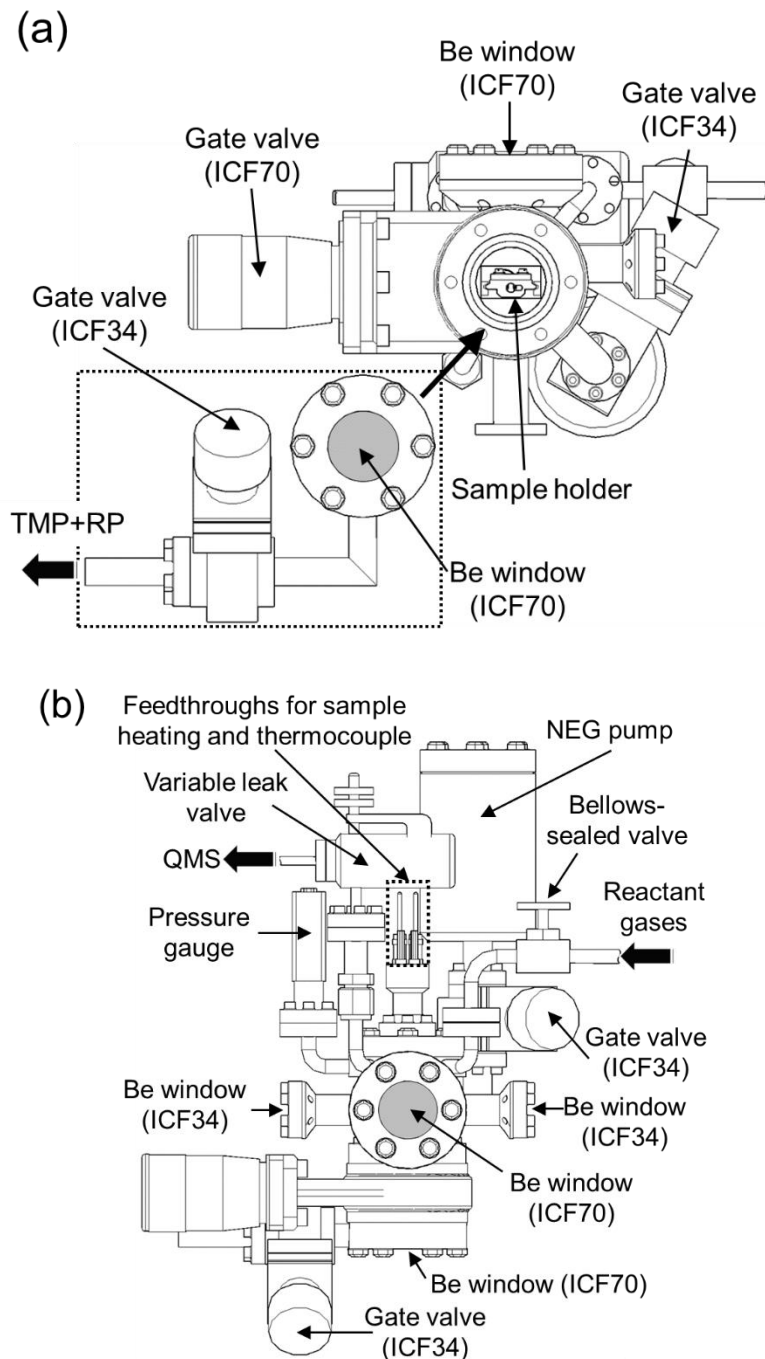


Figure 2-11. (a) Side view and (b) top view of the *operando* PTRF-XAFS cell. The sample holder is visible in panel a, although the gate valve (ICF70) is closed after the cell detachment from the sample parking chamber, as shown in Figure 16. For the dimension of the cell, note that the diameters of the CF flanges, ICF70 and ICF34, are 70 and 34 mm, respectively.

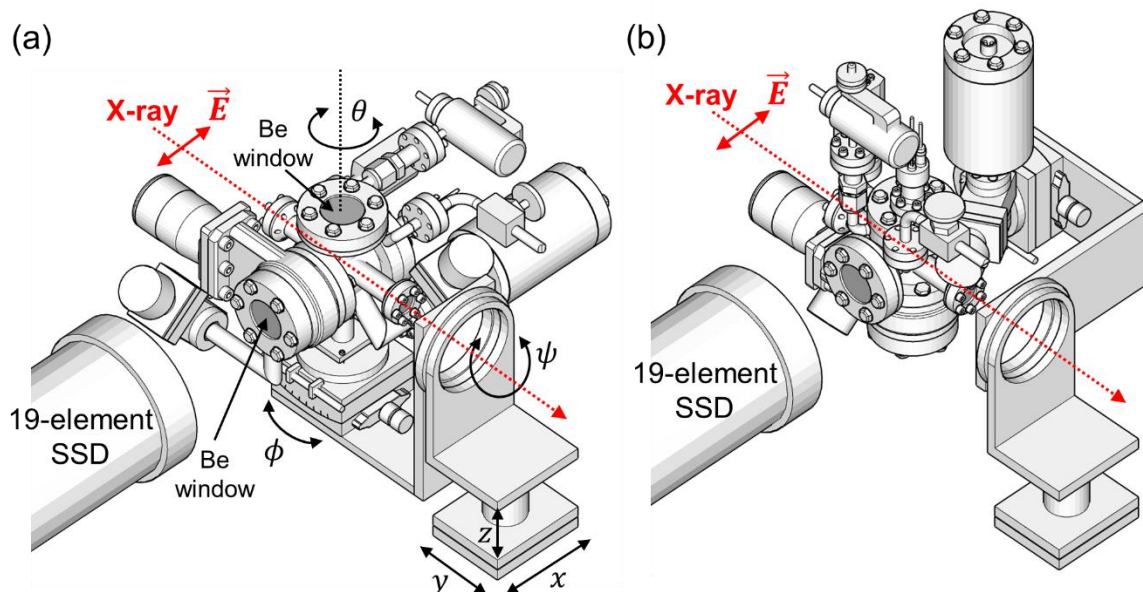


Figure 2-12. Attachment of the *operando* PTRF-XAFS cell to the 6-axis goniometer (x , y , z , θ , ϕ , ψ) and configuration for polarization-dependent fluorescence XAFS measurements; (a) s-polarization and (b) p-polarization.

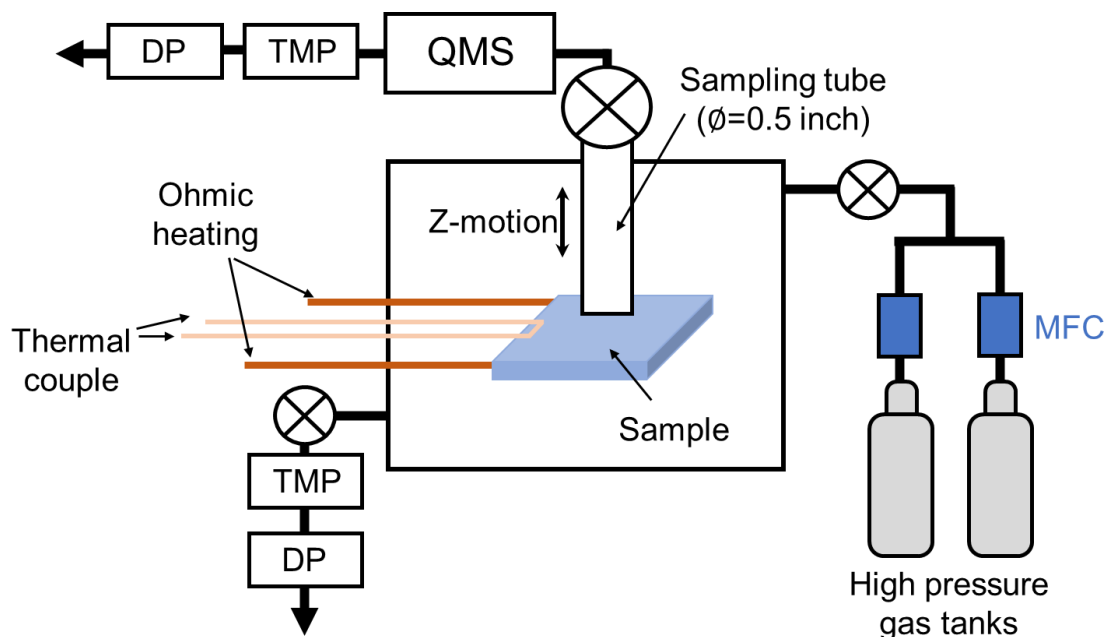


Figure 2-13. Schematic of the modified flow-type cell.

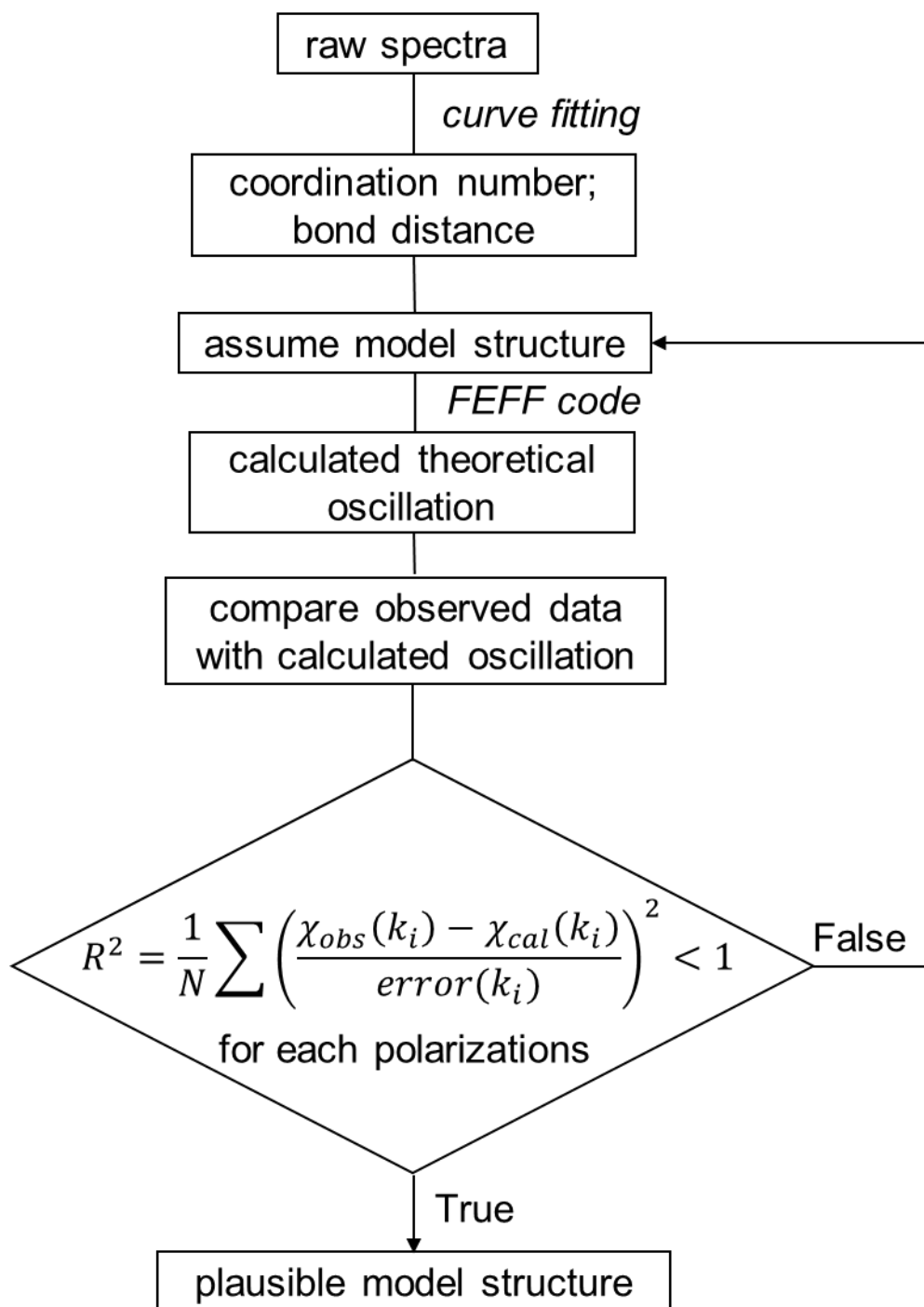


Figure 2-14. Flowchart for the analysis procedure of PTRF-EXAFS.

References

- [1] G. Bunker, *Introduction to XAFS: A Practical Guide to X-ray Absorption Fine Structure Spectroscopy*. Cambridge University Press, 2010, pp. 1-33.
- [2] Y. Iwasawa, K. Asakura, and M. Tada, *XAFS techniques for catalysts, nanomaterials, and surfaces*, Cham: Springer International Publishing, 2017, pp. 275-520.
- [3] D. C. Koningsberger and R. Prins, “X-ray absorption: Principles, applications, techniques of EXAFS, SEXAFS and XANES,” Jan. 1987, Accessed: Jul. 11, 2023.
- [4] D. E. Sayers, E. A. Stern, and F. W. Lytle, New technique for investigating noncrystalline structures: Fourier analysis of the extended x-ray—absorption fine structure. *Physical review letters*, vol. 27, no. 18, pp. 1204, 1971.
- [5] S. Takakusagi, W.-J. Chun, H. Uehara, K. Asakura, and Y. Iwasawa, “Polarization-Dependent Total-Reflection Fluorescence X-ray Absorption Fine Structure for 3D Structural Determination and Surface Fine Tuning,” *Top Catal*, vol. 56, no. 15, pp. 1477–1487, Nov. 2013.
- [6] D. C. Koningsberger and R. Prins, “X-ray absorption: Principles, applications, techniques of EXAFS, SEXAFS and XANES,” Jan. 1987, Accessed: Jul. 10, 2023.
- [7] M. Salmeron and R. Schlögl, “Ambient Pressure Photoelectron Spectroscopy: A new tool for surface science and nanotechnology,” *Surface Science Reports*, vol. 63, no. 4, pp. 169–199, Apr. 2008.

- [8] Y. Iwasawa, *X-ray Absorption Fine Structure for Catalysts and Surfaces*. World Scientific, 1996.
- [9] E. A. Stern, “Number of relevant independent points in x-ray-absorption fine-structure spectra,” *Phys. Rev. B*, vol. 48, no. 13, pp. 9825–9827, Oct. 1993.
- [10] A. L. Ankudinov, B. Ravel, J. J. Rehr, and S. D. Conradson, “Real-space multiple-scattering calculation and interpretation of x-ray-absorption near-edge structure,” *Phys. Rev. B*, vol. 58, no. 12, pp. 7565–7576, Sep. 1998.

CHAPTER 3
PLASMA-ASSISTED NITROGEN ADSORPTION AND
HYDROGENATION ON Co(0001) SURFACE

Nitrogen fixation is the process by which nitrogen is taken from its molecular form (N_2) and converted into nitrogen compounds useful for other chemical processes. The production of ammonia from nitrogen and hydrogen gases, known as Haber-Bosch process, is a conventional nitrogen fixation method that is used in industrial synthesis of ammonia. It is typically carried out over iron catalysts following elementary steps [1]:



where “[]” represents the adsorption site on the catalyst surface. The rate-determining step, which is the slowest step over the entire reaction process, is step 3 because the two nitrogen atoms in the molecule are strongly bonded with each other via the stable triple

bonds. The activation and breaking of the triple bonds of the N_2 molecule is a challenging task and usually needs high pressure and temperature conditions. Recently plasma technology has been applied to nitrogen fixation and its conversion to useful chemicals under mild reaction conditions [2, 3]. The alumina supported cobalt showed a distinctive reactivity towards the ammonia synthesis with the assistance of plasma [2]. However, their surface processes such as adsorption, reaction, and desorption including the rate-determining step are not clearly understood at present. In this work, I used Co foil and Co(0001) single-crystal surfaces for the plasma-assisted ammonia synthesis and conducted a thermodynamic and kinetic study for the nitrogen adsorption process under low temperature and low pressure conditions.

3.1 Kinetic Analysis of Plasma-Assisted Nitrogen Adsorption on Co(0001) Surface [cleaning of the Co(0001) surface]

An one-side polished square-shaped Co(0001) single crystal with the side length of 15 mm and thickness of 0.8 mm (Purity: 99.999+%) was used as the model catalyst surface. The cleaning treatment of the sample surface was performed in the above-mentioned UHV apparatus (refer to section 2.2). Prior to the first use, the Co(0001) surface was sonicated in acetone for 5 min, then fixed to the sample holder (refer to chapter2, Figure 2-2) where a Si wafer and a both sides polished α - Al_2O_3 (0001) single-crystal (Shinkosha Co., Ltd.) of the same size were placed on the backside of the sample as a heater and an insulator, respectively. The sample with the holder was then introduced into the UHV chamber. It is well-known that transition metal surfaces are subject to surface contamination [4]. The surface cleaning therefore is an indispensable procedure before the experiments. Generally, the surface contaminates can be removed by repeating

Ar⁺ sputtering and annealing cycles in UHV condition. Specifically, the whole cleaning procedure of the Co(0001) single-crystal surface needed to be done with great care, because the irreversible crystalline phase transition of the Co single crystal occurs easily from hcp to fcc at a temperature higher than 670 K [5, 6]. Furthermore, the high ion energy / sputtering angle may induce Ar [7, 8] atoms implanted into the bulk of the crystal during Ar⁺ sputtering and they are difficult to remove completely by the annealing process. The Ar⁺ sputtering was therefore conducted with the high voltage of 1.5 keV, Ar (Purity: 99.999%) pressure of 3.6×10^{-5} Pa at room temperature, and the annealing was done at 650 K in UHV ($\sim 1.0 \times 10^{-7}$ Pa). This procedure was repeated until no more oxygen, carbon, nor other contaminants were observed in XPS. The temperature of the sample was always kept below 660 K to avoid the phase transition. The symmetry of the clean Co(0001) surface structure was checked by low-energy electron diffraction (LEED) pattern (Figure 3-1). This procedure was repeated until XPS showed a clean surface..

The thermal reaction proceeds by the Langmuir-Hinshelwood mechanism have been described above, the rate-limiting process is step 3. While the plasma-assisted nitrogen adsorption may be accelerated (via the acceleration of step 3 and new pathway of step 9 and 10) by the formation of excited nitrogen species such as vibrationally excited nitrogen and nitrogen atoms.



where “*” represents the excited species. In this work, I focused on the nitrogen adsorption process and considered only atomic nitrogen and vibrationally excited

nitrogen molecules because they have advantages towards the adsorption process. In the case of nitrogen atoms, the stable triple bond in the molecule was already cleaved and they were ready to adsorb on the surface. The vibrationally excited nitrogen molecule had a weaker bond between the two nitrogen atoms. Their dissociation process and interaction with the Co surface was illustrated in Figure 3-2 [9]. Consequently, the following dissociation process on the Co surface was easier. To figure out the active species from the plasma phase for nitrogen adsorption on the Co surface, a temperature dependent experiment of plasma-assisted nitrogen adsorption was conducted.

Figure 3-3a, b shows the XPS N1s peak with the different N₂ plasma (N₂ flow rate: 0.5 sccm, pressure: 0.5 Pa, plasma power: 10 W) exposure time of the Co(0001) surface at 298 K and 318 K. The N1s peaks were normalized by the corresponding Co2p for each after background removal. This treatment was applied to all XPS N1s peak. There is no difference between the clean Co surface and the N₂ gas (N₂ flow rate: 0.5 sccm, pressure: 0.5 Pa) exposed Co surface. It indicated that the nitrogen molecule cannot “stick” to the Co surface at room temperature. However, N1s peak appears in the XPS spectra after the Co surface exposed to N₂ plasma at room temperature. A clear trend can be found that the amount of nitrogen species increases with the time of nitrogen plasma exposure. The broadening of the N1s indicated that multiple nitrogen species formed after nitrogen plasma exposure. Since the temperature is relatively low, the dissociative adsorption of unexcited nitrogen molecules due to the thermal effect is neglected. Figure 3-3c, shows the relation between the normalized peak area of the N1s and exposure time at different temperatures. The adsorption isotherm has the Langmuir type. The slope of the fitted line corresponds to the adsorption rate of nitrogen species on the Co surface. At time = 0, a

higher rate was observed at the higher temperature. This phenomenon indicates that thermal energy has a positive influence on the adsorption process of nitrogen from the plasma phase and suggests that the contribution from the dissociative adsorption of vibrationally excited nitrogen molecules. Because the adsorption of unstable atoms to the metal surface has generally no energy barrier while extra energy is needed in the case of dissociative adsorption of molecules [10]. Therefore, generally adsorption process is recognized as an exothermic process while dissociation of molecules is considered as an endothermic process due to the formation and breakage of the chemical bonds.

To further verify the contribution of nitrogen adsorption from the vibrationally excited nitrogen molecules, I started to consider the kinetics of the nitrogen adsorption processes. Again look at Figure 3-3a that shows nitrogen plasma exposure time dependence of the XPS N1s peaks intensity on the Co(0001) surface. The Co(0001) is a well-defined surface which can give me an insight to conduct a quantitative analysis for the kinetics of the nitrogen adsorption process. First, the actual adsorption rate of nitrogen to the Co(0001) surface needed to be considered. It is hinted by the XPS N1s peak because the peak intensity of the XPS N1s is proportional to the amount of nitrogen on the Co(0001) surface as the following:

$$M_{N1s} = I_0 \sigma_{N1s} n_N$$

3 - 1

where M_{N1s} is the N1s peak intensity in the XPS measurement that related to the number of photoelectrons emitted from the sample surface, I_0 is the intensity of the irradiate X-ray, σ_{N1s} is the photoionization cross section of the 1s orbital of nitrogen (hereafter, the

values of ionization cross section area are relative to the ionization cross section area of C1s (22200 barn)), n_N is the number of nitrogen atoms within the irradiated area.

The above equation is based on the assumption that the nitrogen species adsorbed on the Co(0001) surface as a monolayer, the thickness caused attenuation of the photoelectrons from nitrogen was neglected. However, in the case of Co2p, the attenuation effect of the photoelectrons from the subsurface Co atoms must be considered. Follow the same manner, the Co2p peak can be present as:

$$M_{Co2p} = I_0 \sigma_{Co2p} n'_{Co}$$

3 - 2

$$n'_{Co} = n_{Co} \sum_{i=0} \exp\left(-\frac{d_i}{\lambda}\right)$$

3 - 3

where n'_{Co} is the equivalent number of Co atoms, n_{Co} is the number of outmost Co atoms on the Co(0001) surface, d_i is the depth of the i th Co layer, λ is the inelastic mean free path of the Co2p photoelectrons.

The crystal structure of the utilized Co single crystal is face centered cubic structure (FCC), and the distance between the two nearest Co layers is 2.017 Å. If we define the number density of the Co atom on the Co(0001) surface as 1 monolayer (ML) ($1.89 \times 10^{19} \text{ m}^{-2}$), then the amount of adsorbed nitrogen on the Co(0001) surface can be determined by the following calculations:

$$\frac{n_N}{n_{Co}} = \frac{I_{N1s} \sigma_{Co2p3/2} \left(\frac{1}{1 - \exp\left(-\frac{d_{Co}}{\lambda_{Co}}\right)} \right)}{I_{Co2p3/2} \sigma_{N1s}}$$

3 - 4

Specifically, $\sigma_{N1s} = 1.77$, $\sigma_{Co2p3/2} = 12.20$, $d_{Co} = 2.017 \text{ \AA}$, $\lambda_{Co} = 9.12 \text{ \AA}$ are used reference to the database [11-13]. The equation 3-4 can be reduced to:

$$\frac{n_N}{n_{Co}} = 34.74 \times \frac{I_{N1s}}{I_{Co2p3/2}}$$

3 - 5

Figure 3-4a shows the amount of adsorbed nitrogen as a function of the exposure time to nitrogen plasma. The adsorption rate can be then derived by taking the 1st deviation of the function as shown in Figure 3-4b.

Here I highlighted and focused on the nitrogen adsorption on the clean Co(0001) surface, i.e. the $t = 0$, where the interaction between the ready-to-adsorb nitrogen and adsorbed nitrogen can be neglected. The apparent initial adsorption rate, i.e., $s_{0,ap} \cdot I_{ap}$ would be $0.32 \text{ ML} \cdot \text{s}^{-1}$, which is $6.06 \times 10^{18} \text{ m}^{-2} \cdot \text{s}^{-1}$, read from the intercept in Figure 3-4b.

Second, the number of nitrogen molecules (or atoms) impinging on the Co(0001) surface from the plasma phase can be given by:

$$I = \frac{p}{\sqrt{2\pi m k_B T}}$$

3 - 6

which has been introduced in section 2.1. If we extract the density of the species n_d , which is a quantity can be directly measured by vacuum ultra-violet (VUV) spectroscopy, the equation can be reduced as the following:

$$I = \frac{Nk_B T}{V} \cdot \frac{1}{\sqrt{2\pi m k_B T}} = n_d \sqrt{\frac{k_B T}{2\pi m}}$$

3 - 7

The flux of nitrogen atoms under this condition (N_2 flow rate: 0.5 sccm, pressure in cell: 0.5 Pa, temperature: 298 K) can be then derived by putting the corresponding n_d of atomic nitrogen ($n_{d,N} = 2.00 \times 10^{16} \text{ m}^{-3}$, measured by Sasaki group, Laboratory of Plasma Processing for Environmental Technology, Hokkaido Univ.) into the equation as:

$$\begin{aligned} I_N &= n_{d,N} \sqrt{\frac{k_B T}{2\pi m_N}} = 2.00 \times 10^{16} \times \sqrt{\frac{1.38 \times 10^{-23} \times 298}{2\pi \times 2.33 \times 10^{-26}}} \\ &= 3.36 \times 10^{18} \text{ [m}^{-2} \cdot \text{s}^{-1}] \end{aligned}$$

3 - 8

The sticking coefficient s , which is defined as the ratio of the adsorption rate to the impingement rate, should be a certain value between unity and zero.

If we consider the atomic nitrogen is the only active species that can adsorb on the Co(0001) surface from the nitrogen plasma phase, the corresponding sticking coefficient to the clean surface (initial $\theta = 0$) would be:

$$s_{0,N} = \frac{s_{0,ap} \cdot I_{ap}}{I_N}$$

$$= \frac{6.06 \times 10^{18}}{3.36 \times 10^{18}} = 1.80$$

3 - 9

which is greater than unity.

There are two origins that may correspond to the result. The first one is the error in the measurement of the number density of atomic nitrogen in the plasma phase. Once the $n_{d,N}$ was underestimated, it would give a overestimated value in the sticking coefficient for atomic nitrogen. The second is that other type of excited species needs to be considered as the active species to the adsorption process on the Co(0001) surface, i.e., the vibrationally excited nitrogen molecules.

The flux of vibrationally excited nitrogen molecules under this condition (N_2 flow rate: 0.5 sccm, pressure in cell: 0.5 Pa, temperature: 298 K) can be derived by putting the corresponding n_d of atomic nitrogen ($n_{d,N_{2v}} = 3.80 \times 10^{18} \text{ m}^{-3}$, measured by Sasaki group, measured by Sasaki group, Laboratory of Plasma Processing for Environmental Technology, Hokkaido Univ) into the equation as:

$$I_{N_{2(v)}} = n_{d,N_{2(v)}} \sqrt{\frac{k_B T}{2\pi m_{N_2}}}$$

$$= 3.80 \times 10^{18} \times \sqrt{\frac{1.38 \times 10^{-23} \times 298}{2\pi \times 4.66 \times 10^{-26}}} = 4.50 \times 10^{20} \text{ [m}^{-2} \cdot \text{s}^{-1}\text{]}$$

3 - 10

Assuming the initial sticking coefficient of atomic nitrogen to be the unity, we can then estimate the initial sticking coefficient of vibrationally excited nitrogen molecule s_{0,N_2} to be:

$$s_{0,N_2(v)} = \frac{s_{0,ap} \cdot I_{ap} - s_{0,N} \cdot I_N}{I_{N_2(v)}}$$

$$= \frac{6.06 \times 10^{18} - 1 \times 3.36 \times 10^{18}}{4.50 \times 10^{20}} = 6 \times 10^{-3}$$

3 - 11

The initial sticking coefficient of vibrationally excited nitrogen molecule calculated in this way could be underestimated because the I take the maximum value for the initial sticking coefficient of atomic nitrogen. However, it is still 3 orders of magnitude greater than the dissociative sticking coefficient of nitrogen on the Fe(111) surface [14].

3.2 Hydrogenation of nitrogen species on Co(0001) surface

The nitrogen adsorbed Co(0001) surface was then exposed to pure H₂ gas (flow rate: 1.0 sccm, pressure: 0.6 Pa) for 600 s at room temperature, but there was no change in the XPS spectra after the exposure, indicating that the H₂ gas could not react with the adsorbed N on the Co surface at room temperature. Figure 3-5 shows the XPS N1s peak after exposure to H₂ plasma (flow rate: 1.0 sccm, pressure: 0.6 Pa, plasma power: 10 W) for 180 s. The amount of nitrogen on the Co surface decreases after exposure to H₂ plasma, which suggested the adsorbed nitrogen species can react with the active species generated by hydrogen plasma at room temperature. The peak splits into two peaks that should correspond to the formation of NH_x species [15]. For further investigation of the adsorbed

nitrogen exceed 1 ML, the Co(0001) surface with different amount of adsorbed nitrogen (greater and less than 1 ML) was then exposed to H₂ with different time periods. The relation of the corresponding normalized XPS N1s intensity and exposure time was shown in Figure 3-6. A clear difference in the decreasing rate of adsorbed nitrogen was observed to the two different initial states. It indicated that the non-uniform adsorption of nitrogen species was formed when the coverage of nitrogen exceeds monolayer.

3.3 Conclusions

I successfully observed nitrogen adsorption and its hydrogenation on Co surface with the assistance of ECR plasma by using a home-made cell and UHV system. Furthermore, I focused on the nitrogen adsorption / dissociation processes, which were generally recognized as the rate-determining step in most ammonia synthesis reaction conditions, on the Co(0001) model surface. Excited nitrogen molecules and atomic nitrogens were considered as the active candidates for the adsorption processes. Considering both the thermodynamic and kinetic analysis results of the nitrogen adsorption process, there may be species other than atomic nitrogen, i.e., vibrationally excited nitrogen molecules, in the plasma phase contributed to the nitrogen adsorption process on the Co surface. By assuming the initial sticking coefficient of atomic nitrogen as the unity, the underestimated sticking coefficient of vibrationally excited nitrogen molecules achieved 6×10^{-3} to the Co(0001) surface at room temperature. It indicates that plasma-assisted catalysis is a very potential pathway for ammonia synthesis under mild conditions.



Figure 3-1. (1×1) LEED pattern of Co(0001) clean surface, probe electron energy = 150 eV.

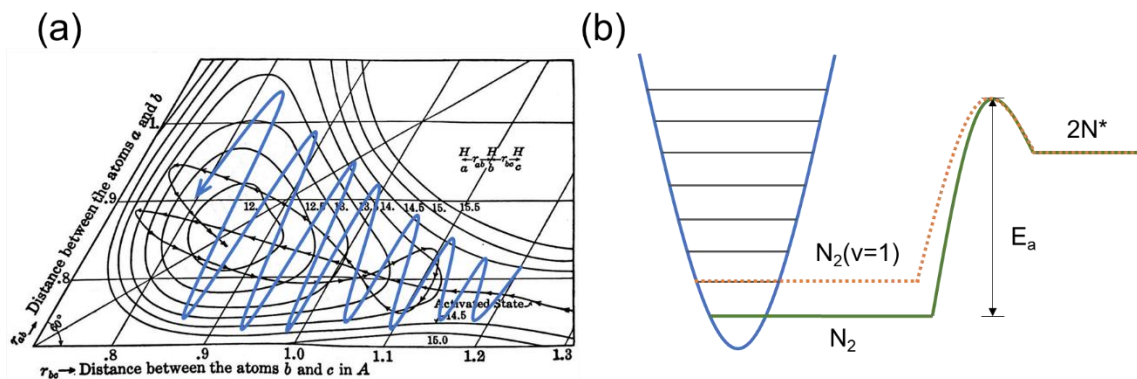


Figure 3-2. (a) An image of potential energy map of N-N (r_{ab}) and Co to N_2 (r_{bc}) distance and (b) schematic reaction coordinate comparing activation energies for N_2 dissociation from ground state (green solid line) and vibrationally excited state (orange dotted line).

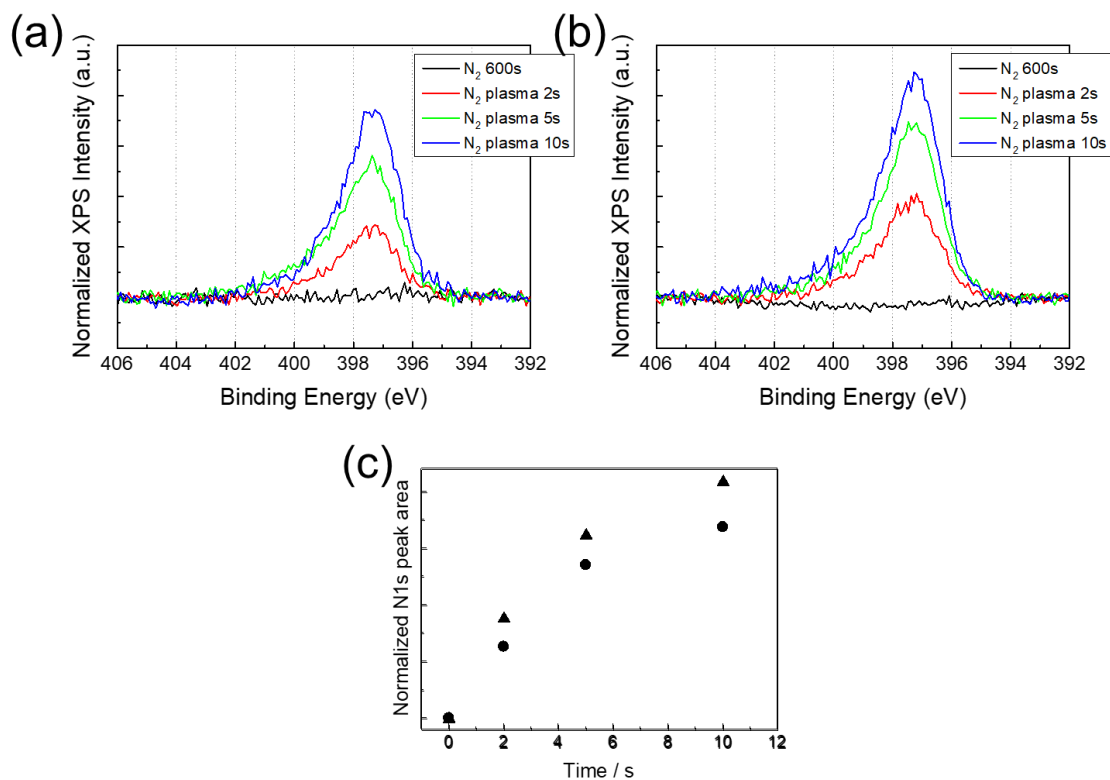


Figure 3-3. N 1s after exposure of nitrogen plasma at (a) 298 K and (b) 318 and the corresponding normalized N1s peak area (round for at 298 K and triangle for at 318 K).

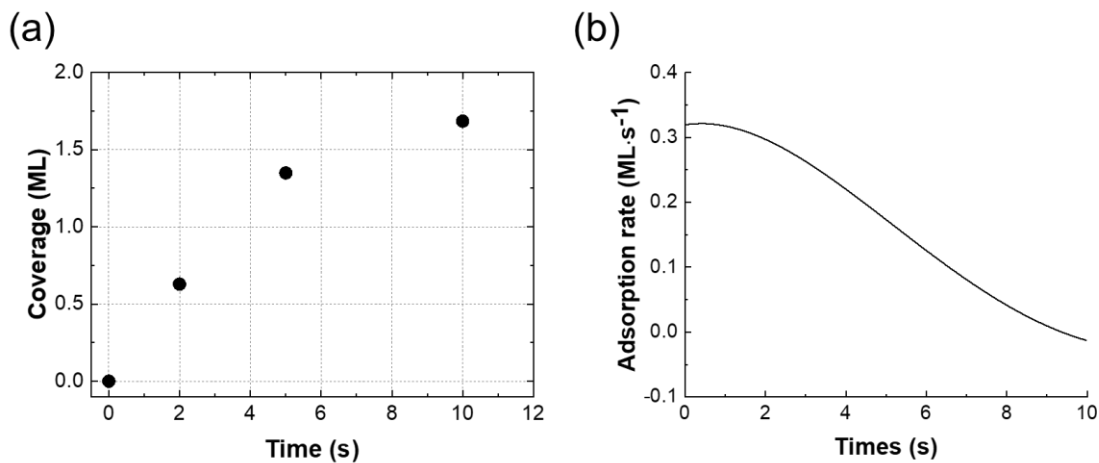


Figure 3-4. (a) Nitrogen coverage on Co(0001) surface as a function of nitrogen plasma exposure time and (b) the adsorption rate derived from the 1st deviation of the coverage.

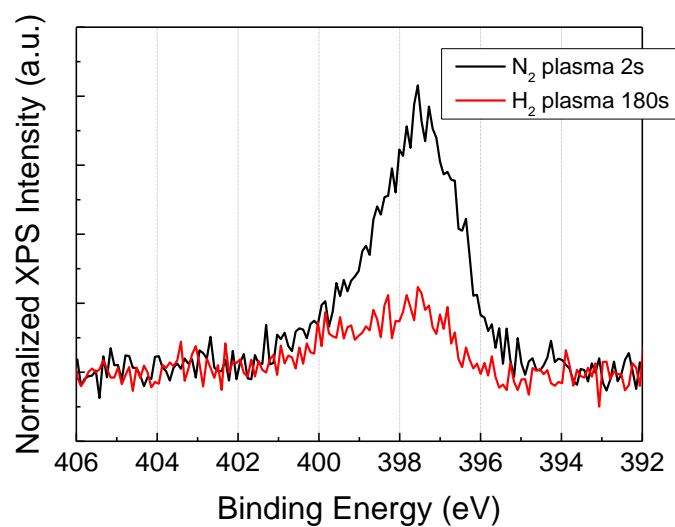


Figure 3-5. N 1s after exposure of hydrogen plasma at 298 K.

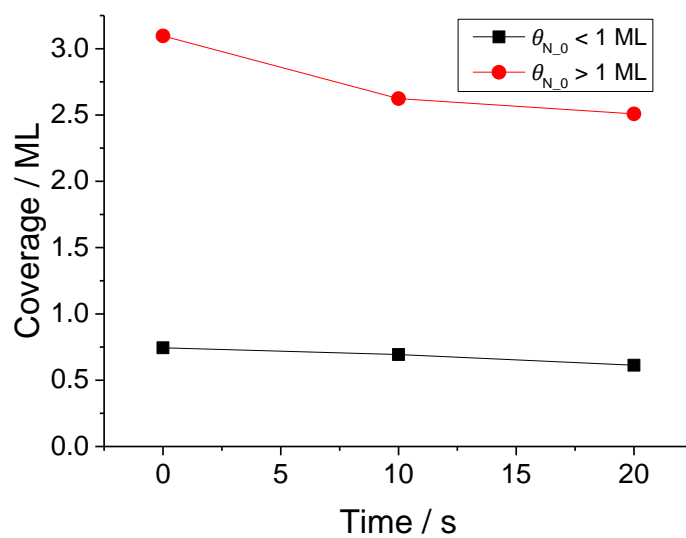


Figure 3-6. The amount of nitrogen species on the Co surface after exposure to hydrogen plasma of different initial coverages.

References

- [1] G. Ertl, “Elementary Steps in Ammonia Synthesis,” in *Catalytic Ammonia Synthesis: Fundamentals and Practice*, J. R. Jennings, Ed., in *Fundamental and Applied Catalysis*. Boston, MA: Springer US, 1991, pp. 109–132.
- [2] P. Mehta et al., “Overcoming ammonia synthesis scaling relations with plasma-enabled catalysis,” *Nat Catal*, vol. 1, no. 4, Art. no. 4, Apr. 2018.
- [3] E. C. Neyts, K. (Ken) Ostrikov, M. K. Sunkara, and A. Bogaerts, “Plasma Catalysis: Synergistic Effects at the Nanoscale,” *Chem. Rev.*, vol. 115, no. 24, pp. 13408–13446, Dec. 2015.
- [4] K. L. Mittal, “Surface Contamination: An Overview,” in *Surface Contamination: Genesis, Detection, and Control*, K. L. Mittal, Ed., Boston, MA: Springer US, 1979.
- [5] J. D. Donaldson and D. Beyersmann, “Cobalt and Cobalt Compounds,” in *Ullmann’s Encyclopedia of Industrial Chemistry*, John Wiley & Sons, Ltd, 2005.
- [6] B. W. Lee, R. Alsenz, A. Ignatiev, and M. A. Van Hove, “Surface structures of the two allotropic phases of cobalt,” *Phys. Rev. B*, vol. 17, no. 4, pp. 1510–1520, Feb. 1978.
- [7] M. Ehrensperger and J. Wintterlin, “*In situ* high-pressure high-temperature scanning tunneling microscopy of a Co(0001) Fischer–Tropsch model catalyst,” *Journal of Catalysis*, vol. 319, pp. 274–282, Nov. 2014.

- [8] C. J. Weststrate, P. van Helden, J. van de Loosdrecht, and J. W. Niemantsverdriet, “Elementary steps in Fischer–Tropsch synthesis: CO bond scission, CO oxidation and surface carbiding on Co(0001),” *Surface Science*, vol. 648, pp. 60–66, Jun. 2016.
- [9] H. Eyring, J. Walter, and G. E. Kimball, “Theory of Reaction Rates” in *Quantum Chemistry*, New York & London: Joh Wiley & Sons, Inc., 1944, pp. 299–331.
- [10] J. M. Thomas and W. J. Thomas, “Adsorption: Energetics, Isotherms and Rates” in *Introduction to the Principles of Heterogeneous Catalysis*, U.S. Ed., London & New York: Academic Press, 1967, pp. 14–63.
- [11] S. Tanuma, C. J. Powell, and D. R. Penn, “Calculations of electron inelastic mean free paths for 31 materials,” *Surface and Interface Analysis*, vol. 11, no. 11, pp. 577–589, 1988.
- [12] J. H. Scofield, “Hartree-Slater subshell photoionization cross-sections at 1254 and 1487 eV,” *Journal of Electron Spectroscopy and Related Phenomena*, vol. 8, no. 2, pp. 129–137, Jan. 1976.
- [13] J. J. Yeh and I. Lindau, “Atomic subshell photoionization cross sections and asymmetry parameters: $1 \leq Z \leq 103$,” *Atomic Data and Nuclear Data Tables*, vol. 32, no. 1, pp. 1–155, Jan. 1985.
- [14] S. Schwegmann et al., “The adsorption of atomic nitrogen on Ru(0001): geometry and energetics,” *Chemical Physics Letters*, vol. 264, no. 6, pp. 680–686, Jan. 1997.

- [15] A. Galtayries, E. Laksono, J.-M. Siffre, C. Argile, and P. Marcus, "XPS study of the adsorption of NH_3 on nickel oxide on Ni(111)," *Surface and Interface Analysis*, vol. 30, no. 1, pp. 140–144, 2000.

CHAPTER 4

3D STRUCTURE OF LOW COVERAGE Cu SPECIES ON α - $\text{Al}_2\text{O}_3(0001)$ SURFACE EXAMINED BY UHV PTRF-XAFS

Single atom catalysts (SACs), which usually consist of isolated single metal atoms dispersed on a powdery support (Figure 4-1) [1], have recently attracted much attention due to their high catalytic activity and cost-saving of noble metal atoms, compared with those of conventional nanoparticle catalysts [2-5]. For instance, single Pt atoms on an iron oxide support show high activity for CO oxidation reaction even at room temperature [5]. Since catalytic performance of the SACs significantly depends on coordination environment around the active metal site, i.e., metal-O bond distance, metal-O coordination number, coordination symmetry, and valence state of the metal atoms etc., unraveling the precise three-dimensional (3D) structure of the active metal site is essential to understand the structure-activity relationship and for development of further active SACs. However, it is difficult to determine their precise 3D structure from conventional XAFS when using a powdery oxide as a support, because bonding information is averaged over all directions and the support surface is generally ill-defined exposing various defects and crystal faces, which may often cause formation of non-uniform single metal species. On the other hand, when a well-defined single-crystal oxide surface is used as a support, information on precise 3D structure of uniform single metal species can be obtained by measuring the polarization-dependent XAFS of the metal species.

The 3D structure of atomic dispersed Cu on an α -Al₂O₃(0001) single-crystal surface was studied in the UHV conditions using the newly constructed compact PTRF-XAFS cell to test its performance on XAFS measurements.

4.1 Performance Test of the New Cell – Attaining PTRF-XAFS Spectra of a Low Coverage Model System

[Cu/ α -Al₂O₃(0001) model system]

An optically polished α -Al₂O₃(0001) single crystal (Shinkosha Co., Ltd.) with the edge length of 15 mm and the thickness of 0.5 mm was first treated at 1323 K for 3 h and followed by keeping at 873 K for 3 h in air to obtain an atomically flat α -Al₂O₃(0001) surface [6]. Monatomic step (0.2 nm) and terrace structures of greater than 300 nm width were confirmed on the entire surface using atomic force microscopy (AFM) as shown in Figure 4-2. The sample was then fixed to the sample holder and transferred into an ultra-high vacuum (UHV) chamber (the details of the sample holder and UHV chamber was introduced in Chapter 2) and heated at 673 K for > 1 h to degas. The surface showed a (1 × 1) pattern by low-energy electron diffraction (LEED) measurements as shown in Figure 4-3. There are two possible structures with different termination layers, i.e., oxygen terminated and aluminum terminated surfaces as shown in Figure 4-4. In this work, aluminum terminated surface structure was used according to the reported experimental [7, 8] and theoretical analysis results [9-11].

Cu was then deposited on the α -Al₂O₃(0001) surface by resistive heating of a Cu-wrapped tungsten wire (refer to Chapter 2) at room temperature in the sample preparation chamber. The vapor pressure was controlled to be lower than 1×10^{-5} Pa for the entire deposition process. The amount of deposited Cu on the α -Al₂O₃(0001) surface was

determined by the XPS measurement follow the same manner that introduced in Chapter 3. Submonolayer structure of Cu species was assumed so that the attenuation effect of the photoelectrons from alumina support by deposited Cu was neglected. Base on the surface structure of α -Al₂O₃(0001) as shown in Figure 4-5, the Cu coverage was estimated to be 0.19 ML from the XPS peak area ratio of Cu2p_{3/2} and Al2p as follows:

$$\frac{n_{Cu}}{n_{Al}} = \frac{I_{Cu2p3/2}\sigma_{Al2p} \left(\frac{1}{1 - \exp\left(-\frac{d_{Al2}}{\lambda_{Al_2O_3}}\right)} + \frac{\exp\left(-\frac{d_{Al1}}{\lambda_{Al_2O_3}}\right)}{1 - \exp\left(-\frac{d_{Al2}}{\lambda_{Al_2O_3}}\right)} \right)}{I_{Al2p}\sigma_{Cu2p3/2}}$$

Specifically, the photoionization cross section of aluminum 2p orbital $\sigma_{Al2p} = 0.54$, and of copper 2p_{3/2} orbital $\sigma_{Cu2p3/2} = 16.73$, the distance between the surface Al layer and the second Al layer of the α -Al₂O₃(0001) surface $d_{Al1} = 1.680$ Å, and between the surface Al layer and the third Al layer $d_{Al2} = 2.165$ Å, the inelastic mean free path of photoelectron in Al₂O₃ $\lambda_{Al_2O_3} = 28$ Å are used reference to the database [12-14]. 1 ML was defined as 5.1×10^{14} cm⁻² with correspondence to the density of surface Al atoms on the α -Al₂O₃(0001) substrate.

[UHV PTRF-XAFS measurements]

The Cu/ α -Al₂O₃(0001) sample was then transferred from the sample preparation chamber to the PTRF-XAFS cell through the sample parking chamber under the UHV condition. Then the cell was detached from the UHV chamber for the XAFS measurements. The detailed steps from sample installation to PTRF-XAFS measurement have been described in Chapter2. The vacuum environment inside the cell was kept by the non-evaporable

getter (NEG) during the transferring and by a turbo molecular pump and dry pump during the PTRF-XAFS measurements.

PTRF-XAFS measurements were conducted at the BL9A beamline of the Photon Factory at the Institute of Materials Structure Science (KEK-IMSS-PF, Tsukuba, Japan). The storage ring energy and ring current were 2.5 GeV and 450 mA, respectively. The major optical components are a bent conical collimation mirror (Rh coated Si, water-cooled for both side), a Si(111) double crystal monochromator, a bent conical focusing mirror (Rh coated ULE) and two flat mirrors for higher order reduction [15]. The beam size on the sample was regulated with a molybdenum pinhole with the diameter of 0.4 mm, which was attached before the ion chamber at upstream (I₀), to reduce undesirable irradiation outside of the sample surface (Figure 4-6).

The total reflection condition for s- polarization, where the electric field vector of X-ray paralleled the sample surface, was adjusted follow steps below:

- (1) Fix the *operando* PTRF-XAFS cell on the 6 - axis goniometer;
- (2) Make sure the sample ψ and ϕ are 0 and the sample surface is parallel to the optical stage;
- (3) Adjust sample X, Z so that the X-rays can go through the cell above the center of the sample and be detected by ion chamber located downstream of the sample (I₁). Now, the X-ray beam should be between the sample surface and the Be windows upper edges, otherwise it will be blocked by the sample holder or window edge leading to no X-ray detected in I₁;

- (4) Adjust sample Z to maximize I_1 detection (denoted as $I_{1\max}$) under the constraints of step (3);
- (5) Lift the sample surface by adjusting sample Z to make the sample partially block the X-ray beam so that I_1 value becomes half of $I_{1\max}$;
- (6) Adjust sample ϕ to find local maximum value (denoted as $I_{1\text{locmax}}$) in I_1 ;
- (7) Repeat step (5) and step (6) alternatively until $I_{1\text{locmax}} = \frac{1}{2} I_{1\max}$. Now, the sample surface is parallel to the X-ray propagation direction and blocks the lower half of the X-ray beam. Part of X-ray goes directly through the cell, while others are reflected by the sample surface with a grazing angle. The X-rays are, therefore, divided into two beams after encountering the sample surface.
- (8) Block the direct X-ray by a Pb piece in front of I_1 and optimize the sample surface position using sample Z and ϕ so that reflected X-ray achieve maximum in I_1 .

When it turns to p-polarization, where the X-ray electric field vector is perpendicular to the sample surface, the sample ψ in step (2) should be 90° and the adjustment of sample X and sample Z should be exchanged in step (4) and (5).

The Cu K fluorescence was detected by a 19-element pure Ge solid-state detector (SSDGL110S, Canberra, United States). The self-absorption effect can be neglected due to the ultra-low concentration ($4.9 \times 10^{14} \text{ cm}^{-2}$) of Cu species.

Then, the PTRF-XAFS spectra (Figure 4-7 and Figure 4-8) of the dispersed Cu species on the $\alpha\text{-Al}_2\text{O}_3(0001)$ surface under UHV condition were successfully obtained by using the newly designed and constructed cell.

4.2 3D Structure Determination of Cu Atoms on α -Al₂O₃(0001)

Figure 4-7a shows the PTRF-XANES spectra of the Cu species just after vacuum evaporation of Cu on an α -Al₂O₃(0001) surface and the XANES spectra of Cu foil, Cu₂O and CuO as the references (Figure 4-7b). The background removal and normalization processes were conducted using REX2000 following the procedures in section 2.4. The XANES spectra of the Cu/ α -Al₂O₃(0001) sample showed different features from that of Cu foil, which suggested the formation of non-metallic Cu species. The mid-edge features observed at approximately 8983 eV for s- and p-polarizations could be assigned to the 1s to 4p π^* transition, as determined from the previous XANES results [16]. The inflection points of the edge appeared at around 8980.4 eV for both polarization directions. Considering that the respective inflection points for references appeared at these points, the oxidation state of the Cu species is monovalent.

Cu was reported to have weaker strength of the metallic Cu-Cu interactions but stronger strength of the bonding as an oxidized species due to reduced cohesive energy and small ionic radius, respectively [17]. It means that Cu prefers to form single atom site than smaller clusters on the oxide surface when the coverage of Cu species is low. It is consistent with the EXAFS oscillations that I obtained in this measurement where the Cu-Cu interaction was not found. It indicates that the Cu species were atomically dispersed on the α -Al₂O₃(0001) surface at 0.19 ML. Figure 4-8 shows the EXAFS oscillations of the Cu/ α -Al₂O₃(0001) sample for s- and p-polarizations, respectively. The main oscillations damped quickly to noise level at the high-k region, which indicated that the presence of low Z elements in the nearest neighbor. It means that the interaction between the Cu species and the substrate and the structure of the substrate surface were the key

points to determining the local structure surrounding the Cu single atoms. The structure of the clean $\alpha\text{-Al}_2\text{O}_3(0001)$ surface has been studied by LEED, ion scattering and grazing incidence X-ray scattering [8, 18, 19]. It was demonstrated that $\alpha\text{-Al}_2\text{O}_3(0001)$ is terminated with an Al layer as shown in Figure 4-4b. This termination provides an auto compensated surface so that the exposed elements on the $\alpha\text{-Al}_2\text{O}_3(0001)$ surface are both oxygen and aluminum atoms, with which Cu could directly interact. Preliminary curve-fitting was conducted with the k-range from 30 nm^{-1} to 90 nm^{-1} and its Fourier transformed r-range from 0.116 nm to 0.227 nm . The number of available parameters (M) should therefore be equal to or less than 6 given by the equation as the following [20, 21]:

$$M = \frac{2\Delta k \cdot \Delta r}{\pi} + 2$$

If I assume the oxygen as the nearest neighbor atoms, the coordination number was 2.0 ± 0.5 and 2.9 ± 0.5 for s- and p-polarizations, respectively. The Cu-O distance to be $0.195 \pm 0.02\text{ nm}$ for both directions. The comparable goodness of fitting can be obtained when the nearest neighbor atom altered to aluminum with the coordination number of 1.2 ± 0.5 and 1.8 ± 0.5 for s- and p-polarizations, respectively, and Cu-Al distance of $0.220 \pm 0.02\text{ nm}$ and $0.216 \pm 0.02\text{ nm}$ for s- and p-polarizations, respectively. However, such short bond distance between Cu and Al has never been observed. The comparable coordination number in two polarizations suggested that no matter what the nearest neighbor atoms are, the location of Cu was not an atop site of substrate surface atoms which should give much less interactions in the s-polarization. Considering the coordination numbers, the candidate sites for Cu would be a two-oxygen bridge site and a three-fold oxygen hollow site. As shown in Figure 4-5, the bulk structure of the $\alpha\text{-Al}_2\text{O}_3$

consists of an alternated stacking of two Al planes and one O plane arranged with a three-fold symmetry. Each Al atom in this structure has three nearest neighbor oxygens at a distance of 0.185 nm and three second nearest neighbor oxygens at a distance of 0.197 nm. The Al in the (0001) surface has a terminal oxygen triangle with the O-O bond distance of 0.286 nm and sharing oxygen triangle with the O-O bond distance of 0.252 nm. Therefore, the (0001) surface of the α -Al₂O₃ has two types of oxygen bridge sites and three types of three-fold oxygen hollow sites. In this chapter, they are named as site-B1, site-B2, and site-H1, site-H2, site-H3, respectively. Site-B1 and site-B2 correspond to the bridge sites of oxygen atoms with longer (0.286 nm) and shorter (0.252 nm) O-O distances, respectively. Cu could be situated on the three-fold oxygen at site-H1 by removing a surface Al atom. There is no Al atom located at the second and third layer below. The site-H2 lies on the symmetric line of the large oxygen triangle with the O-O distance of 0.286 nm. The oxygen atoms have a nearest neighbor Al atom located at the second Al layer. When the Cu-O bond distance was set at 0.195nm, the distance between the Cu and second layer Al atom will be 0.187 nm, which is an unusual short bond distance for Cu and Al. The site-H3 is the three-fold site of the small oxygen triangle with the O-O distance of 0.252 nm. Further analysis including the Cu-O and Cu-Al interactions within 0.3 nm using FEFF [22] code and real-space model structures was carried out to determine the detailed local structure surrounding the Cu atoms. First, an ideal Al-terminated α -Al₂O₃(0001) surface was postulated as the initial structure. The atomic positions for it were shown on the left side of table 4-1. Cu atom was then put in the position of site-B1, site-B2, site-H1, site-H2 and site-H3 (Figure 4-9) at the Cu-O distance of 0.195 nm with minor variation of ± 0.02 nm. Figure 4-10 shows the simulated spectra

with the observed spectra in both polarizations. But no good agreement was found in any sites selected above, especially due to the strong Cu-Al interaction was involved.

I therefore turned to consider the surface structure of the α -Al₂O₃(0001) surface, it was reported that the X-ray diffraction indicated the relaxation of the α -Al₂O₃(0001) occurring under UHV condition [18]. The atomic positions of the relaxed surface were given on the right side of table 4-1. The relaxation involved several atomic layers beneath the surface. The first Al layer moved down towards the bulk so that the interplanar spacing with the nearest neighbor layer was reduced by 51%. The second layer (O) mainly shifted within the plane, moving almost radially towards the third layer (Al). It led to an O-O distance change so that the oxygen triangle around site-H2 had the O-O distance of 0.250 nm, while the oxygen triangle around site-H3 had the O-O distance of 0.277 nm. Following the same rule that the Cu-O bond distance was kept at 0.195 ± 0.02 nm, I put the Cu atom on the five sites (Figure 4-11) and simulated the EXAFS spectra according to them. Finally, site-B1 and site-H1 well reproduced the EXAFS oscillations for both polarizations as shown in Figure 4-12. Figure 4-11 shows the local structure of the two sites. It is difficult to deny either of them due to their comparable goodness of fitting to the observed spectra of both s- and p-polarizations. However, the site-H1 should correspond to the surface Al defects encountered with the Cu atoms from the Cu vapor. It should not be caused by the sputtering effect of Cu atom although the Cu atom is much heavier than the Al. Because unlike the accelerated Ar⁺ in the ion sputtering process, Cu atoms in the vapor basically undergo a free expansion process before arriving at the alumina surface. The Cu atoms therefore do not have sufficient kinetic energy to kick out the surface Al atoms. In this sense, the portion of the Cu atoms located at site-H1 should

be small due to the limited amount of Al detects on the α -Al₂O₃(0001) surface while nearly 0.2 ML Cu was deposited on the surface. Therefore, the majority of the deposited Cu species should be located at site-B1 and stabilized by two nearest neighbor oxygen and oxidized as Cu(I).

4.3 Conclusions

The newly constructed compact *operando* PTRF-XAFS cell was successfully applied to investigate the valence state and 3D structure of low coverage Cu species dispersed on a well-defined α -Al₂O₃(0001) surface under UHV condition. The valence state of the Cu species was determined to be monovalent according to the PTRF-XANES spectra. The Cu species was found to be atomically dispersed on the α -Al₂O₃(0001) surface at Cu coverage of 0.19 ML (9.7×10^{13} cm⁻²) due to the lack of Cu-Cu interaction from the PTRF-EXAFS spectra. Later, FEFF code [22] was applied to simulate the polarization dependent EXAFS in the two polarization directions. Five different sites including three-fold oxygen hollow sites and two oxygen bridge sites on the ideal (truncated bulk) and relaxed α -Al₂O₃(0001) surface were examined as the candidates according to the curve fitting results of the PTRF-EXAFS spectra. The Cu that was situated on the two-oxygen bridge site with O-O bond distance at 0.277 nm of the relaxed α -Al₂O₃(0001) surface showed best reproducibility to the experimental spectra in both polarizations. The Cu-O bond distance was 0.194 nm, which consistent well with the curve fitting results.

	Ideal surface			Relaxed surface		
	x	y	z	x	y	z
Al	0	0	1.148	0	0	1.122
O	0.361	0.333	1.083	0.352	0.372	1.09
O	0.667	0.027	1.083	0.628	-0.021	1.09
O	0.973	0.639	1.083	1.021	0.648	1.09
Al	0.333	0.667	1.019	0.333	0.667	1.015
Al	0.667	0.333	0.981	0.667	0.333	0.988
O	0.639	0.667	0.917	0.633	0.67	0.911
O	0.333	0.973	0.917	0.33	0.963	0.911
O	0.027	0.361	0.917	0.037	0.367	0.911
Al	0	0	0.852	0	0	0.849
Al	0.333	0.667	0.815	0.333	0.667	0.812
O	0.694	0	0.75	0.692	0.008	0.748
O	0	0.694	0.75	-0.008	0.684	0.748
O	0.306	0.306	0.75	0.316	0.308	0.748
Al	0.667	0.333	0.685	0.667	0.333	0.685
Al	0	0	0.648	0	0	0.647

Table 4-1. The atomic position of the ideal (left) and relaxed α -Al₂O₃(0001) surface [18]

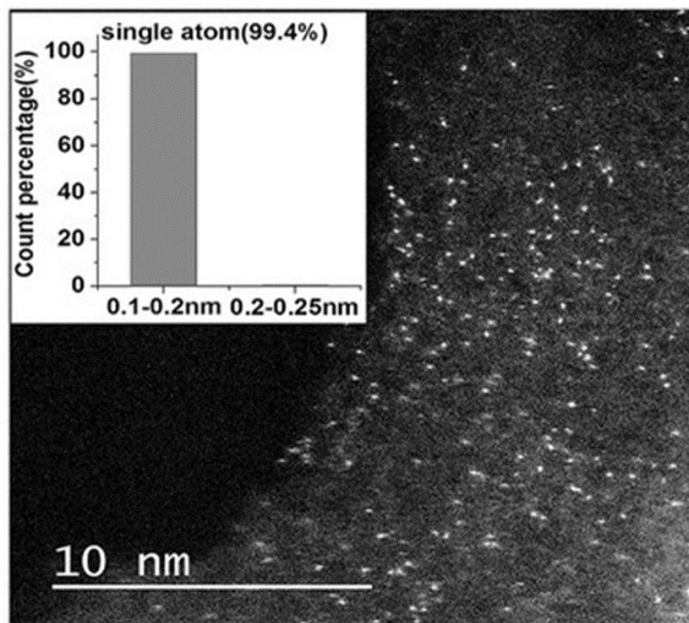


Figure 4-1. HAADF-STEM image of Pt single atoms on C₃N₄ with the inset of the size distribution of the bright spots [1].

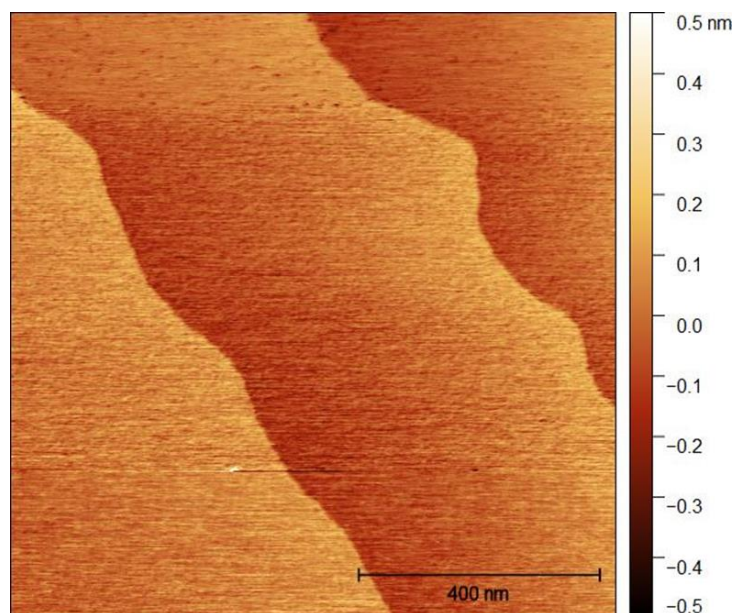


Figure 4-2. AFM image of clean α -Al₂O₃(0001) surface.

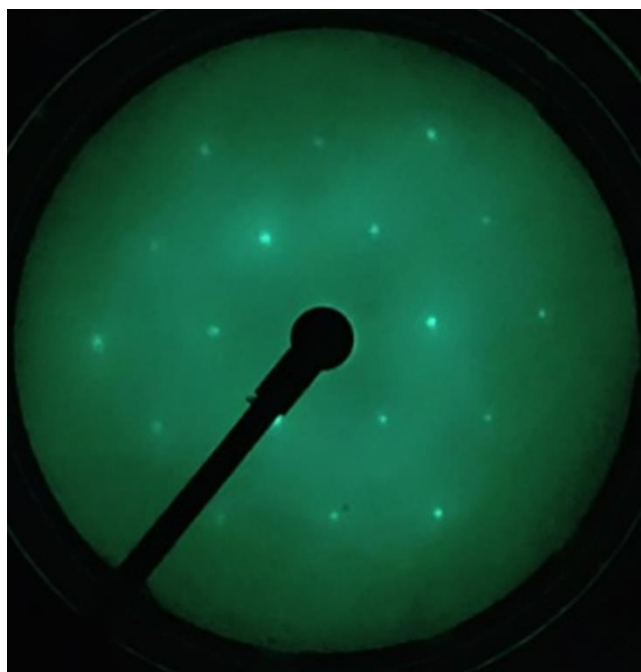


Figure 4-3. (1×1) LEED pattern of $\alpha\text{-Al}_2\text{O}_3(0001)$ clean surface, probe electron energy = 130 eV.

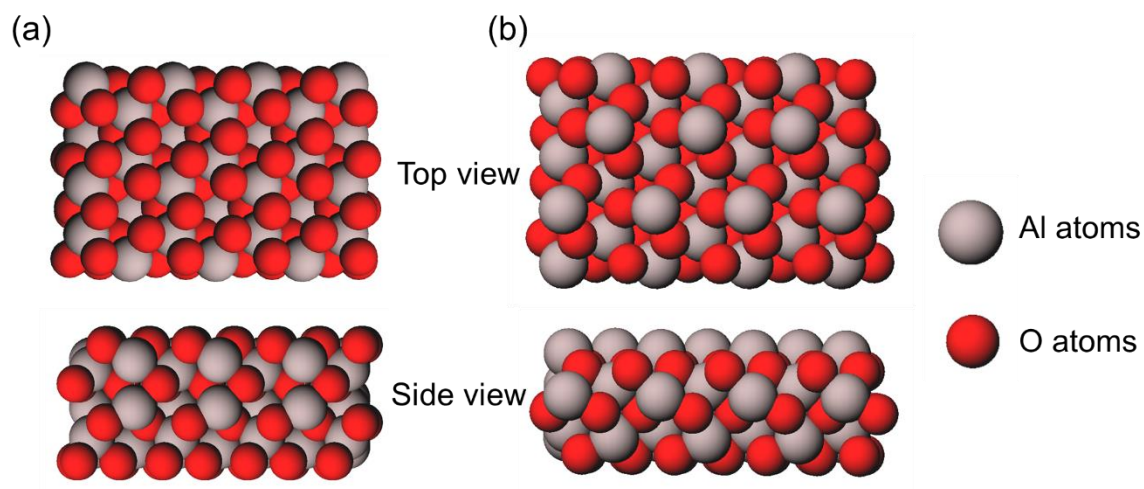


Figure 4-4. The ball model of $\alpha\text{-Al}_2\text{O}_3(0001)$. (a) Oxygen terminated and (b) aluminum terminated.

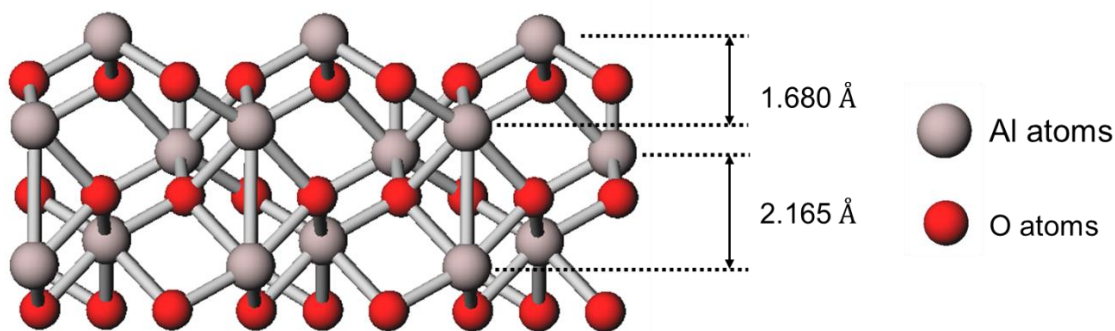


Figure 4-5. Side view of ball-and-stick model of Al terminated $\alpha\text{-Al}_2\text{O}_3(0001)$.

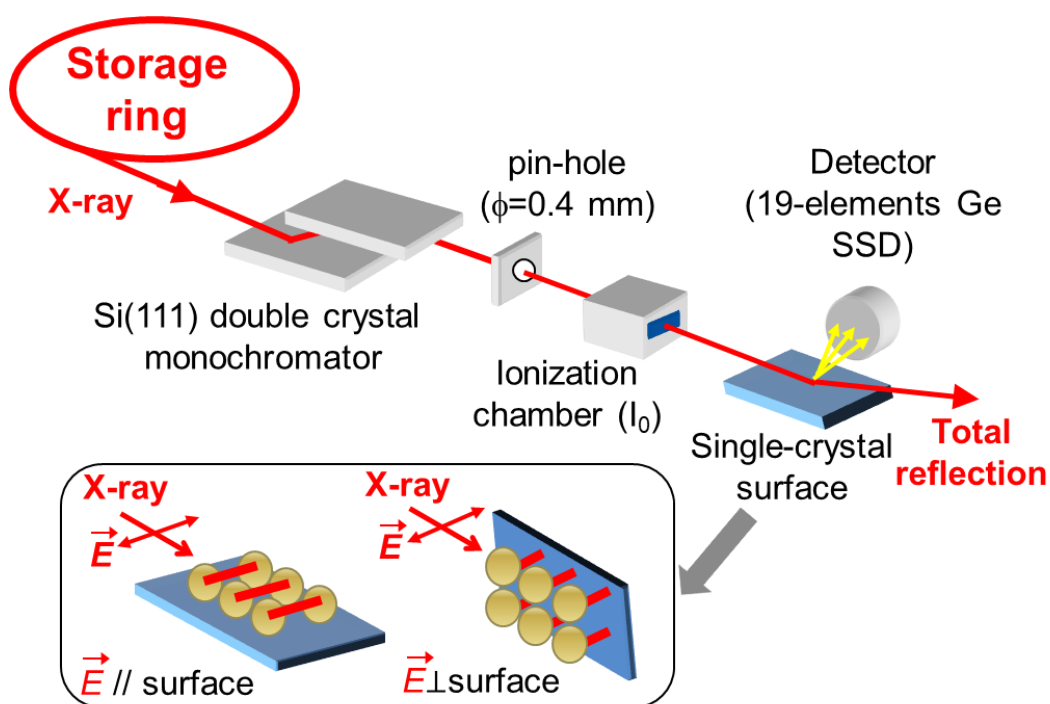


Figure 4-6. Schematic of the PTRF-XAFS technique. Polarization-dependent XAFS measurements of metal species dispersed on a single-crystal surface are conducted by combining total reflection and fluorescence detection modes using a multielement solid-state detector (SSD). Metal atoms on the single-crystal surface are shown as yellow balls.

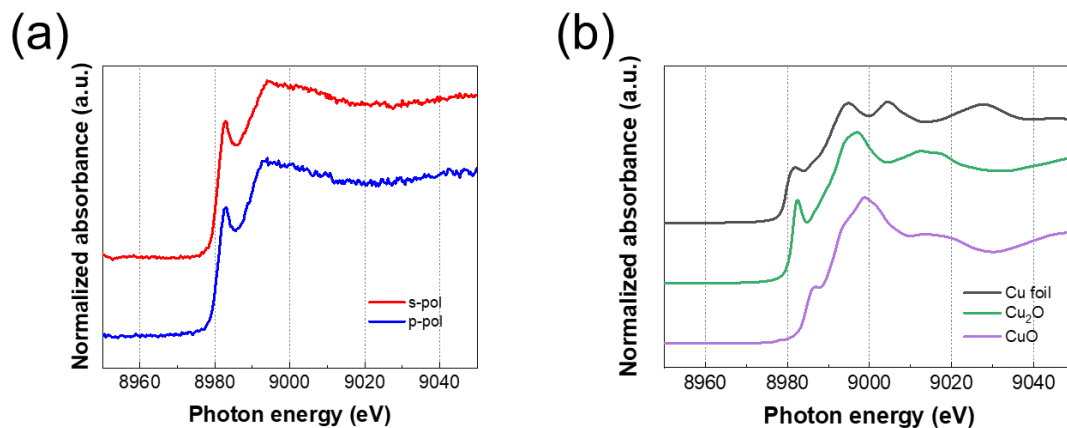


Figure 4-7. (a) Cu K-edge PTRF-XANES spectra of the Cu species on the α -Al₂O₃(0001) surface measured at room temperature under UHV condition. (b) Cu K-edge XANES spectra of Cu foil, Cu₂O and CuO as reference.

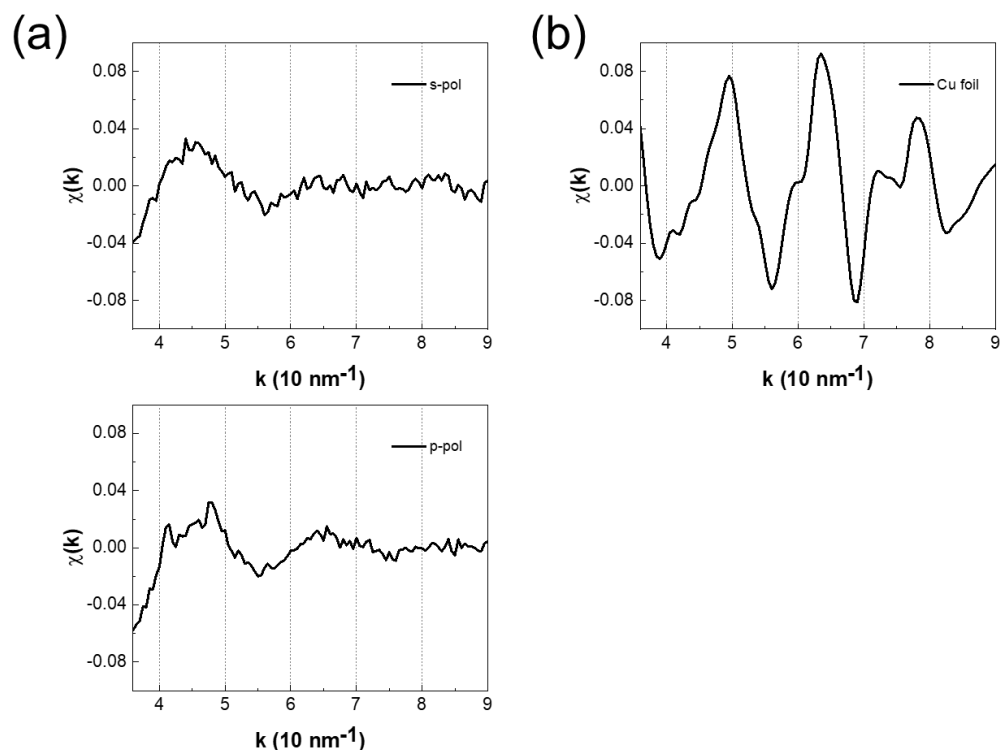


Figure 4-8. (a) Cu K-edge PTRF-EXAFS spectra of the Cu species on the α -Al₂O₃(0001) surface measured at room temperature under UHV condition. (b) Cu K-edge EXAFS spectra of Cu foil as a reference.

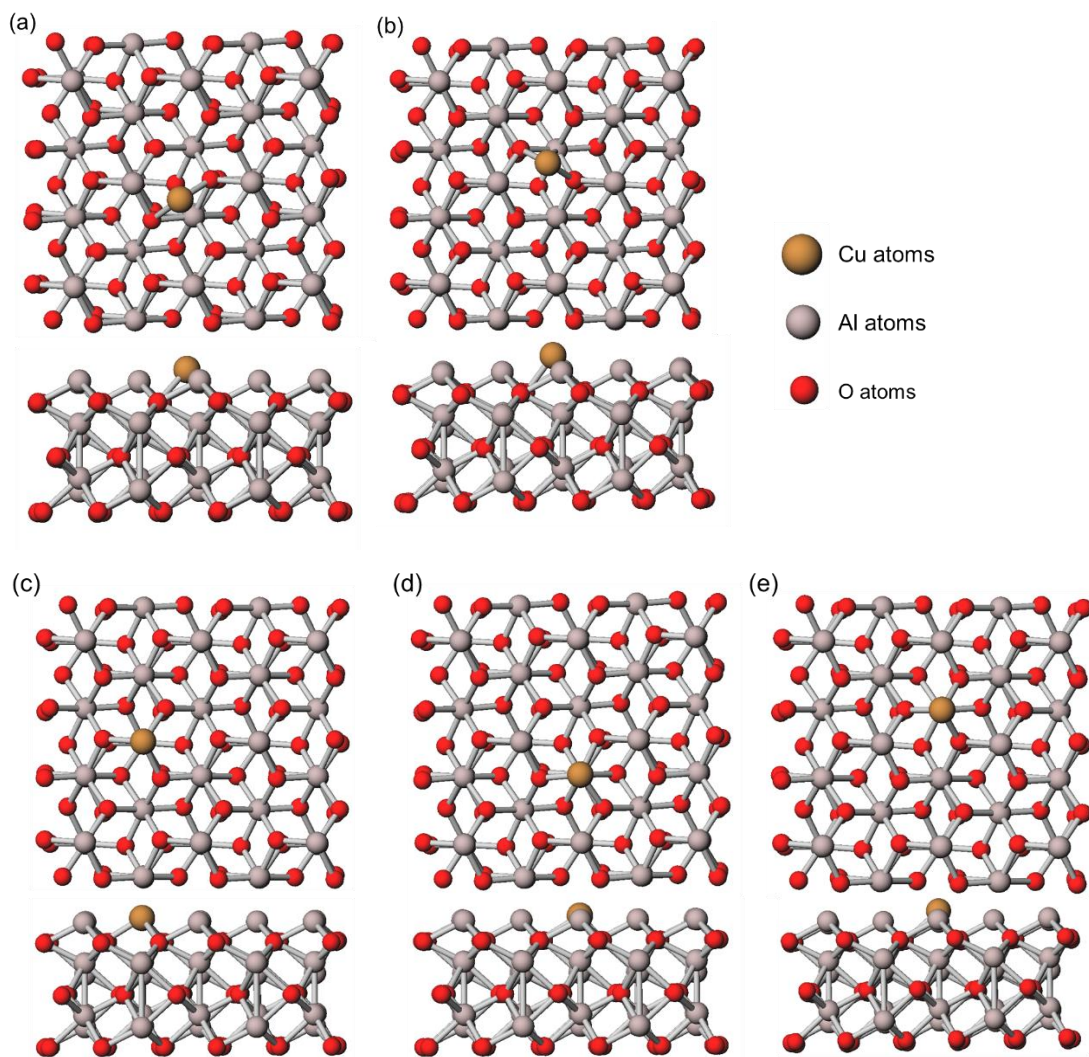


Figure 4-9. Local structures of Cu atom used for FEFF calculation to fit the PTRF-EXAFS spectra of the Cu species on the ideal α - $\text{Al}_2\text{O}_3(0001)$ surface under UHV condition. (a) site-B1, (b) site-B2, (c) site-H1, (d) site-H2, (e) site-H3.

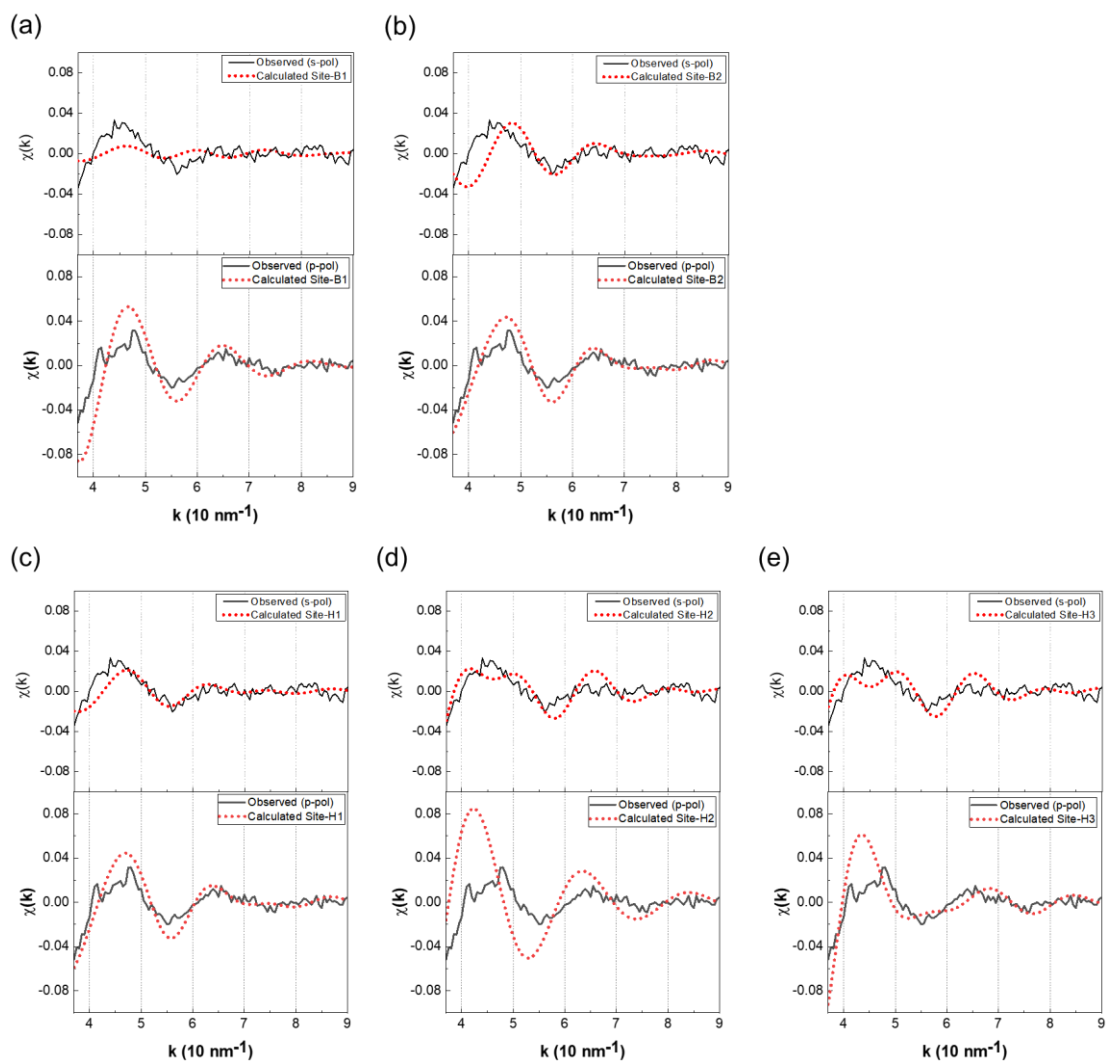


Figure 4-10. Series of calculated EXAFS oscillations for the Cu atom on the α - $\text{Al}_2\text{O}_3(0001)$ surface at sites shown in Figure 4-9. (a) site-B1, (b) site-B2, (c) site-H1, (d) site-H2, (e) site-H3.

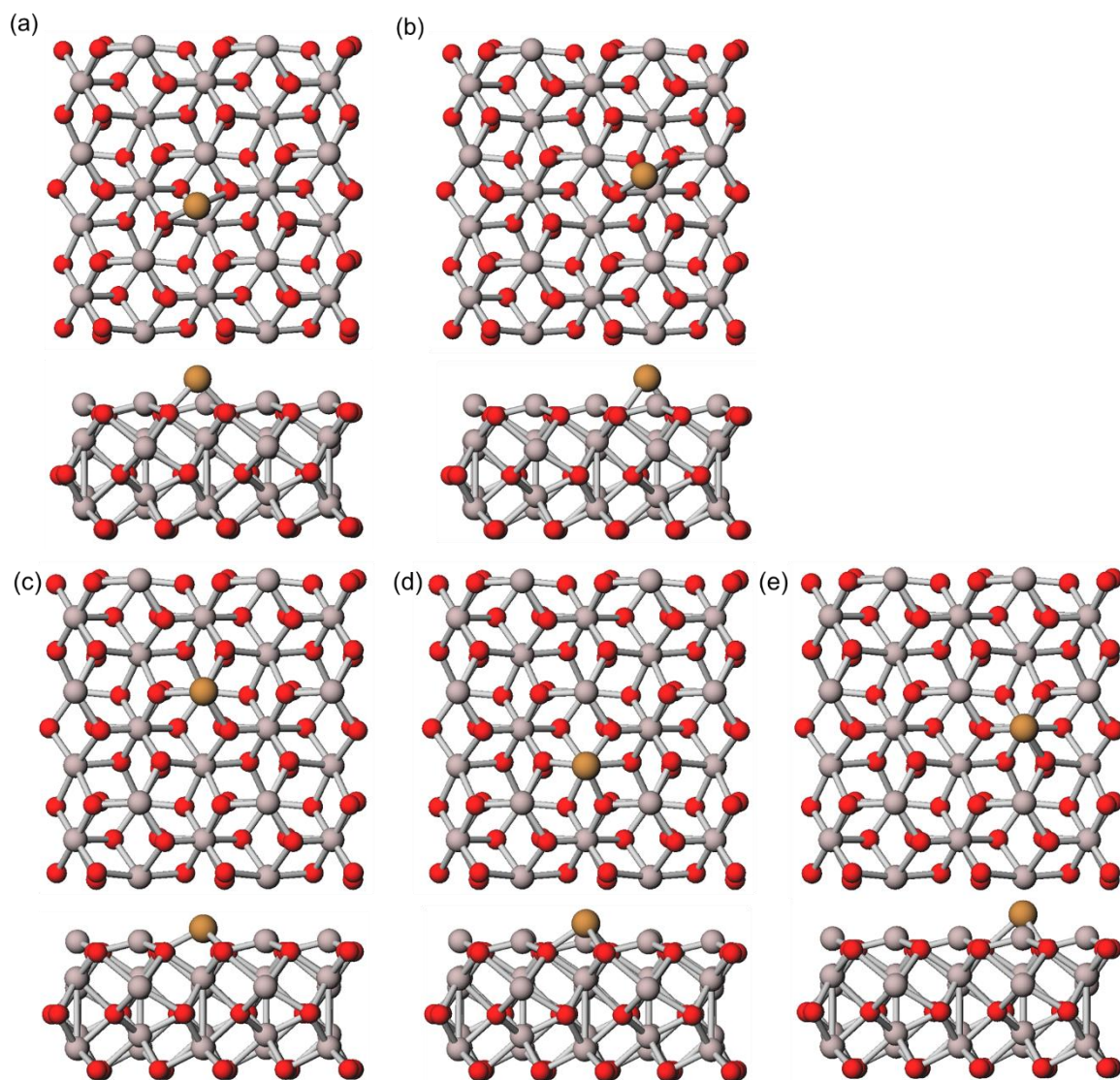


Figure 4-11. Local structures of Cu atom used for FEFF calculation to fit the PTRF-EXAFS spectra of the Cu species on the relaxed $\alpha\text{-Al}_2\text{O}_3(0001)$ surface under UHV condition. (a) site-B1, (b) site-B2, (c) site-H1, (d) site-H2, (e) site-H3.

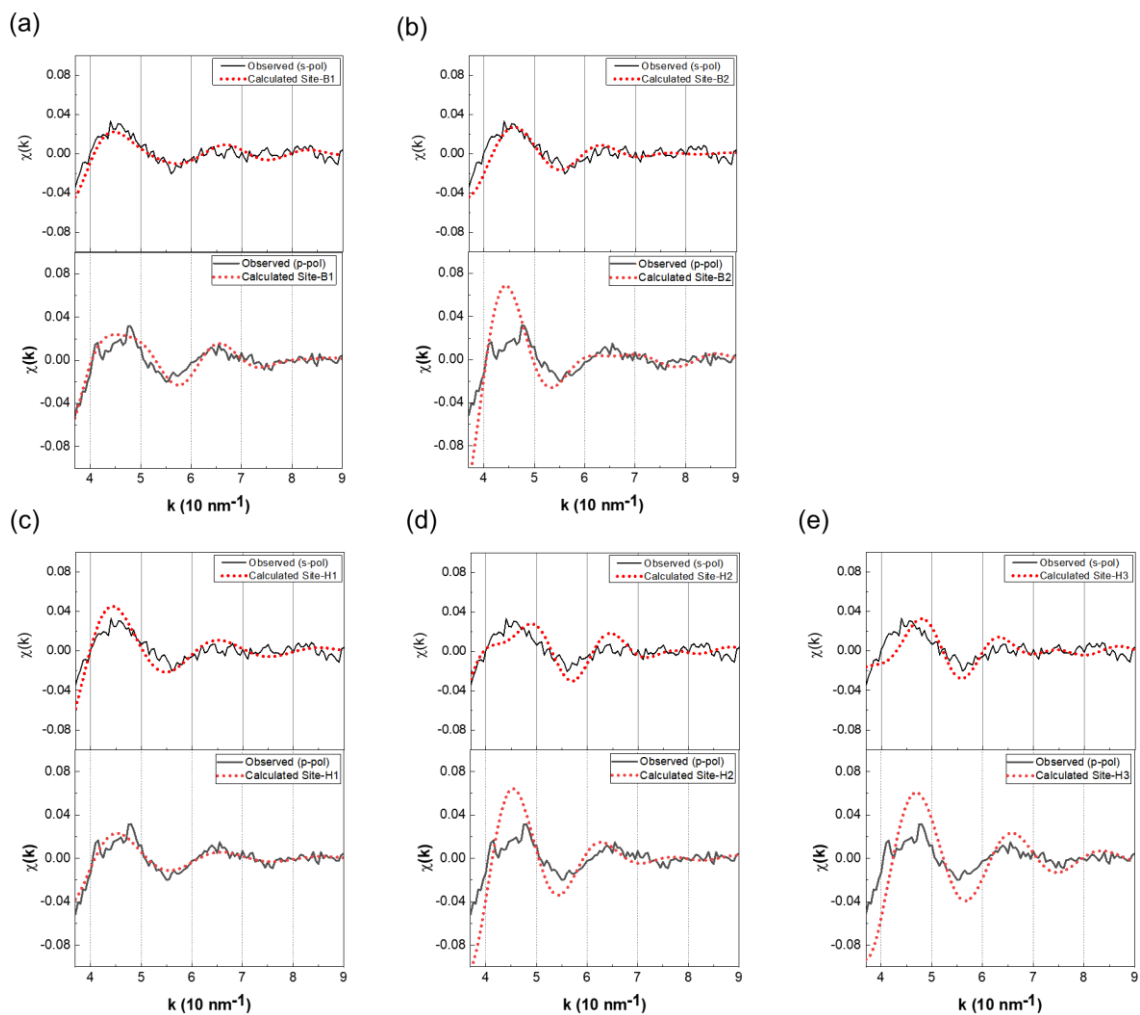


Figure 4-12. Series of calculated EXAFS oscillations for the Cu atom on the α - $\text{Al}_2\text{O}_3(0001)$ surface at sites shown in Figure 4-11. (a) site-B1, (b) site-B2, (c) site-H1, (d) site-H2, (e) site-H3.

References

- [1] X. Li et al., “Single-Atom Pt as Co-Catalyst for Enhanced Photocatalytic H₂ Evolution,” *Advanced Materials*, vol. 28, no. 12, pp. 2427–2431, 2016.
- [2] S. Liang, C. Hao, and Y. Shi, “The Power of Single-Atom Catalysis,” *ChemCatChem*, vol. 7, no. 17, pp. 2559–2567, 2015.
- [3] S. K. Kaiser, Z. Chen, D. Faust Akl, S. Mitchell, and J. Pérez-Ramírez, “Single-Atom Catalysts across the Periodic Table,” *Chem. Rev.*, vol. 120, no. 21, pp. 11703–11809, Nov. 2020.
- [4] R. Bliem et al., “Dual role of CO in the stability of sub-nano Pt clusters at the Fe₃O₄(001) surface,” *Proceedings of the National Academy of Sciences*, vol. 113, no. 32, pp. 8921–8926, Aug. 2016.
- [5] X.-F. Yang, A. Wang, B. Qiao, J. Li, J. Liu, and T. Zhang, “Single-Atom Catalysts: A New Frontier in Heterogeneous Catalysis,” *Acc. Chem. Res.*, vol. 46, no. 8, pp. 1740–1748, Aug. 2013.
- [6] T. Isono, T. Ikeda, R. Aoki, K. Yamazaki, and T. Ogino, “Structural- and chemical-phase-separation on single crystalline sapphire (0001) surfaces,” *Surface Science*, vol. 604, no. 21, pp. 2055–2063, Oct. 2010.
- [7] E. A. Soares, M. A. Van Hove, C. F. Walters, and K. F. McCarty, “Structure of the α -Al₂O₃(0001) surface from low-energy electron diffraction: Al termination and evidence for anomalously large thermal vibrations,” *Phys. Rev. B*, vol. 65, no. 19, p. 195405, Apr. 2002.

- [8] J. Ahn and J. W. Rabalais, "Composition and structure of the $\text{Al}_2\text{O}_3\{0001\}$ -(1×1) surface," *Surface Science*, vol. 388, no. 1, pp. 121–131, Oct. 1997.
- [9] C. Verdozzi, D. R. Jennison, P. A. Schultz, and M. P. Sears, "Sapphire (0001) Surface, Clean and with *d*-Metal Overlayers," *Phys. Rev. Lett.*, vol. 82, no. 4, pp. 799–802, Jan. 1999.
- [10] P. D. Tepesch and A. A. Quong, "First-Principles Calculations of α -Alumina (0001) Surfaces Energies with and without Hydrogen," in *Computer Simulation of Materials at Atomic Level*, John Wiley & Sons, Ltd, 2000, pp. 377–387.
- [11] X.-G. Wang, A. Chaka, and M. Scheffler, "Effect of the Environment on α - $\text{Al}_2\text{O}_3(0001)$ Surface Structures," *Phys. Rev. Lett.*, vol. 84, no. 16, pp. 3650–3653, Apr. 2000.
- [12] J. H. Scofield, "Hartree-Slater subshell photoionization cross-sections at 1254 and 1487 eV," *Journal of Electron Spectroscopy and Related Phenomena*, vol. 8, no. 2, pp. 129–137, Jan. 1976.
- [13] J. J. Yeh and I. Lindau, "Atomic subshell photoionization cross sections and asymmetry parameters: $1 \leq Z \leq 103$," *Atomic Data and Nuclear Data Tables*, vol. 32, no. 1, pp. 1–155, Jan. 1985.
- [14] S. Tanuma, C. J. Powell, and D. R. Penn, "Calculations of electron inelastic mean free paths for 31 materials," *Surface and Interface Analysis*, vol. 11, no. 11, pp. 577–589, 1988.

- [15] M. Nomura and A. Koyama, "Performance of a beamline with a pair of bent conical mirrors," *Nuclear Instruments and Methods in Physics Research Section A: Accelerators, Spectrometers, Detectors and Associated Equipment*, vol. 467–468, pp. 733–736, Jul. 2001.
- [16] N. Kosugi, H. Kondoh, H. Tajima, and H. Kuroda, "Cu K-edge XANES of $(\text{La}_{1-x}\text{Sr}_x)_2\text{CuO}_4$, $\text{YBa}_2\text{Cu}_3\text{O}_y$ and related Cu oxides. valence, structure and final-state effects on $1s-4p\pi$ and $1s-4p\sigma$ absorption," *Chemical Physics*, vol. 135, no. 1, pp. 149–160, Jul. 1989.
- [17] J. A. Kelber, C. Niu, K. Shepherd, D. R. Jennison, and A. Bogicevic, "Copper wetting of $\alpha\text{-Al}_2\text{O}_3(0001)$: theory and experiment," *Surface Science*, vol. 446, no. 1, pp. 76–88, Feb. 2000.
- [18] P. Guénard, G. Renaud, A. Barbier, and M. Gautier-Soyer, "Determination of the $\alpha\text{-Al}_2\text{O}_3(0001)$ Surface Relaxation and Termination by Measurements of Crystal Truncation Rods," *Surf. Rev. Lett.*, vol. 05, no. 01, pp. 321–324, Feb. 1998.
- [19] C. F. Walters, K. F. McCarty, E. A. Soares, and M. A. Van Hove, "The surface structure of $\alpha\text{-Al}_2\text{O}_3$ determined by low-energy electron diffraction: aluminum termination and evidence for anomalously large thermal vibrations," *Surface Science*, vol. 464, no. 2, pp. L732–L738, Oct. 2000.
- [20] E. A. Stern, "Number of relevant independent points in x-ray-absorption fine-structure spectra," *Phys. Rev. B*, vol. 48, no. 13, pp. 9825–9827, Oct. 1993.

- [21] P. A. Lee, P. H. Citrin, P. Eisenberger, and B. M. Kincaid, “Extended x-ray absorption fine structure -- its strengths and limitations as a structural tool,” *Rev. Mod. Phys.*, vol. 53, no. 4, pp. 769–806, Oct. 1981.
- [22] A. L. Ankudinov, B. Ravel, J. J. Rehr, and S. D. Conradson, “Real-space multiple-scattering calculation and interpretation of x-ray-absorption near-edge structure,” *Phys. Rev. B*, vol. 58, no. 12, pp. 7565–7576, Sep. 1998.

CHAPTER 5

STUDY OF A Pt/ α -Al₂O₃(0001) MODEL CATALYST DURING CO OXIDATION REACTION USING *in situ/operando* PTRF- XAFS TECHNIQUE

Oxide-supported noble metal nanoclusters have been used intensively for industrial catalytic processes. In particular, Pt nanoclusters dispersed on metal oxide supports showed outstanding performance on the catalysis of a variety of chemical reactions [1-3]. A consensus is that the catalytic performances of the oxide-supported metal catalysts largely depend on the size, shape of the metal species and their interaction with the supports, therefore, it is highly demanded to determine them at the atomic-level for elucidating precise structure-activity relationship. I have constructed a compact *operando* PTRF-XAFS cell that can reveal the 3D structure and electronic states of the dispersed metal species on oxide single-crystal surface. It has been applied to an atomically dispersed Cu/ α -Al₂O₃(0001) surface under UHV condition. However, the structure of the active species may change under the reaction conditions, which cannot occur under UHV.

In this chapter, the *operando* PTRF-XAFS technique was applied to a Pt/ α -Al₂O₃(0001) model catalyst surface during CO oxidation reaction for measurements at high temperatures in the presence of reactant gases while monitoring the catalytic activity using a quadrupole mass spectrometer (QMS).

*B. Lu, D. Kido, Y. Sato, H. Xu, WJ. Chun, K. Asakura and S. Takakusagi, J. Phys. Chem. C, vol. 125, no. 22, pp. 12424–12432, Jun. 2021. Reprinted with permission of publisher

5.1 3D structure of as-deposited Pt species on α -Al₂O₃(0001) surface at room temperature

An optically polished α -Al₂O₃(0001) single crystal (15 × 15 × 0.5 mm³, Shinkosha Co., Ltd.) was annealed in air at 1323 K for 3 h and followed by keeping at 873 K for 3 h to obtain an atomically flat α -Al₂O₃(0001) surface [4]. As shown in Figure 5-1, monatomic step and terrace structures were confirmed on the entire surface using atomic force microscopy (AFM). The sample was then transferred into an ultra-high vacuum (UHV) chamber and heated at 573 K for > 1 h to degas. The surface showed a (1 × 1) pattern by low-energy electron diffraction (LEED) measurements (Figure 5-2). Pt was deposited by Pt vapor generation through electron bombardment of a Pt rod (99.98%, Nilaco Co., Japan) with application of a high voltage (typically 850 V) between the filament and the Pt rod. XPS measurement was performed after Pt deposition to estimate the coverage of the Pt species. Pt 4f and Al 2p peaks were generally measured for quantitative analysis. However, here I used the ratio of Pt 4d_{3/2} and Al 2s XPS peak intensities to calculate the Pt coverage, because the Pt 4f electron and Al 2p electron have similar binding energy so that their XPS peaks overlapped with each other, which made the analysis difficult. The calculated process followed the same routine used in section 4.1 with the parameters of $\sigma_{Al2s} = 0.75$, $\sigma_{Pt4d3/2} = 7.78$, $d_{Al1} = 1.680 \text{ \AA}$, $d_{Al2} = 2.165 \text{ \AA}$, $\lambda_{Al_2O_3} = 28 \text{ \AA}$ from the database [5-7]. The Pt coverage was estimated to be 0.96 monolayer (ML) where 1 ML was defined as $5.1 \times 10^{14} / \text{cm}^2$ with correspondence to the density of surface Al atoms on the α -Al₂O₃(0001) substrate.

The Pt/ α -Al₂O₃(0001) sample was then transferred to the *operando* PTRF-XAFS cell under the UHV condition, and the cell was detached from the UHV chamber for the XAFS measurements (see Figure 2-8 for details).

PTRF-XAFS measurements were conducted at the BL9A beamline [8] of the Photon Factory at the Institute of Materials Structure Science (KEK-IMSS-PF, Tsukuba, Japan). The storage ring energy and ring current were 2.5 GeV and 450 mA, respectively. X-rays were monochromatized with a Si(111) double-crystal monochromator that was focused by using a pair of bent conical mirrors, and the beam size on the sample was regulated with a pinhole (0.4 mm diameter) to reduce undesirable irradiation (Figure 33 in Chapter 4). The total reflection conditions were adjusted using a 6-axis goniometer (see Figure 2-10 in Chapter 2). PTRF-XAFS measurements were conducted with two different orientations against the electric vector (E) of the incident X-rays, i.e., parallel to the surface (s-polarization) and perpendicular to the surface (p-polarization). The Pt L α fluorescence was detected using a 19-element Ge solid state detector (SSDGL0110S, Canberra, United States).

EXAFS analysis was performed using REX 2000 (Rigaku Co., Japan) package [9]. The EXAFS oscillations were extracted using a spline smoothing method and normalized with respect to the edge height with the energy dependence expressed in a Victoreen equation. The 3D structure was determined by an iterative method using the FEFF8.04 [10] code with a Hedin-Lundqvist potential based on a real-space model structure. The Debye–Waller factor of Pt–Pt was fixed to one value for each polarization direction, respectively. The goodness of fit between the observed ($\chi_{obs}(k)$) and calculated ($\chi_{cal}(k)$) XAFS oscillations was evaluated based on a χ square test using:

$$R^2 = \frac{1}{N} \sum_k \frac{\{\chi_{obs}(k) - \chi_{cal}(k)\}^2}{\{\varepsilon(k)\}^2}$$

6 - 1

where N and $\varepsilon(k)$ are the number of data points and the error of the observed spectrum, respectively. The calculated XAFS oscillations were adopted as a good model structure when R^2 values were lower than unity. To avoid confusion between the EXAFS oscillation ($\chi(k)$) and χ -squared test, R^2 was used instead of χ^2 .

After preparation of the Pt/ α -Al₂O₃(0001) surface in the UHV sample preparation chamber, the sample was transferred to the *operando* PTRF-XAFS cell. The cell was then detached and transferred to the hutch in the beamline. The sample in the cell was kept in argon atmosphere (100 Pa) during the transfer to the hutch, and the PTRF-XAFS measurements were conducted in the argon environment after attaching the cell to the goniometer and optimizing the total reflection conditions for the incident X-rays.

Figure 5-3a shows PTRF-EXAFS spectra of the as-deposited Pt species on the α -Al₂O₃(0001) surface measured at room temperature, together with a spectrum of Pt foil as a reference (Figure 5-3b). In Figure 5-1a, little polarization dependence was observed between the two polarization directions. The amplitude of the EXAFS oscillations was smaller than that of the Pt foil, and the spectra were each a simple sinusoidal shape, which indicates a smaller coordination number and the absence of higher-coordination shells because of the formation of small Pt clusters. In addition, the EXAFS oscillations were dumped quickly, which suggests that the small Pt clusters may have large disorder. Preliminary curve-fitting results showed that the first-shell Pt–Pt bond distance was 0.269

± 0.002 nm and the effective coordination numbers for the two polarization directions were 4 ± 1 . These results suggested that the Pt clusters have high symmetry as with cuboctahedral or icosahedral structures. Similar Pt–Pt bond distance (0.268 nm) and coordination number (5.0) were obtained for the 2.6% Pt/Al₂O₃ powder catalyst [11].

Bonding interactions between the Pt clusters and the α -Al₂O₃(0001) substrate, i.e., Pt-O and Pt-Al interactions, could not be detected in the curve-fitting analysis, probably because of the spherical shape of the Pt clusters, which would result in less interaction with the Al₂O₃ support surface.

An iterative method using the FEFF code [10] and a real-space model structure were employed to determine the detailed morphology of the Pt clusters. From a geometrical consideration of the Pt clusters based on the EXAFS results and previous reports [12-14], we assumed cuboctahedral (O_h) and icosahedral (I_h) structures that have a spherical shape and energetic stability (closed shell) at the magic number of 13, 55, and 147 clusters (Figure 5-4). A significant difference in the O_h and I_h models is that the O_h clusters have both (111) and (100) faces, whereas the I_h clusters have only the (111) face. Another difference is that the I_h clusters have two different bond lengths, whereas the O_h clusters have just one. Figure 5-5 shows a series of calculated EXAFS oscillations based on the Pt₁₃, Pt₅₅, and Pt₁₄₇ clusters. The I_h-Pt₅₅ cluster structure best reproduced the observed EXAFS spectra (Figure 5-6) with $R^2 < 1$ for the two polarization directions (Table 1). Although there should be a size distribution, it was concluded that the majority of the Pt clusters were I_h-Pt₅₅ (1.0 nm), which corresponds well to the previous report that I_h-Pt₅₅ is energetically more stable than O_h-Pt₅₅ [15]. The orientation of the I_h-Pt₅₅ cluster

could not be determined, because it had a symmetric shape and gave no significant polarization dependence, in principle.

Table 1. R^2 values for EXAFS oscillation fits with Pt cluster models for the Pt species on α -Al₂O₃(0001) at room temperature.

Symmetry	Number of Pt atoms	R^2 (s-pol)	R^2 (p-pol)
Cuboctahedron (O _h)	13	1.70	1.74
	55	2.81	2.71
	147	4.15	4.37
Icosahedron (I _h)	13	1.29	1.41
	55	0.98	0.95
	147	1.13	1.14

R_2 tests were carried out in the k-ranges of 35 ~ 100 nm⁻¹.

5.2 Simultaneous measurements of catalytic activity and XANES

Catalytic activity for CO oxidation reaction and PTRF-XANES of the Pt/ α -Al₂O₃(0001) surface were measured simultaneously, and the relationship between the activity and valence state of the Pt species was monitored when the sample is heated in the reactant gases. Figure 5-7 shows the results of sampling and analysis of the gases in the cell by QMS when the sample is heated in a stepwise manner, i.e., room temperature (RT) → 353 K → 393 K → 433 K → 473 K as a function of time after introducing the mixture gases (CO+O₂+Ar, Ar is an internal standard) into the cell. The ratio of the gases was CO : O₂ : Ar = 20%:72%:8% and total pressure was 250 Pa. CO₂ production along with CO and O₂

consumption was successfully confirmed at > 433 K and catalytic activity at 473 K was estimated to be 5×10^{-4} mol/(g_{Pt}·s) using the *operando* PTRF-XAFS system. It is noted that the product detection depends on catalytic activity itself and measurement time (accumulation time) since the cell adopts a batch-type reactor, which means that longer measurement time has a chance to detect the product even at a lower reaction temperature.

Figure 5-8 shows the PTRF-XANES spectra measured during the heating process in the reactant gases indicated in Figure 5-7. The peak in the spectra which is called “white line” started to decrease at ~ 353 K in both polarizations when the reaction temperature was increased and this observation is clearly confirmed by plotting the white line intensity as a function of the temperature. The white line intensity reflects the density of unoccupied states of Pt 5d orbitals since the L₃ absorption edge corresponds to an electron transition from the 2p_{3/2} to unoccupied 5d orbitals in the Pt atom, thus reflecting the oxidation state of Pt atom. Therefore Figure 5-6 suggested that the Pt atoms on the α -Al₂O₃(0001) surface were gradually reduced with increase of the temperature. I speculate that the reduction was primarily caused by partial desorption of CO pre-adsorbed on the Pt cluster surfaces at room temperature in the reactant gases because it is reported that thermal desorption of CO started at 350~400 K when the CO-covered Pt nanoparticles (~ 1.7 nm) on α -Al₂O₃(0001) or Pt clusters (Pt₇, Pt₁₅, Pt₂₀) on Al₂O₃/NiAl(110) were heated in the UHV conditions [16]. Another possibility for the decrease in the white line intensity in Figure 5-5 is thermal aggregation of the Pt clusters since the ratio of the CO-adsorbed Pt atoms to the total Pt atoms should be decreased by the aggregation. Such aggregation behavior was observed when the Pt/ α -Al₂O₃(0001) surface was heated at 493 K in the reactant gases which will be described in the next

session, however, its contribution might be small since increase in the cluster size was not significant.

5.3 3D structure of the Pt species on α -Al₂O₃(0001) surface during CO oxidation

I also succeeded in measuring PTRF-EXAFS spectra of the Pt species on the α -Al₂O₃(0001) surface during CO reaction at 493 K in the reactant gases (Figure 5-7) and evaluated the relationships between 3D structure and catalytic activity of the Pt species. The spectra in Figure 5-9 did not show a significant polarization dependence, which suggested that the Pt species is spherical in shape. Preliminary curve-fitting results indicated the first-shell Pt–Pt bond distance at 0.273 ± 0.002 nm, while the effective coordination numbers were 8 ± 1 in the two polarization directions. These values were similar to those (Pt–Pt bond distance, 0.273 nm; coordination number, 7.1) reported for the 1.2% Pt/SiO₂ powder catalyst [11]. FEFF simulation was conducted to determine the 3D structure of the Pt species based on a strategy similar to that described in section 5.1. Cuboctahedral (O_h) and icosahedral (I_h) structures were again assumed, and the 55, 147, and 309 clusters were tested (Figure 5-10). A series of calculated EXAFS oscillations based on the Pt₅₅, Pt₁₄₇, and Pt₃₀₉ clusters is illustrated in Figure 5-11. The O_h-Pt₁₄₇ cluster structure best reproduced the observed EXAFS spectra (Figure 5-12), and only this cluster structure provided $R^2 < 1$ for the two polarization directions (Table 2). It was thus concluded that the I_h-Pt₅₅ clusters (Figure 5-6b) were converted to O_h-Pt₁₄₇ clusters (1.6 nm) when the Pt/ α -Al₂O₃(0001) surface was heated at 493 K in the reactant gases. It should be noted that the O_h-Pt₁₄₇ cluster structure is the averaged one with a certain size/shape distribution. The catalytic activity at 493 K was also monitored during the EXAFS measurements, and the turnover frequency (TOF) per surface Pt atom was

estimated to be 0.06 s^{-1} , assuming the number of the exposed surface Pt atoms as 92 in the $\text{O}_h\text{-Pt}_{147}$ cluster. The *operando* PTRF-XAFS system thus enabled evaluation of the relationship between the 3D structure and catalytic activity of the Pt species dispersed on $\alpha\text{-Al}_2\text{O}_3(0001)$.

Previous reports suggested that icosahedral clusters could be the most favorable structures at small sizes because the surface was composed of only the most stable (111) closed-packed facets [14]. However, this stabilization of the icosahedral structure is achieved at the expense of volume instability (strain in the cluster) because the interatomic distances are not ideal, i.e., intershell bonds are compressed while intrashell bonds are expanded. When the cluster size is increased and the volume instability exceeds the surface effect, a structural crossover to ideal fcc structures such as the cuboctahedron is expected to occur to reduce the strain in the cluster. The crossover size (N, number of Pt atoms) from the icosahedral to fcc Pt cluster has been reported to be $N < 100$ [17]. According to the present results, $\text{I}_h\text{-Pt}_{55}$ clusters are formed initially on the $\alpha\text{-Al}_2\text{O}_3(0001)$ surface at room temperature and are then converted to the $\text{O}_h\text{-Pt}_{147}$ structure when the sample is heated at 493 K in the reactant gases, which is in agreement with previous results [14, 17].

Table 2. R^2 values for EXAFS oscillation fits with Pt cluster models for the Pt species on $\text{Al}_2\text{O}_3(0001)$ at 493 K in the reactant gases ($\text{CO}:\text{O}_2:\text{Ar}=20\%:72\%:8\%$, 100 Pa).^a

Symmetry	Number of Pt atoms	R^2 (s-pol)	R^2 (p-pol)
(O_h)	55	1.03	1.02
	147	0.98	0.94

	309	1.12	1.07
Icosahedron (I_h)	55	1.40	1.35
	147	1.22	1.15
	309	1.18	1.09

R^2 tests were carried out in the k-ranges of 35-100 nm⁻¹.

5.4 Conclusions

The *operando* PTRF-XAFS technique has been successfully developed to determine the valence state and 3D structure of active metal species dispersed on a well-defined single-crystal surface during catalytic reactions under realistic gas pressure conditions. I applied this technique to the Pt/ α -Al₂O₃(0001) surface during CO oxidation. Icosahedral Pt₅₅ clusters were initially formed on the Pt/ α -Al₂O₃(0001) surface at room temperature. The catalytic activity of the Pt/ α -Al₂O₃(0001) surface for the CO oxidation reaction was followed with simultaneous monitoring of the valence state and 3D structure of the Pt clusters. The Pt clusters were converted to the cuboctahedral Pt₁₄₇ structure under CO oxidation reaction at 493 K. The TOF per surface Pt atom at 493 K was estimated to be 0.06 s⁻¹, based on the Pt cluster structure. Thus, *operando* PTRF-XAFS technique can give information on precise relationship between the 3D structure and catalytic activity of supported metal species in heterogeneous catalysis, which is difficult to obtain when using powdery samples or by other surface science techniques. Because the 3D structure–activity relationship is important information to reveal the origins of the catalytic activity, the *operando* PTRFXAFS technique will make a significant

contribution to atomic level understanding of heterogeneous catalysis and further development of active supported metal catalysts.

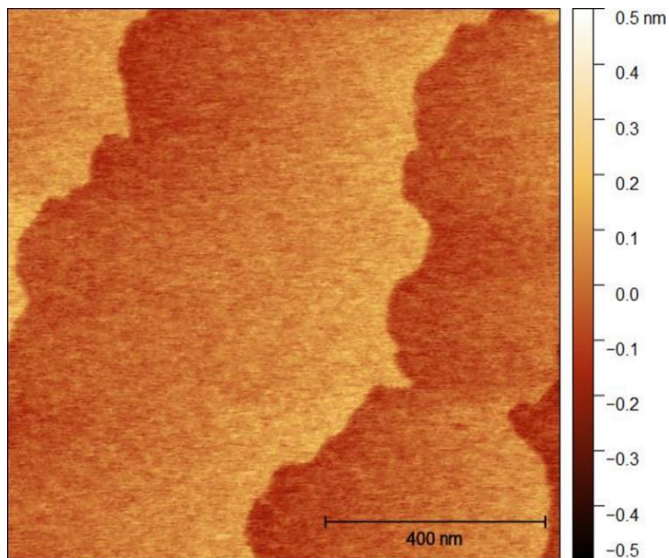


Figure 5-1. AFM image of clean $\alpha\text{-Al}_2\text{O}_3(0001)$ surface.

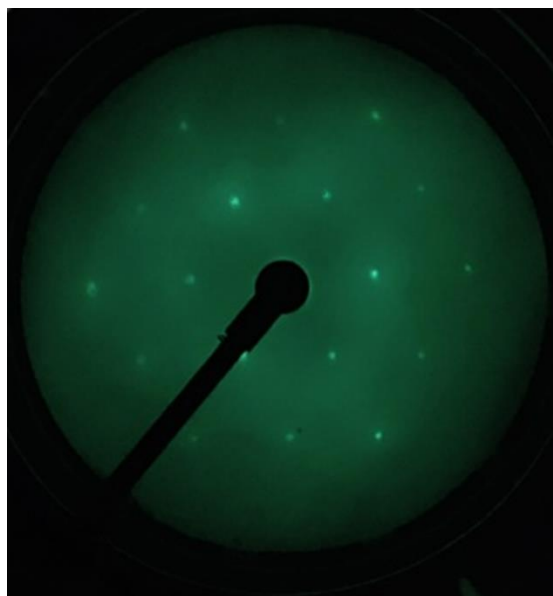


Figure 5-2. (1×1) LEED pattern of $\alpha\text{-Al}_2\text{O}_3(0001)$ clean surface, probe electron energy = 130 eV.

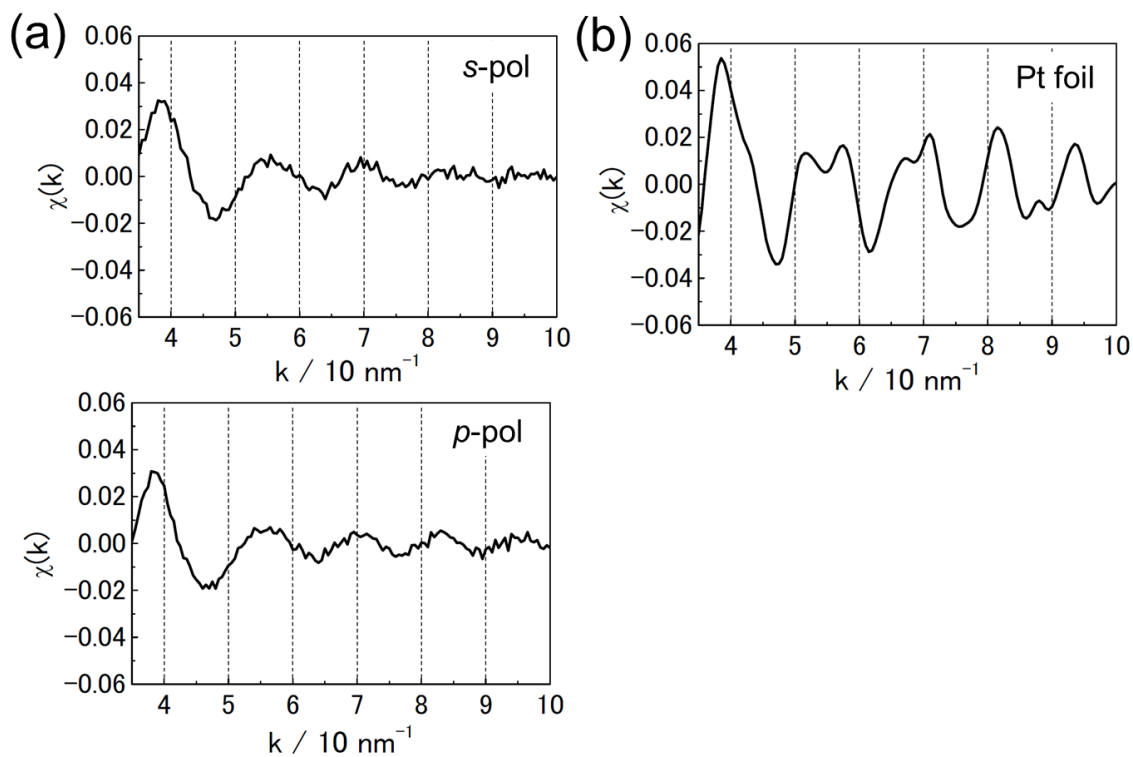


Figure 5-3. (a) Pt L₃-edge PTRF-EXAFS spectra of the Pt species on the α -Al₂O₃(0001) surface measured at room temperature in an inert atmosphere (100 Pa Ar). The k -range was limited to 100 nm^{-1} because of the low coverage of the Pt atoms (0.96 ML). (b) Pt L₃-edge EXAFS spectra of Pt foil as a reference.

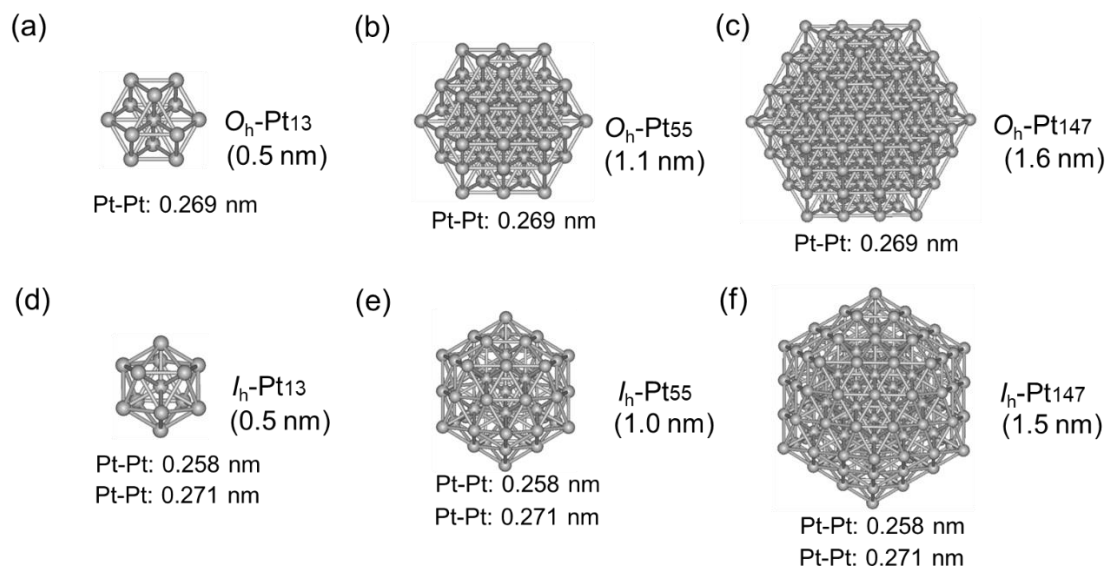


Figure 5-4. Structures of Pt clusters used for FEFF calculation to fit the PTRF-EXAFS spectra of the Pt species on the α -Al₂O₃(0001) surface at room temperature. (a) O_h -Pt₁₃, (b) O_h -Pt₅₅, (c) O_h -Pt₁₄₇, (d) I_h -Pt₁₃, (e) I_h -Pt₅₅, (f) I_h -Pt₁₄₇. Cluster size and Pt-Pt bond distances are also illustrated. In the I_h -cluster structures, the shorter Pt-Pt bond corresponds to intershell bonds while the longer one to intrashell bonds.

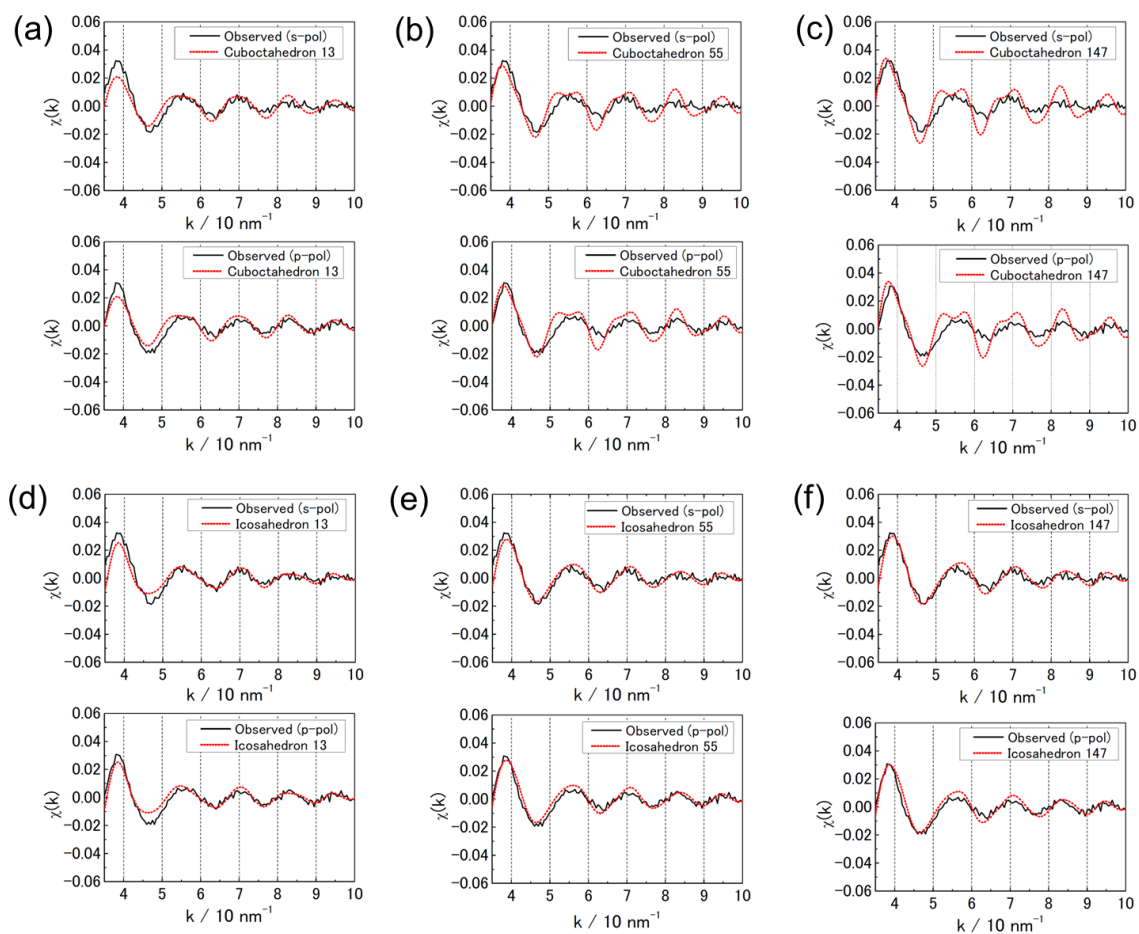


Figure 5-5. Series of calculated EXAFS oscillations (red dotted lines) for the Pt species on the $\alpha\text{-Al}_2\text{O}_3(0001)$ surface at room temperature using the Pt cluster structures shown in Figure 5-2. (a) $\text{O}_h\text{-Pt13}$, (b) $\text{O}_h\text{-Pt55}$, (c) $\text{O}_h\text{-Pt147}$, (d) $\text{I}_h\text{-Pt13}$, (e) $\text{I}_h\text{-Pt55}$, (f) $\text{I}_h\text{-Pt147}$

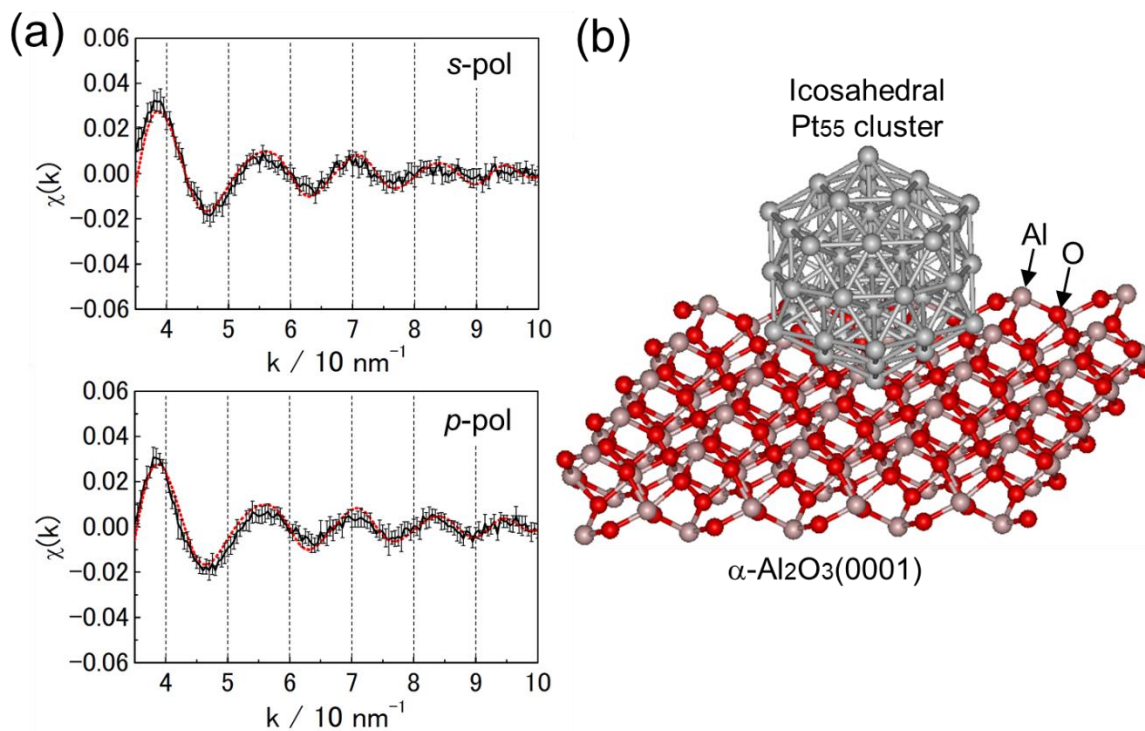


Figure 5-6. (a) Observed (black solid line) and calculated (red dotted line) EXAFS spectra for the Pt species on the $\alpha\text{-Al}_2\text{O}_3(0001)$ surface at room temperature. Errors of the observed spectra are also shown. The $I_h\text{-Pt}_{55}$ cluster model illustrated in panel b was assumed for the calculation, and the $\alpha\text{-Al}_2\text{O}_3(0001)$ support was not included in the calculation. The Pt–Pt bond distances are 0.258 and 0.271 nm for intershell and intrashell bonds, respectively.

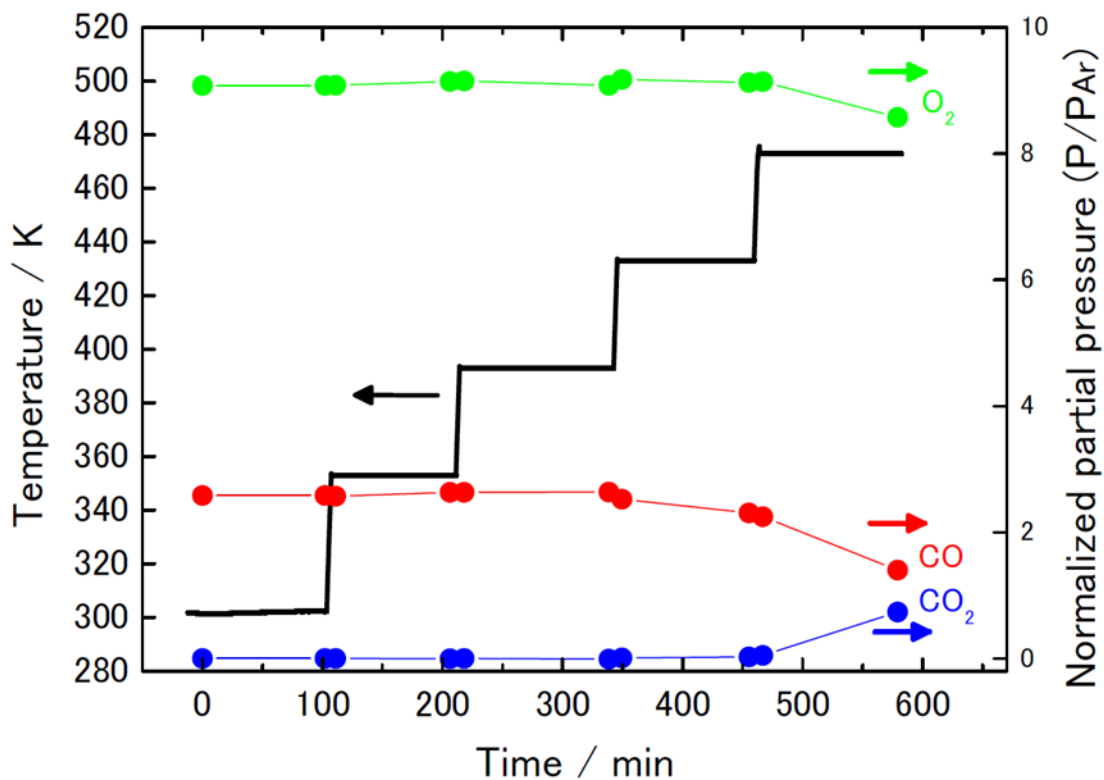


Figure 5-7. CO oxidation activity measurements for the Pt/ α -Al₂O₃(0001) surface using the *operando* PTRF-XAFS cell. After the reactant gases (CO:O₂:Ar = 20%:72%:8%, total pressure 250 Pa) were introduced into the cell at room temperature, the Pt/ α -Al₂O₃(0001) surface was heated at 353, 393, 433, and 473 K, and the reaction was monitored using the QMS. Ar was used as an internal standard gas.

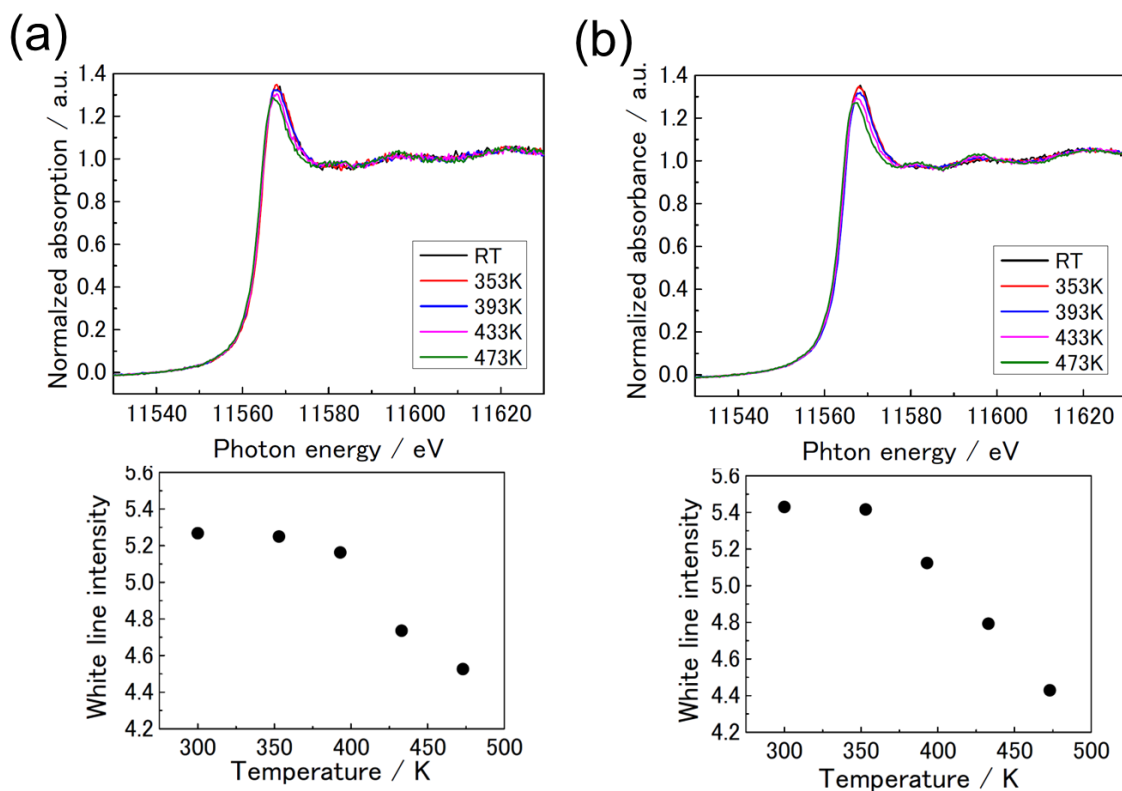


Figure 5-8. Pt L_3 -edge PTRF-XANES spectra of the Pt/ $Al_2O_3(0001)$ surface obtained at room temperature, 353K, 393K, 433 K and 473K during the CO oxidation activity measurement in Figure 5-5, and the plots of white line intensity as a function of temperature. (a) s-polarization. (b) p-polarization. The white line intensity was evaluated by a curve fitting analysis using a set of a Lorentzian and an arctangent function.

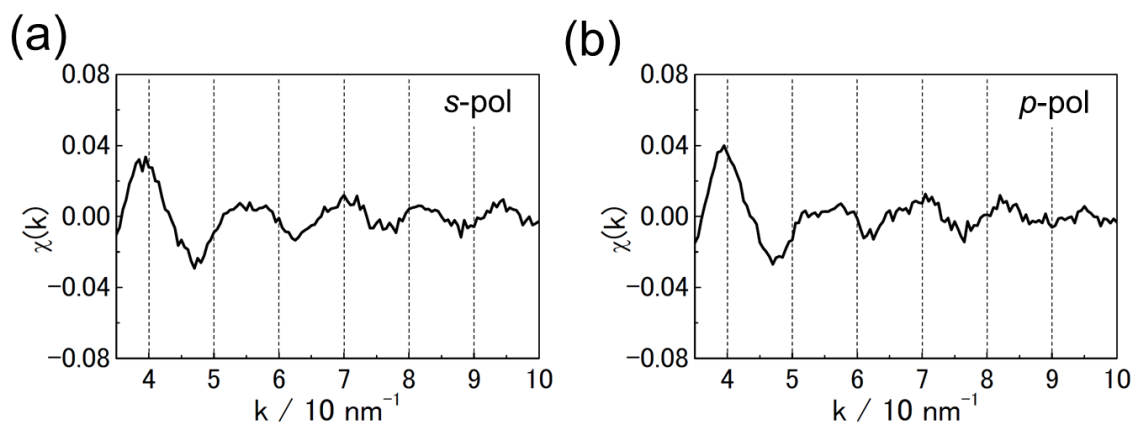


Figure 5-9. Pt L₃-edge PTRF-EXAFS spectra of the Pt species on the α -Al₂O₃(0001) surface measured at 493 K in the reactant gases (CO:O₂:Ar = 20%:72%:8%, total pressure 100 Pa).

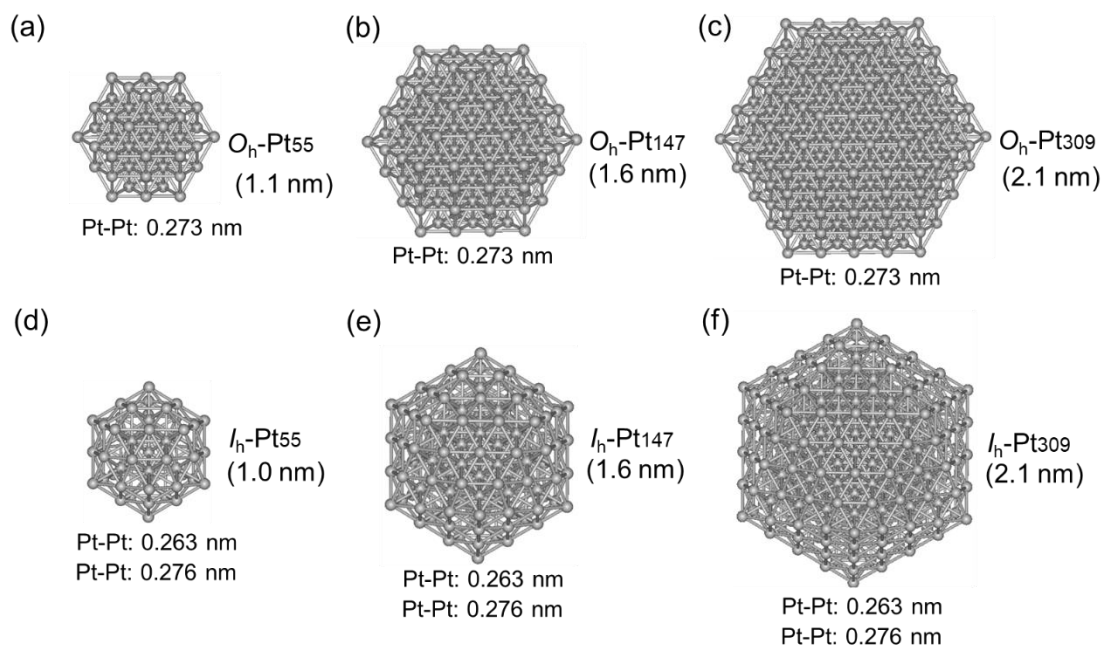


Figure 5-10. Structures of Pt clusters used for FEFF calculation to fit the PTRF-EXAFS spectra of the Pt species on the α -Al₂O₃(0001) surface at 493 K in the reactant gases (CO:O₂:Ar = 20%:72%:8%, 100 Pa). (a) O_h-Pt₅₅, (b) O_h-Pt₁₄₇, (c) O_h-Pt₃₀₉, (d) I_h-Pt₅₅, (e)

I_h-Pt₁₄₇, (f) I_h-Pt₃₀₉. Cluster size and Pt-Pt bond distances are also illustrated. In the I_h-cluster structures, the shorter Pt-Pt bond corresponds to intershell bonds while the longer one to intrashell bonds.

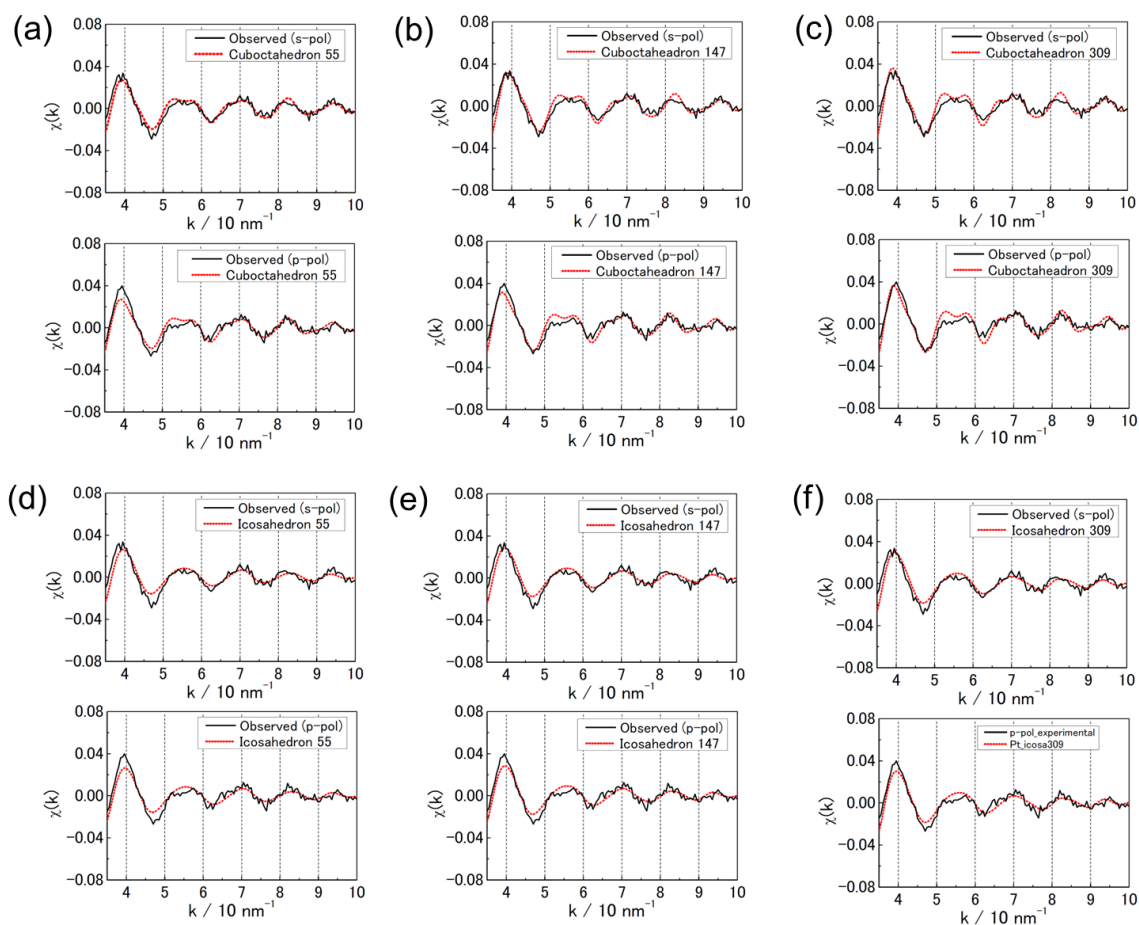


Figure 5-11. Series of calculated EXAFS oscillations for the Pt species on the α -Al₂O₃(0001) surface at 493 K in the reactant gases using the Pt cluster structures shown in Figure 5-8. (a) O_h-Pt₅₅, (b) O_h-Pt₁₄₇, (c) O_h-Pt₃₀₉, (d) I_h-Pt₅₅, (e) I_h-Pt₁₄₇, (f) I_h-Pt₃₀₉.

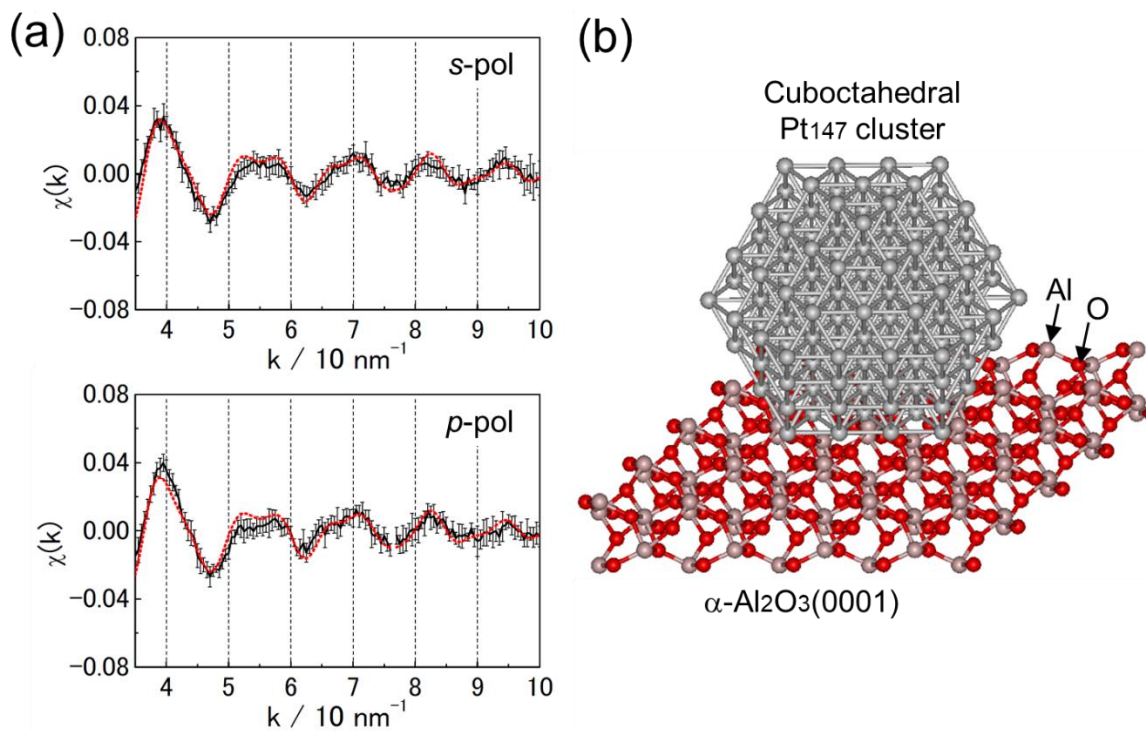


Figure 5-12. (a) Observed (black solid line) and calculated (red dotted line) EXAFS spectra for the Pt species on the $\alpha\text{-Al}_2\text{O}_3(0001)$ surface during CO oxidation reaction at 493 K. Errors of the observed spectra are also shown. The $\text{O}_h\text{-Pt}_{147}$ cluster model illustrated in panel b was assumed for the calculation, and the $\alpha\text{-Al}_2\text{O}_3(0001)$ support was not included in the calculation. The Pt–Pt bond distance is 0.273 nm.

References

- [1] J. J. H. B. Sattler, J. Ruiz-Martinez, E. Santillan-Jimenez, and B. M. Weckhuysen, “Catalytic Dehydrogenation of Light Alkanes on Metals and Metal Oxides,” *Chem. Rev.*, vol. 114, no. 20, pp. 10613–10653, Oct. 2014
- [2] M. R. Rahimpour, M. Jafari, and D. Iranshahi, “Progress in catalytic naphtha reforming process: A review,” *Applied Energy*, vol. 109, pp. 79–93, Sep. 2013.
- [3] D. Duprez, C. Descorme, T. Birchem, and E. Rohart, “Oxygen Storage and Mobility on Model Three-Way Catalysts,” *Topics in Catalysis*, vol. 16, no. 1, pp. 49–56, Sep. 2001.
- [4] T. Isono, T. Ikeda, R. Aoki, K. Yamazaki, and T. Ogino, “Structural- and chemical-phase-separation on single crystalline sapphire (0001) surfaces,” *Surface Science*, vol. 604, no. 21, pp. 2055–2063, Oct. 2010.
- [5] J. H. Scofield, “Hartree-Slater subshell photoionization cross-sections at 1254 and 1487 eV,” *Journal of Electron Spectroscopy and Related Phenomena*, vol. 8, no. 2, pp. 129–137, Jan. 1976.
- [6] J. J. Yeh and I. Lindau, “Atomic subshell photoionization cross sections and asymmetry parameters: $1 \leq Z \leq 103$,” *Atomic Data and Nuclear Data Tables*, vol. 32, no. 1, pp. 1–155, Jan. 1985.
- [7] S. Tanuma, C. J. Powell, and D. R. Penn, “Calculations of electron inelastic mean free paths for 31 materials,” *Surface and Interface Analysis*, vol. 11, no. 11, pp. 577–589, 1988.

- [8] M. Nomura and A. Koyama, "Performance of a beamline with a pair of bent conical mirrors," *Nuclear Instruments and Methods in Physics Research Section A: Accelerators, Spectrometers, Detectors and Associated Equipment*, vol. 467–468, pp. 733–736, Jul. 2001.
- [9] T. Taguchi, T. Ozawa, and H. Yashiro, "REX2000: yet another XAFS analysis package," *Phys. Scr.*, vol. 2005, no. T115, p. 205, Jan. 2005.
- [10] A. L. Ankudinov, B. Ravel, J. J. Rehr, and S. D. Conradson, "Real-space multiple-scattering calculation and interpretation of x-ray-absorption near-edge structure," *Phys. Rev. B*, vol. 58, no. 12, pp. 7565–7576, Sep. 1998.
- [11] Y. Lei, J. Jelic, L. C. Nitsche, R. Meyer, and J. Miller, "Effect of Particle Size and Adsorbates on the L3, L2 and L1 X-ray Absorption Near Edge Structure of Supported Pt Nanoparticles," *Top Catal*, vol. 54, no. 5, pp. 334–348, Apr. 2011.
- [12] S. Takakusagi, Y. Iwasawa, and K. Asakura, "Premodified Surface Method to Obtain Ultra-Highly Dispersed Metals and their 3D Structure Control on an Oxide Single-Crystal Surface," *The Chemical Record*, vol. 19, no. 7, pp. 1244–1255, 2019.
- [13] J. A. Alonso, "Electronic and Atomic Structure, and Magnetism of Transition-Metal Clusters," *Chem. Rev.*, vol. 100, no. 2, pp. 637–678, Feb. 2000.
- [14] F. Baletto and R. Ferrando, "Structural properties of nanoclusters: Energetic, thermodynamic, and kinetic effects," *Rev. Mod. Phys.*, vol. 77, no. 1, pp. 371–423, May 2005.

- [15] E. Aprà and A. Fortunelli, “Density-Functional Calculations on Platinum Nanoclusters: Pt₁₃, Pt₃₈, and Pt₅₅,” *J. Phys. Chem. A*, vol. 107, no. 16, pp. 2934–2942, Apr. 2003.
- [16] A. Beniya, N. Isomura, H. Hirata, and Y. Watanabe, “Morphology and chemical states of size-selected Pt_n clusters on an aluminium oxide film on NiAl(110),” *Physical Chemistry Chemical Physics*, vol. 16, no. 48, pp. 26485–26492, 2014.
- [17] F. Baletto, R. Ferrando, A. Fortunelli, F. Montalenti, and C. Mottet, “Crossover among structural motifs in transition and noble-metal clusters,” *The Journal of Chemical Physics*, vol. 116, no. 9, pp. 3856–3863, Mar. 2002.

CHAPTER 6

ELUCIDATING ACTIVATION ENERGY CHANGE TOWARDS
CO OXIDATION ON Pt/ α -Al₂O₃(0001) VIA *in situ/operando*
PTRF-XAFS

Platinum is a practical important catalyst for catalyzing redox reactions and widely used in the treatment of toxic gases. To get higher stability and economic benefit, Pt is usually dispersed on the surface of oxide nanoparticles. Pt/ γ -Al₂O₃ therefore is widely used in the exhaust pipe in automobile to reduce the toxicity of exhaust. α -Al₂O₃ is applied as the oxide support in this research because it has much lower structure complexity and catalytic activity and is easier to obtain a single crystal surface, which is significant to synthesize model catalyst. The apparent activation energy, which is usually determined by the intrinsic activity of the catalysts, is a quantity that can be measured directly by fitting the temperature dependence of the reaction rate to the Arrhenius law. It provides fundamental understanding of the reaction kinetics and mechanisms if one can correlate the microscopic origin / elementary steps to the macroscopic / overall reactions.

In this chapter, the newly modified flow-type *in situ* PTRF-XAFS cell was applied to a Pt/ α -Al₂O₃(0001) model catalyst surface during CO oxidation reaction to reveal the adsorbates on the Pt nanocluster surface at different temperatures regimes.

6.1 Temperature dependence of activation energy towards CO oxidation on the Pt/ α -Al₂O₃(0001)

A one side polished square-shaped α -Al₂O₃(0001) single crystal with the side length of 15 mm and thickness of 0.5 mm (Shinkosha. Co., Ltd.) was used as the substrate surface. It was annealed in air at 1323 K for 3 h and followed by keeping at 873 K for 3 h to obtain an atomically flat α -Al₂O₃(0001) surface [1]. The surface morphology was checked using atomic force microscopy (AFM) that monatomic step and terrace structures were confirmed on the entire surface as shown in (Figure 6-1). The sample was then transferred into the ultra-high vacuum (UHV) chamber mentioned above (base pressure: 2×10^{-8} Pa, refer to Chapter 2) and heated at 873 K to degas after one night evacuation. The surface showed a (1 \times 1) pattern by low-energy electron diffraction (LEED) measurements (Figure 6-2). Pt was deposited by Pt vapor generation through electron bombardment of a Pt rod (99.98%, Nilaco Co., Japan) with application of a high voltage (typically 850 V) between the filament and the Pt rod. The Pt coverage was estimated to be 0.3 ML from the X-ray photoelectron spectroscopy (XPS) peak area ratio of Pt 4d_{3/2} to Al 2s as shown in Figure 6-3, where 1 ML was defined as 5.1×10^{14} /cm² with correspondence to the density of surface Al atoms on the α -Al₂O₃(0001) substrate.

The sample was then transferred into the newly modified flow-type reactor (see section 2.4 for detail) through the load-lock chamber following the manner described in section 2.1. Figure 6-4 shows the schematic diagram of the specialized setup for the reactions. CO (99.995%) and O₂ (10% Ar) cylinders were connected to the reactor to supply the reactant gases and their flow rates were controlled by two mass-flow controllers (MKS, max flow rate: 10 sccm), respectively. A power supply and a PID

controller were connected to silicon heater and thermocouple via terminals at backside of the holder, respectively, so that the sample in the reactor can be heated at high temperature (< 800 K) in a controllable way in the presence of reactant gases. The products that generated from the sample surface can be sampled by the sampling tube (diameter: $\frac{1}{2}$ inch) that approached to the surface using a linear motion manipulator (AVC, ALMB-133/30). The distance between the sample surface and the sampling tube was set approximately to 0.5 mm to ensure the mass transfer and sufficient production sampling. The sampled mixture was differential pumped to the quadrupole mass spectrometer (QMS) for component analysis.

Firstly, the performance of the flow-type reactor was tested by the CO oxidation activity measurements for the Pt/ α -Al₂O₃(0001) surface. The result was shown in Figure 6-5. The production of CO₂ was successfully detected at temperatures higher than 470K. This temperature is a little higher than that of in Chapter which determined by using the batch-type cell during the *operando* PTRF-XAFS measurements. It is probably affected by two origins. The first one is due to the detection limit of the flow-type cell. In the batch-type cell, the produced CO₂ was accumulated in the cell so that even if the reaction rate was extremely low, they can be captured and visualized by QMS. However, in the case of the flow-type reactor, the reactant gases were continuously supplied and impinged on the sample surface. The whole reactor was evacuated by turbo molecular pump and / or dry pump all the time. It means the concentration of the produced CO₂ was kept at an ultra-low level inside the reactor. A relatively high production rate of CO₂, which corresponded to a higher reaction temperature, was required to achieve the detection limit of the QMS. The second origin is the pressure difference between the current system and

the batch-type one. In this measurement, the total pressure of the reactants and product inside the reactor was kept lower than 25 Pa to avoid the damage to the evacuation system. This pressure was much lower than that was used in the *operando* PTRF-XAFS measurements (total pressure: 250 Pa). The difference in the pressure may induce a change in the processes of adsorption and desorption or even a further modification to the structure of the supported metals and lead to a deviation in the catalytic activity of the catalyst. Moreover, a deactivation region was found when the surface temperature was higher than 590 K. It was reported that deeply oxidized Pt(111) surface showed lower reactivity towards CO oxidation [2]. However, the materials gap between the supported metals and metal single crystals must be always minded. Therefore, further experiments (see section 6.2 for details) were conducted to provide firm evidence.

Secondly, a measurement that can hardly be done by the former batch-type reactor was conducted using the updated flow-type reactor, i.e., the partial pressure dependence of the CO oxidation activity on the Pt/ α -Al₂O₃(0001) surface (Figure 6-6). The Pt/ α -Al₂O₃(0001) surface was heated in the CO and O₂ gas mixture (ratio close to 1 : 1). When the production of CO₂ can be clearly confirmed and the temperature at 550 K, the flow rate of O₂ (Figure 6-6a) and CO (Figure 6-6b) was stepwise increased, respectively. The variation of the total pressure in the reactor was kept less than 200% versus the initial pressure (0.8 Pa). Clearly different responses towards the partial pressure change were observed. When the partial pressure of the O₂ gas increased, the production rate of CO₂ also increased. On the other hand, there was a slight inverse proportional relationship between the CO partial pressure and the reaction rate when CO was the dominant gas at this temperature. It is consistent with the studies conducted on the Pt single crystal

surfaces. The basic idea to interpret this result is that when the CO partial pressure is comparable with or higher than that of O₂, at relatively low temperatures, the surface of the metal species is almost fully covered by CO molecules because their sticking coefficient close to the unity. These CO molecules occupy most of the adsorption sites as an inhibitor so that O₂ molecules can hardly access these sites. For a limited number of vacancy sites, the increase of the O₂ partial pressure therefore leads to a higher reaction rate to CO₂.

In order to evaluate the reactivity of the Pt/ α -Al₂O₃(0001) model surface, I convert the reaction rate of CO₂ to the Arrhenius plot to estimate the apparent activation energy of the reaction on the catalyst surface. Then I found different apparent activation energies above and below an ignition temperature (Figure 6-7a). Similar phenomena was observed for the CO oxidation on Pt(111), Pd(111) and Ru(0001) surfaces [5-7]. However, as far as I know it was not reported for the oxide-supported metals. The partial pressure dependence of the ignition temperature was examined as shown in Figure 6-7. For higher O₂ partial pressure, the ignition temperature shifted to lower side. I therefore thought that the potential interpretations for this phenomenon would be the change of the dominant adsorbates or / and of the reaction mechanism.

6.2 Investigation of adsorbates on Pt/ α -Al₂O₃(0001) during CO oxidation

To investigate the origin of the apparent activation energy change and deactivation towards CO oxidation, *in situ* PTRF-XAFS measurements of the Pt/ α -Al₂O₃(0001) surface under corresponding CO oxidation reaction conditions were conducted. The same procedures for sample preparation for a Pt/ α -Al₂O₃(0001) surface with Pt coverage of 0.3 ML were conducted in the UHV system that was introduced in section 2.2. After the

preparation the sample was transferred to the flow-type *in situ* PTRF-XAFS cell. The cell was then detached and transferred to the hutch in the beamline. The sample in the cell was kept in UHV by using the non-evaporable getter (NEG) pump during the transfer to the hutch, and the PTRF-XAFS measurements were conducted after attaching the cell to the goniometer and optimizing the total reflection conditions for the incident X-rays at the BL9A beamline [8] of the Photon Factory at the Institute of Materials Structure Science (KEK-IMSS-PF, Tsukuba, Japan). The storage ring energy and ring current were 2.5 GeV and 450 mA, respectively. X-rays were monochromatized with a Si(111) double-crystal monochromator that was focused by using a pair of bent conical mirrors, and the beam size on the sample was regulated with a pinhole (0.4 mm diameter) to reduce undesirable irradiation (Figure 4-6 in section 4.1). The total reflection conditions were adjusted using a 6-axis goniometer (see Figure 2-10 in section 2.3).

Figure 6-9 compares the PTRF-XANES of the Pt L₃ edge of the Pt/ α -Al₂O₃(0001) measured under different conditions. The sample was reduced in H₂ at 573 K [9, 10] after one cycle of CO oxidation at 653K with CO (flow rate: 0.33 sccm) and O₂ (flow rate: 1.00 sccm). The sample was kept at 573 K after cutting out the H₂ flow to remove the surface adsorbed hydrogen [11]. The *in situ* PTRF-XANES spectra were recorded under steady-state conditions in UHV at 573 K, CO at room temperature, O₂ at 523 K, and O₂ at 573 K, respectively. They were assigned to be the reference states as clean, CO covered, oxygen adsorbed, and oxidized surface, respectively. The variations in the shape of the white line were affected by the change in atmosphere. The difference spectra of these surfaces are shown in Figure 6-8b, where the reference state of clean surface was used to create the spectra ($E_0 = 11562$ eV). The oxidized surface showed a stronger intensity at

the edge and a weaker one at approximately 9 eV above the edge while the CO covered surface showed an inverted however weaker feature, which was in line with the previous reported XANES of CO covered Pt nanocluster surface [12, 13].

Figure 6 – 8a shows the PTRF-XANES of the Pt L₃ edge of the Pt/ α -Al₂O₃(0001) measured at different temperatures under the gas flow conditions (CO flow rate: 0.33 sccm; O₂ flow rate: 1.00 sccm, total pressure in the cell: 1.8 Pa) after one cycle of CO oxidation at 653K with the same reactant gas mixture flow. The four temperatures can be divided into three groups which correspond to deactivated (653 K), low apparent activation energy (583 K), and high apparent activation energy (503 K and 473 K) regimes, respectively. A clear trend was observed that the trough feature (~ 11570 eV) just after white line got lower at higher temperatures while the difference between at 503 K and 473 K was small in both polarizations. Their difference spectra are shown in Figure 6 – 8b, where the reference state of clean surface obtained in UHV at 573 K after reduction by H₂. At 653 K, the XANES spectra in both polarizations showed similar features with the oxidized reference spectra. It indicated that the Pt species was oxidized under this condition, which consistent with the conclusion that the oxidized surface presented lower reactivity towards the CO oxidation because CO is unlikely to adsorb on or react with defect-free α -PtO₂(0001) surfaces [14]. The spectra obtained at 583 K showed a very close feature with that of the oxygen adsorbed surface at the edge at meanwhile with a little similarity with the oxidized surface at 10 eV above the edge. It may correspond to an oxygen adsorbed and / or partially oxidized Pt species. According to the difference spectra obtained at 503 K and 473 K, the surface states of the supported Pt species would be basically covered by CO with different coverage. Therefore, the

apparent activation energy mainly consisted of the desorption energy of CO from the Pt species surface.

Furthermore, a surprisingly polarization dependence was observed in the PTRF-XANES spectra obtained at 653 K during the CO oxidation reaction as shown in Figure 6-10. As far as I know the *in situ* PTRF-XAFS should be the only technique that can capture such kind of features at present. I may indicate different adsorbate species or oxidation state in different orientations of the Pt species supported by the α -Al₂O₃(0001) surface at high temperatures. However, this was not discussed in detail in this report as there was not enough time to conduct theoretical analysis, which would be very time-consuming work, especially for XANES simulations.

6.3 Conclusions

The newly constructed flow-type reactor was applied to investigate the catalytic CO oxidation on the Pt/ α -Al₂O₃(0001) surface. Two different apparent activation energies were found below and above a distinct ignition temperature. The ignition temperature showed a partial pressure dependence. In this work, the O₂ to CO partial pressure ratio varied from approximately 1 to 3 and the corresponding ignition temperature shifted from approximately 540 K to 510 K. Moreover, a decrease in the reactivity of the Pt/ α -Al₂O₃(0001) surface was found at temperature higher than 590 K.

The *in situ* XAFS measurements of the Pt/ α -Al₂O₃(0001) surface under the corresponding CO oxidation conditions were conducted by using the flow-type reactor as an *in situ* PTRF-XAFS cell. By comparing the PTRF-XANES spectra with the referenced spectra, which were also measured by using the same cell, one can conclude

that the presence of the different apparent activation energies should tightly relate to surface states of the Pt species. In the high apparent activation energy regime, the Pt surface was basically covered with CO thus limited vacancy sites were available for O₂ adsorption. Although the number of vacancy sites increased with the temperature so that the apparent reaction rate increased as well, the desorption energy was still a major part of the apparent activation energy. In the low activation energy regime, the Pt surface was affected by oxygen however with sufficient sites for CO adsorption and reaction with oxygen. The deactivated state would relate with the deeply oxidized surface of the Pt species. The sticking coefficient decreased dramatically on such surfaces so that the apparent reaction rate was suppressed.

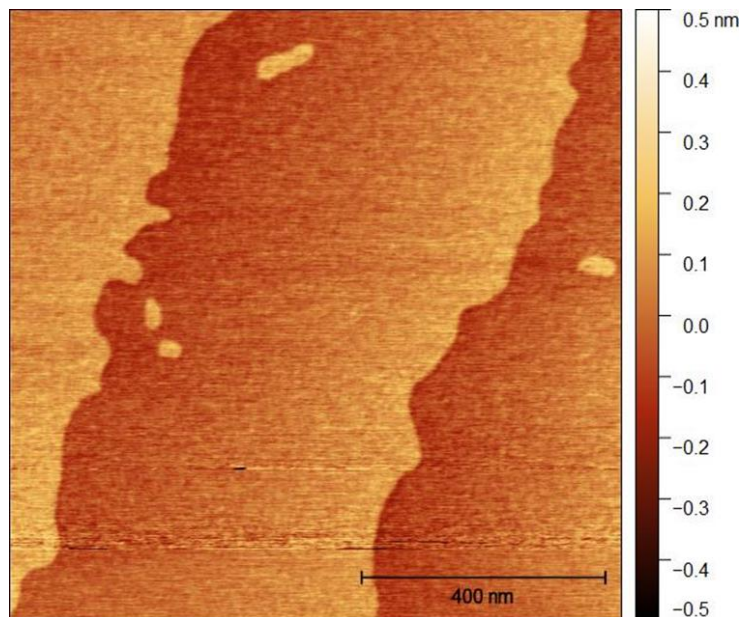


Figure 6-1. AFM image of clean $\alpha\text{-Al}_2\text{O}_3(0001)$ surface.

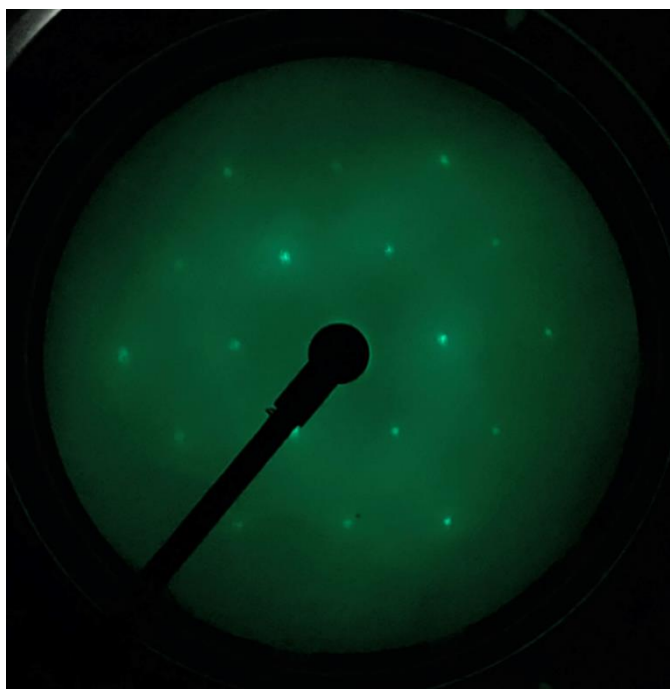


Figure 6-2. (1×1) LEED pattern of $\alpha\text{-Al}_2\text{O}_3(0001)$ clean surface, probe electron energy = 130 eV.

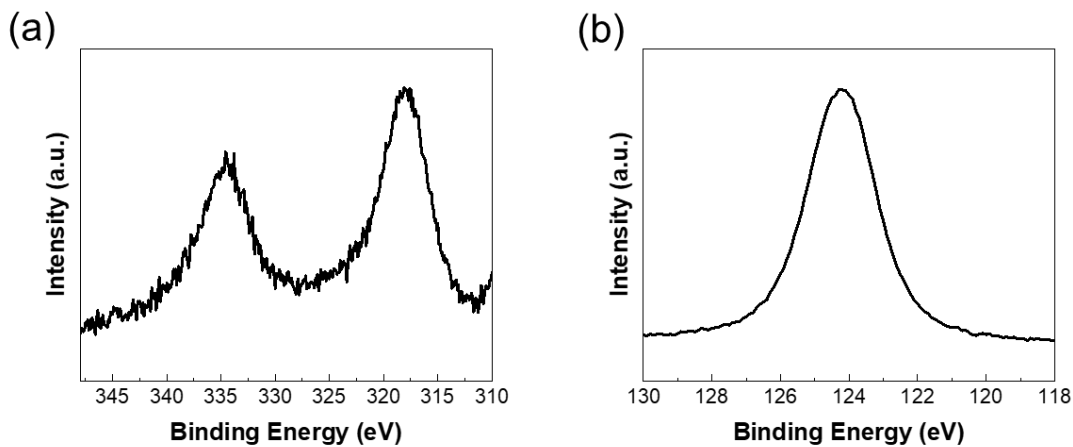


Figure 6-3. (a) Pt 4d and (b) Al 2s XPS recorded after the UHV Pt deposition at room temperature.

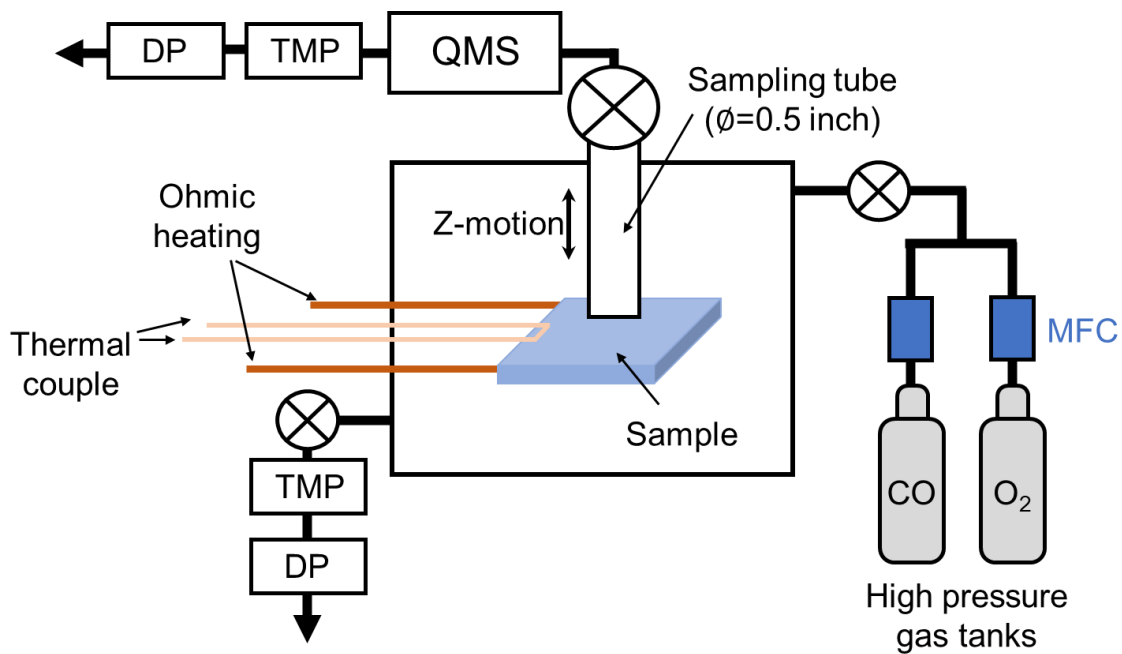


Figure 6-4. Schematic of the modified flow-type cell.

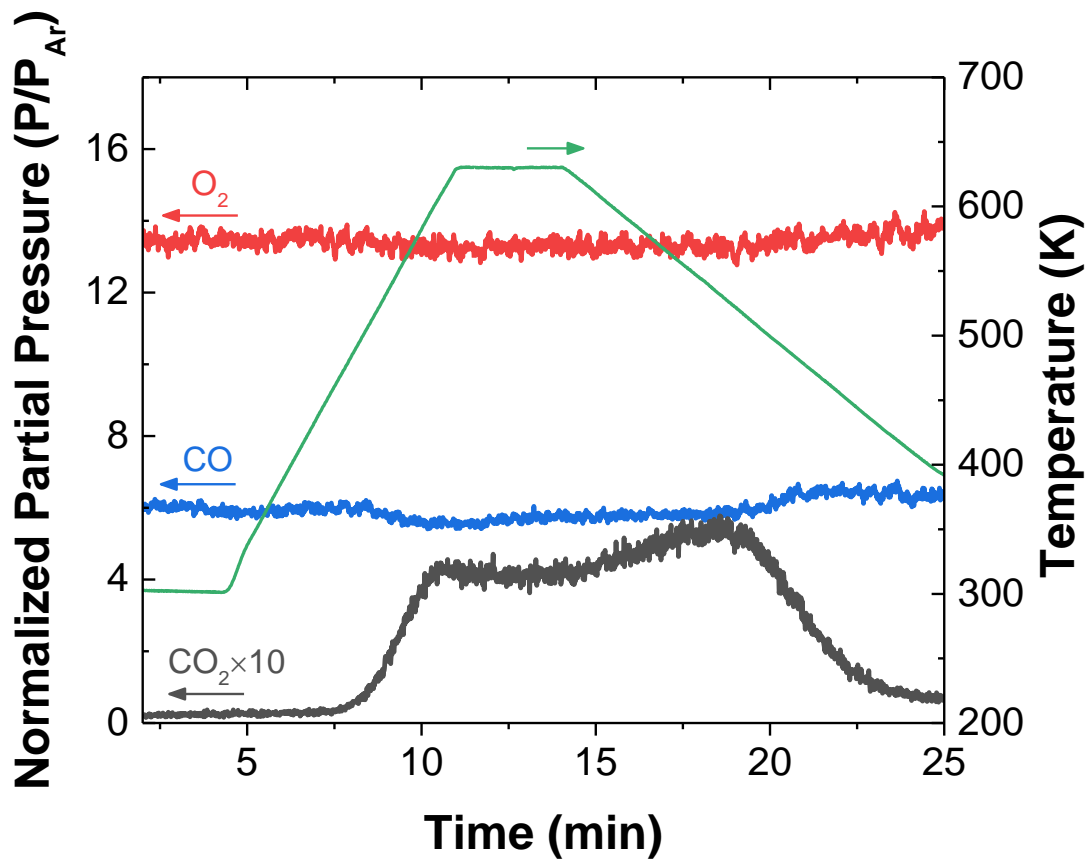


Figure 6-5. CO oxidation activity measurements for the Pt/ α -Al₂O₃(0001) surface using the flow-type cell. The reactant gases were introduced into the cell at constant flow rate by MFCs. The reaction was monitored using the QMS. Ar was used as an internal standard gas.

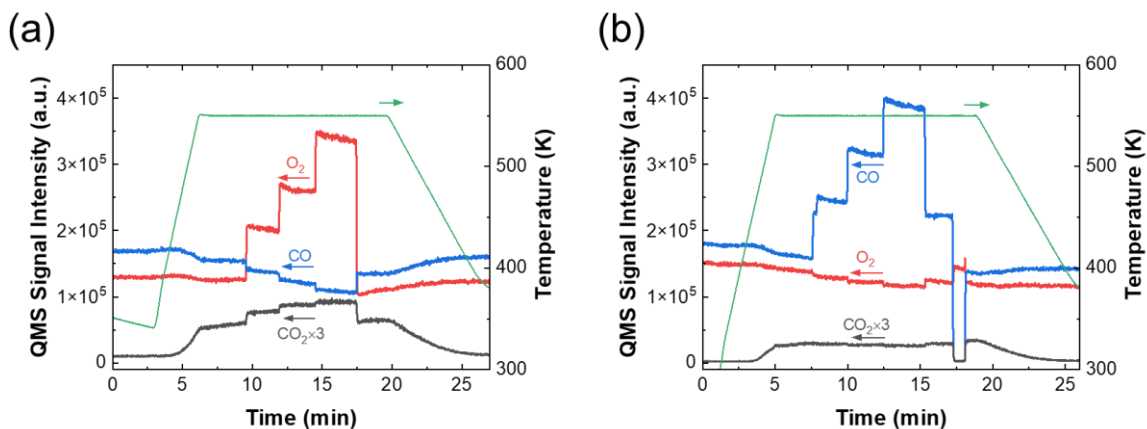


Figure 6-6. The (a) O₂ and (b) CO partial pressure dependence of the CO oxidation activity on the Pt/ α -Al₂O₃(0001) surface measured using the flow-type cell.

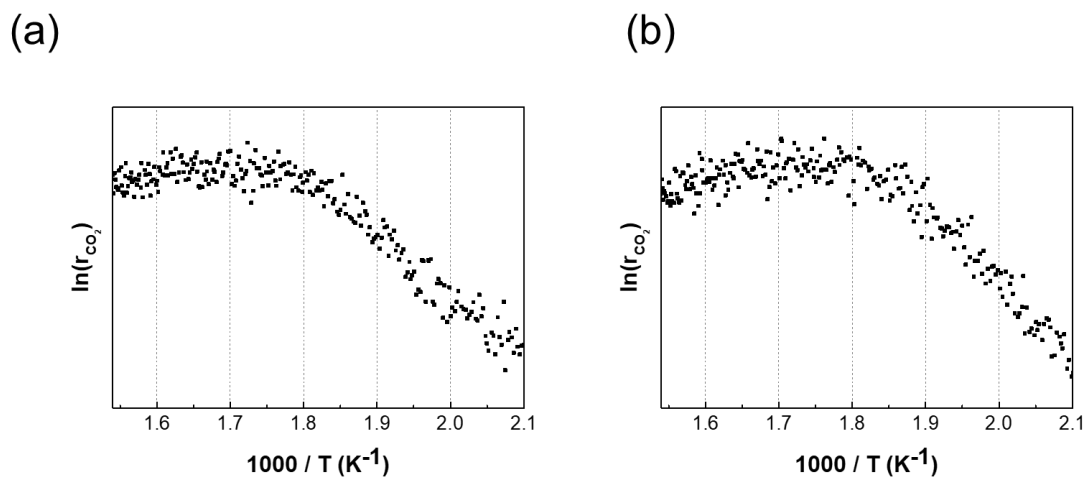


Figure 6-7. Rates for CO oxidation on Pt/ α -Al₂O₃(0001) as function of temperature for O₂ to CO partial pressure ratio of (a) 1 and (b) 3.

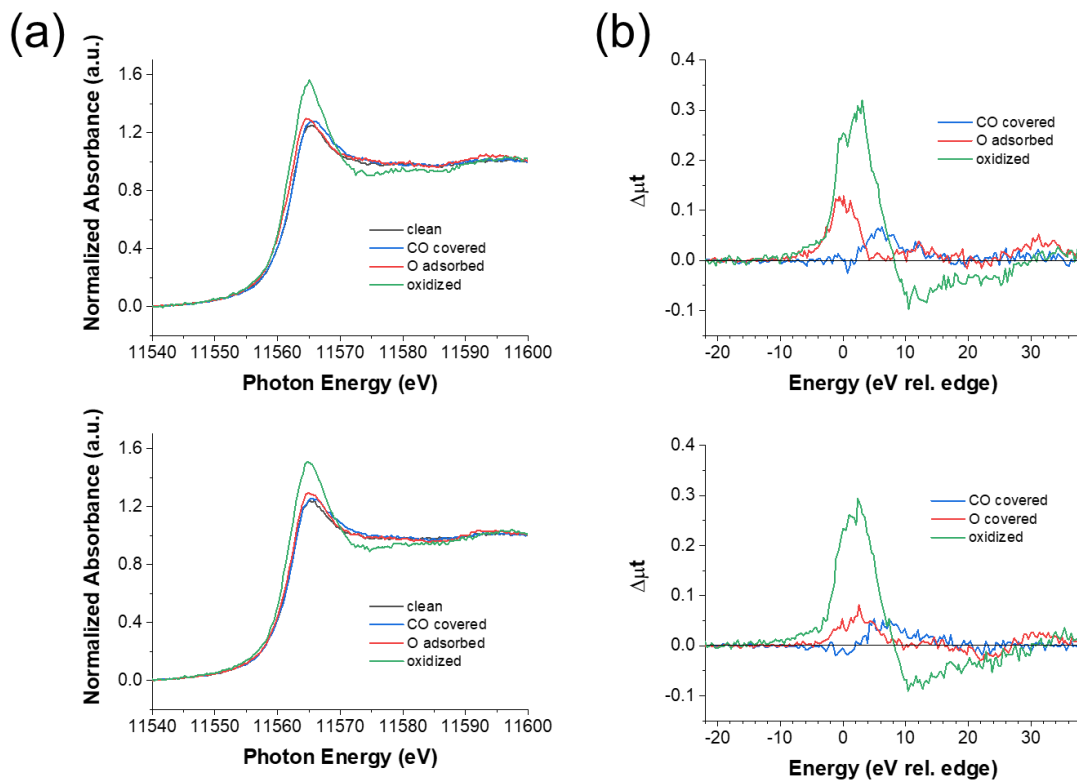


Figure 6-8. (a) PTRF-XANES spectra at Pt L3-edge of clean, CO covered, oxygen adsorbed, and oxidized Pt species on α -Al₂O₃(0001) surface and (b) corresponding difference spectra using clean surface as the reference.

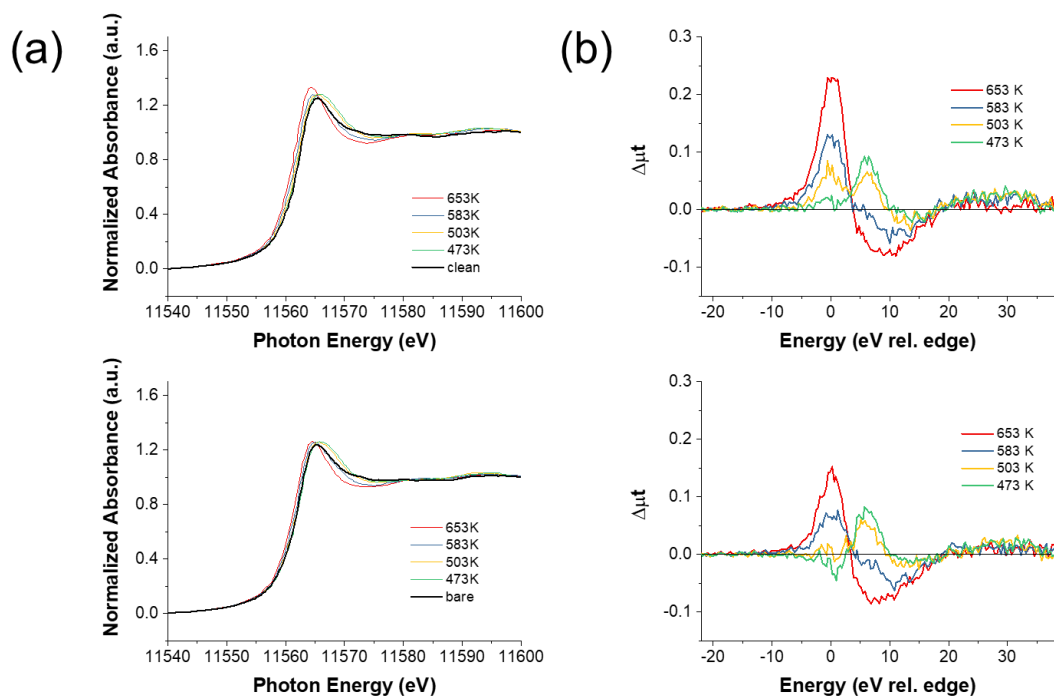


Figure 6-9. (a) Pt L3-edge PTRF-XANES spectra of the Pt/ α -Al₂O₃(0001) surface obtained at 473K, 503K, 583K, and 653K during the CO oxidation reaction and (b) corresponding difference spectra using clean surface as the reference.

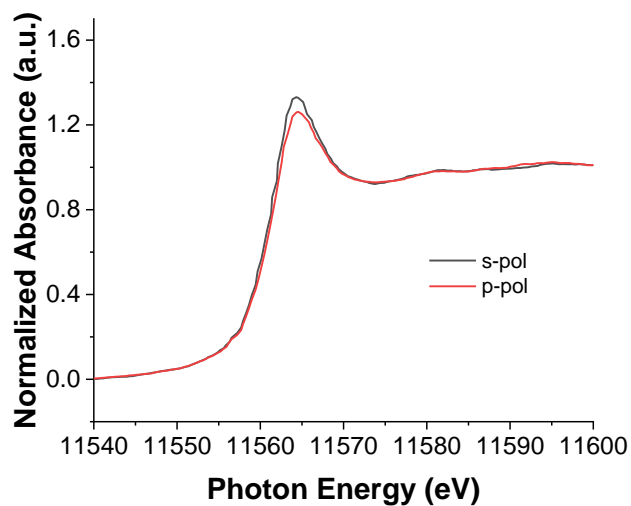


Figure 6-10. Polarization dependence of Pt L3-edge XANES spectra of the Pt/ α -Al₂O₃(0001) surface obtained at 653K during the CO oxidation reaction.

References

- [1] T. Isono, T. Ikeda, R. Aoki, K. Yamazaki, and T. Ogino, “Structural- and chemical-phase-separation on single crystalline sapphire (0001) surfaces,” *Surface Science*, vol. 604, no. 21, pp. 2055–2063, Oct. 2010.
- [2] D. Miller, H. Sanchez Casalongue, H. Bluhm, H. Ogasawara, A. Nilsson, and S. Kaya, “Different Reactivity of the Various Platinum Oxides and Chemisorbed Oxygen in CO Oxidation on Pt(111),” *J. Am. Chem. Soc.*, vol. 136, no. 17, pp. 6340–6347, Apr. 2014.
- [3] J. Liu, “Sticking Probabilities for CO Adsorption on Pt(111) Surfaces Revisited”.
- [4] R. M. Eiswirth, K. Krischer, and G. Ertl, “Nonlinear dynamics in the CO-oxidation on Pt single crystal surfaces,” *Appl. Phys. A*, vol. 51, no. 2, pp. 79–90, Aug. 1990.
- [5] X. Su, P. S. Cremer, Y. R. Shen, and G. A. Somorjai, “High-Pressure CO Oxidation on Pt(111) Monitored with Infrared–Visible Sum Frequency Generation (SFG),” *J. Am. Chem. Soc.*, vol. 119, no. 17, pp. 3994–4000, Apr. 1997.
- [6] T. Engel and G. Ertl, “A molecular beam investigation of the catalytic oxidation of CO on Pd(111),” *J. Chem. Phys.*, vol. 69, no. 3, pp. 1267–1281, Aug. 1978.
- [7] C. H. F. Peden and D. W. Goodman, “Kinetics of carbon monoxide oxidation over ruthenium(0001),” *J. Phys. Chem.*, vol. 90, no. 7, pp. 1360–1365, Mar. 1986.
- [8] M. Nomura and A. Koyama, “Performance of a beamline with a pair of bent conical mirrors,” *Nuclear Instruments and Methods in Physics Research Section*

- A: Accelerators, Spectrometers, Detectors and Associated Equipment, vol. 467–468, pp. 733–736, Jul. 2001.
- [9] T. Huizinga, J. Van Grondelle, and R. Prins, “A temperature programmed reduction study of Pt on Al₂O₃ and TiO₂,” *Applied Catalysis*, vol. 10, no. 2, pp. 199–213, May 1984.
- [10] M. Fujita, A. Yamamoto, N. Tsuchiya, and H. Yoshida, “Hydrogen Adsorption/Desorption Isotherms on Supported Platinum Nanoparticles Determined by in-situ XAS and Δ XANES Analysis,” *ChemCatChem*, vol. 14, no. 5, p. e202101709, 2022.
- [11] E. Bus and J. A. van Bokhoven, “Hydrogen chemisorption on supported platinum, gold, and platinum–gold-alloy catalysts,” *Phys. Chem. Chem. Phys.*, vol. 9, no. 22, pp. 2894–2902, May 2007.
- [12] T. Kubota, K. Asakura, and Y. Iwasawa, “Quantitative analysis of hydrogen adsorbed on Pt particles on SiO₂ in the presence of coadsorbed CO by means of L3-edge X-ray absorption near-edge structure spectroscopy,” *Catalysis Letters*, vol. 46, no. 3, pp. 141–144, Jul. 1997.
- [13] Y. Lei et al., “Adsorbate-Induced Structural Changes in 1–3 nm Platinum Nanoparticles,” *J. Am. Chem. Soc.*, vol. 136, no. 26, pp. 9320–9326, Jul. 2014.
- [14] D. Miller, H. Sanchez Casalongue, H. Bluhm, H. Ogasawara, A. Nilsson, and S. Kaya, “Different Reactivity of the Various Platinum Oxides and Chemisorbed Oxygen in CO Oxidation on Pt(111),” *J. Am. Chem. Soc.*, vol. 136, no. 17, pp. 6340–6347, Apr. 2014.

CHAPTER 7

GENERAL CONCLUSIONS

The body of this work was centrally focused on elucidating the structure-activity relationship for model catalyst surfaces mainly using a newly developed *in situ / operando* surface science technique. The development of this *in situ / operando* PTRF-XAFS technique was motivated by the curiosity of knowing the detailed information on the three dimensional geometric and electronic structures of the catalyst surface during the catalytic reactions. After its construction, it was applied to an atomically dispersed Cu/ α -Al₂O₃(0001) surface under UHV condition, and Pt clusters on α -Al₂O₃(0001) surface under CO oxidation conditions to investigate the atomic level 3D structure and electronic states of the supported metal species.

For the plasma-assisted ammonia synthesis work detailed in Chapter 3, the central conclusion is that nitrogen can adsorb on the Co surface in an efficient way (sticking coefficient estimated to be $\sim 6 \times 10^{-3}$) and be further hydrogenated with the assistance of ECR plasma at room temperature. The excited nitrogen molecules and atomic nitrogen were considered as the candidate active species from the nitrogen plasma phase for the adsorption process on Co surface. The thermodynamic analysis showed an endothermic process during the nitrogen adsorption and the kinetic analysis suggested that the apparent adsorption rate of nitrogen was greater than the rate of impinging from the atomic nitrogen in the plasma phase. It suggested that atomic nitrogen may not be the only active species in the nitrogen plasma that contributed to the nitrogen adsorption process on the Co surface.

The future work that can be adopted for Chapter 3 would be first to determine the reactivity of the Co surface by detecting the formation of the ammonia product. It is difficult to do at present because the materials used for the vacuum components such as the reactor and sampling tube are made of stainless steel (SUS) contains iron, which is a good catalyst surface for ammonia adsorption. Therefore, the produced ammonia molecules can easily be captured by the wall of the reactor and sampling tube and no signal from ammonia can be observed before they are saturated. This huge delay would be a stumbling block in the reactivity analysis. Second, although both the thermodynamic and kinetic analysis suggested the contribution of vibrationally excited nitrogen molecules, a control experiment that measure the adsorption rate of nitrogen by changing the N to N(v) ratio to obtain firm supporting evidence to the conclusion. Another way would be to compare the apparent adsorption energy with the adsorption energy of atomic nitrogen and vibrationally excited nitrogen molecules based on the theoretical models. The last one would be to investigate the structure of Co species during the plasma-assisted surface processes by using the developed *in situ* PTRF-XAFS technique to establish the structure-activity relationship for such cutting-edge catalytic systems.

The first trial of newly constructed *operando* PTRF-XAFS cell was conducted under UHV condition in Chapter 4. Highly dispersed Cu species on α -Al₂O₃(0001) surface was used as the model surface. The ultra-diluted sample surface ($9.7 \times 10^{13} \text{ cm}^{-2}$) was a great challenge to acquire meaningful data. Fortunately, both the XANES and EXAFS in two polarization directions were successfully obtained. XANES spectra indicated that the Cu species form on the α -Al₂O₃(0001) surface at this low coverage (1.9 ML) would be monovalent. Based on the real-space model structures of Cu atoms situated

at a series of sites including three different oxygen hollow sites and two types of oxygen bridge sites on ideal and relaxed α - $\text{Al}_2\text{O}_3(0001)$ surfaces, FEFF code was applied to simulate the PTRF-EXAFS spectra. The Cu atom put at an oxygen bridge site on the relaxed surface with Cu-O bond length at 0.194 nm reproduced well the experimental spectra in both s- and p-polarization directions. It therefore can be concluded that the Cu species was atomically dispersed and stabilized by the surface oxygens of the relaxed α - $\text{Al}_2\text{O}_3(0001)$ surface.

The future work that can be adopted for Chapter 4 would be the application of a more efficient analysis method for the PTRF-EXAFS spectra. Due to the limitations of manpower and computational resources, only finite number of real-space models can be taken into consideration based on the knowledge of surface science and chemistry. However, small distortion of structure or anomalous sites can hardly be aware. Moreover, the Cu/ Al_2O_3 is a well-known catalyst for NO decomposition. The *in situ* / *operando* PTRF-XAFS technique can be applied to investigate the relationship between the NO decomposition activity and the local 3D structure of the Cu single site on the Al_2O_3 single crystal surface would be an interesting topic.

The application of *operando* PTRF-XAFS technique to a Pt/ α - $\text{Al}_2\text{O}_3(0001)$ model catalyst surface during the CO oxidation reaction was the central content of Chapter 5. Icosahedral Pt₅₅ cluster was initially formed on the α - $\text{Al}_2\text{O}_3(0001)$ surface at room temperature. When the surface was heated in the reactant gases, the Pt species were gradually reduced due to partial desorption of CO and showed activity for CO oxidation reaction at high temperatures. The Pt species then converted mainly to cuboctahedral Pt₁₄₇ cluster when the CO oxidation reaction was taking place at 493K. The turnover

frequency (TOF) per surface Pt atom at 493 K was estimated to be 0.06 s^{-1} based on the Pt cluster structure.

The final chapter of this work was concerned with the use of the newly upgraded flow-type *in situ* PTRF-XAFS cell. It enabled me to monitor the 3D structure of the supported metal species under steady state span over the long XAFS measurement time periods, especially of highly active catalysts. Temperature regimes presented two different apparent activation energies and deactivation towards CO oxidation on Pt/ α -Al₂O₃(0001) was found using the abovementioned flow-type cell. The results of the *in situ* PTRF-XAFS measurements provided the hint to the origin of the changes related to the surface states such as adsorbed species and oxidation states of the Pt species at different temperatures in the environment of CO and O₂ mixture gases.

The future work that can be adopted for Chapter 6 would be first a reaction kinetic analysis for the catalytic processes on the Pt/ α -Al₂O₃(0001) surface at different temperatures. The estimation of the reaction order would be a preferential method to investigate the reaction mechanism. The difficulty for conducting this measurement at present is the dependent flow rate change between the reactant gases (see the Figure 6-6 in Chapter 6). I think it can be resolved by adding a gas line to introduce reference inert gas as a constant flow rate. The second would be the interpretation of the PTRF-XANES spectra. Theoretical simulation from the real-space models using FEFF code would be a choice to figure out the origin of the polarization dependence of the XANES spectra obtained at deactivated regime for CO oxidation. It could provide a good insight into the origin of catalyst deactivation and contribute to the development of active catalysts.

In my Ph.D. work, a surface sensitive *in situ / operando* XAFS technique has been successfully developed to determine the valence state and atomic-level 3D structure of active metal species dispersed on a well-defined surface during catalytic reactions under realistic gas pressure conditions. This technique can provide information on precise relationship between the 3D structure and catalytic activity of supported metal species in heterogeneous catalysis, which is difficult to obtain when using powdery samples or by UHV surface science techniques. My Ph.D. work will therefore make a significant contribution to atomic-level understanding of heterogeneous catalysis and further development of active supported metal catalysts.

ACKNOWLEDGEMENTS

First, I would like to express my deepest appreciation to my supervisor Prof. Kiyotaka Asakura. Without his guidance and leadership, I would have never had faith to finish my work as now. He always opens his office door to me whenever I have questions or ideas about my research. He is such a positive and optimistic person that gave me lots of courage to face difficulties.


I would like to extend my sincere thanks to my advisor Professor Satoru Takakusagi for his guidance throughout my graduation studies. Through his guidance I was able to develop a strong experimental background and fostered my ability to critically evaluate science. The thesis would not have been possible without his help. I am also grateful to the tough but fruitful time of the experiments in KEK.

Thanks should also go to Professor Daiki Kido for all his kind help and great patience. I had the pleasure of working with the group members in Asakura lab, all past and present members. Thanks for the time spent discussing all things science and otherwise.

Many thanks to all professors and staff in the Division of Quantum Science and Engineering, Institute for Catalysis and Photon Factory. Also to the DX fellowship for the financial support throughout my graduate program.

Most importantly, I am extremely grateful to my family for all their support and encouragement.

COPYRIGHTS & PERMISSIONS



Development of Operando Polarization-Dependent Total Reflection Fluorescence X-ray Absorption Fine Structure Technique for Three-Dimensional Structure Determination of Active Metal Species on a Model Catalyst Surface under Working Conditions

Author: Bang Lu, Daiki Kido, Yuta Sato, et al
Publication: The Journal of Physical Chemistry C
Publisher: American Chemical Society
Date: Jun 1, 2021

Copyright © 2021, American Chemical Society

PERMISSION/LICENSE IS GRANTED FOR YOUR ORDER AT NO CHARGE

This type of permission/license, instead of the standard Terms and Conditions, is sent to you because no fee is being charged for your order. Please note the following:

- Permission is granted for your request in both print and electronic formats, and translations.
- If figures and/or tables were requested, they may be adapted or used in part.
- Please print this page for your records and send a copy of it to your publisher/graduate school.
- Appropriate credit for the requested material should be given as follows: "Reprinted (adapted) with permission from {COMPLETE REFERENCE CITATION}. Copyright {YEAR} American Chemical Society." Insert appropriate information in place of the capitalized words.
- One-time permission is granted only for the use specified in your RightsLink request. No additional uses are granted (such as derivative works or other editions). For any uses, please submit a new request.

If credit is given to another source for the material you requested from RightsLink, permission must be obtained from that source.

BACK

CLOSE WINDOW

Figure A1. Copyright permission for: B. Lu, D. Kido, Y. Sato, H. Xu, WJ. Chun, K. Asakura and S. Takakusagi, "Development of Operando Polarization-Dependent Total Reflection Fluorescence X-ray Absorption Fine Structure Technique for Three-Dimensional Structure Determination of Active Metal Species on a Model Catalyst Surface under Working Conditions," J. Phys. Chem. C, vol. 125, no. 22, pp. 12424–12432, Jun. 2021, doi: 10.1021/acs.jpcc.1c02913.